IMPERIAL COLLEGE LONDON

ALTERNATIVE TECHNIQUES FOR DETECTION OF INACCESSIBLE PIPE CORROSION

by

Pouyan Khalili

A thesis submitted for the degree of

Doctor of Philosophy

Department of Mechanical Engineering

Imperial College London

March 2018

Abstract

Testing for corrosion in the petrochemical industry has always been a significant challenge which takes up a large portion of the operating expenditure. Whereas major advancements have been made for the detection of general corrosion, inspection at inaccessible locations, such as at pipe supports, remains a demanding prospect; this signifies the need for an alternative technique, capable of dealing with various surface conditions encountered when testing at such locations including weld patches, T-joints, surface roughness and coatings. Long range guided waves are commonly used to detect relatively severe defects in plain sections of pipe but are less suited to inspection at supports because the support itself gives significant reflection. The reflection coefficient at the support reduces with frequency so it would be beneficial to test at higher frequencies, which can also improve the sensitivity of the test to smaller, pitting-type defects.

Following the attractive properties of the Higher Order Mode Cluster (HOMC) proposed by Balasubramaniam et al. (IIT Madras), this research starts by investigating the nature of the mode cluster and shows that the features of this method are essentially those of the A1 mode in the high frequency-thickness regime. The study then goes on to investigate the possibility of exciting a single mode Lamb wave with low dispersion at a frequency-thickness of around 20 MHz-mm. Excitation of the A1 mode was considered because of its relationship with HOMC and due to its non-dispersive nature and low surface motion at such frequency-thickness products; this makes it attractive for inspection at supports since it will be unaffected by the support itself and also by surface roughness and attenuative coatings.

The thesis then explores the relative ability of different transducer types for single mode excitation in the medium and high frequency-thickness regimes; here the practical feasibility of exciting the A1 mode at around 20 MHz-mm, in spite of its low surface motion, is investigated. Next, a systematic performance analysis of the A1 mode compared to the existing inspection techniques is carried out and, finally the sensitivity of this technique to realistic 3-D pitting-type holes is established. The thesis shows that the A1 mode is an attractive tool for the detection of localized, sharp, severe defects that will be missed by standard, lower frequency guided wave testing.

تقدیم به پدر و مادرم

Acknowledgements

I would like to express my gratitude to my supervisor Prof. Peter Cawley for his guidance throughout this work and for his patience to oversee many of my shortcomings; thank you for giving me the opportunity to be a part of the distinguished NDE group.

I would also like to thank Prof. Peter Nagy for all the interesting and stimulating conversations we had.

I’m also grateful to all persons who helped me execute this work within the NDE group at Imperial College. Special thanks to: Dr. Anton Van Pamel, Dr. Julio Isla, Dr. Matthias Seher, and Gabor Gubicza.

Finally, I’m forever indebted to my family for their unconditional love and support throughout this work and in fact my entire life. This thesis is dedicated to you.

Declaration of Originality

The content of this thesis is the result of independent work carried out by myself under the supervision of Prof. Peter Cawley. Appropriate references have been provided wherever the work of others has been used.

Pouyan Khalili

Copyright Declaration

Contents

List of Figures

List of Tables

Chapter 1

Introduction

Problem Definition

1.1 Motivation

Conventional ultrasonic Non-Destructive Testing (NDT) techniques mostly involve the use of spot thickness gauging (Birks et al., 1991; Krautkramer and Krautkramer, 1990; Schmerr, 1998) for easy-to-access locations, though this is very time consuming if a large number of locations must be tested. Guided wave inspection provides an attractive alternative since it allows large areas to be covered from a single transducer location; this is highly beneficial especially for use on insulated or buried pipework and allows the inspection of physically inaccessible regions of a structure. Contrary to bulk waves, guided waves can only exist in elongated structures called waveguides, such as pipes and plates, where they continuously interact with the boundaries of the structure; this enables long propagation distances to be achieved with minimal energy loss. However, due to their nature, guided waves exhibit multiple wave modes which can exist at the same time; also these modes are, in general, dispersive meaning their velocity is a function of frequency. Therefore, understanding the properties of guided waves, such as group and phase velocity dispersion curves and displacement mode-shape of a wave mode, are fundamental in the selection of the appropriate method for a given application (Wilcox et al., 2002).

Analytical methods are often used for waveguides with simple cross-section profiles, in order to solve dispersion equations, where the unique properties of each wave mode can be represented by its dispersion curve. One of the key software packages which offers these analytical solutions is DISPERSE (Pavlakovic et al., 1997). This software, which was developed by the members of the NDE group at Imperial College, enables quick evaluation of the guided wave properties based on the user defined waveguide; here, regular structures such as plates and cylinders can be defined as multi-layered or homogeneous, composed of isotropic or anisotropic material(s), in a vacuum, immersed in a fluid or embedded in a solid. By studying the physical properties of the guided waves, specific inspection methods can be commercially developed (Alleyne et al., 1998, 2001; Mudge, 2001; Sheard and McNulty, 2001) which, for a given application, allow more efficient testing to be carried out.

However, when considering propagation across irregular geometries, such as T-joints or discontinuities within a structure, the behaviour of guided waves is difficult to determine via analytical means; for such cases, the Finite Element (FE) method has been frequently applied. This works by subdividing the model into discrete number of elements where each element can be solved through simple equations; these are then assembled to yield a global system of equations for the entire model which can be realised based on the user defined boundary conditions (Drozdz, 2008; Zemanek, 1972). Therefore, FE allows the investigation of guided wave propagation in complex geometries which would otherwise be costly to investigate experimentally. It has been an essential tool in understanding the transduction of guided waves and the effect of discontinuities, such as corrosion defects, on wave propagation (Alleyne, 1991; Lowe and Diligent, 2002; Moser et al., 1999).

Inspection for corrosion is essential for the petrochemical and other industries and it forms a significant fraction of the operating expenditure; based on a 2006 study carried out by Saudi Aramco, the average value of the cost of corrosion is 4.2% of the gross national product (GNP) of a country, based on 12 national surveys while a more recent study estimated the USA cost at 6% of the GNP(Tems and Al Zahrani, 2006). The more common types of corrosion damage include wide area gradual thickness loss and localised, shape, pitting type defects. Guided waves are used extensively to check for such defects and while low frequency guided wave inspection (< 1 MHz-mm or 100kHz in a 10 mm thick plate/pipe) is able to detect and locate damaged areas reliably, it is most suited for inspection of wide-area gradual wall thinning where typically a cross-sectional loss of around 5% within a plain section of pipe is detectable (Demma et al., 2004, 2003; Lowe et al., 2002; Mudge and Catton, 2008; Rose et al., 2004). However, testing for corrosion defects can be problematic especially at inaccessible locations, e.g. at pipe supports, as at the low frequencies required to detect wide-area thickness loss, the support itself gives a significant reflection resulting in a reduction in detectability (Galvagni and Cawley, 2011); also the locations of concern are inaccessible for conventional ultrasonic thickness gauging. Similar issues arise when testing the floor of storage tanks from the small region of the floor protruding outside the tank wall. Also, deep defects with relatively small plan area are often a concern due to the compromised sensitivity to small defects as a result of the low frequencies used. This suggests that it would be beneficial to test at higher frequencies where the sensitivity to localised, sharp, pitting-type defects would be improved. However, inspection can still be complex as the presence of multiple and often dispersive guided wave modes at higher frequencies can limit defect detectability.

There has been growing interest in testing over 1-5 m distances at much higher frequencies (> 5 MHz-mm); Balasubramaniam et al. have introduced a technique they call Higher Order Mode Cluster (HOMC) where the excited higher order Lamb modes combine to form a non-dispersive cluster (Balasubramaniam et al., 2012; Chandrasekaran et al., 2009, 2010; Jayaraman et al., 2009; Ratnam et al., 2012; Satyarnarayan et al., 2008; Swaminathan et al., 2011). HOMC uses a conventional piezoelectric transducer mounted on wedges, where the angle is selected based on the application, operating at a frequency-thickness of around 20 MHz-mm, and because of the raised frequency content, the method is reported to be highly sensitive to small diameter, deep pits. In addition, the excited Lamb modes exhibit very low surface motion which makes HOMC insensitive to surface features/conditions such as pipe supports or T-joints, as well as attenuative coatings and surface roughness. Given these properties, this method has been employed for various applications; it is reported (Swaminathan et al., 2011) that HOMC is able to detect localised flaws along the axial direction of the pipe while its sensitivity is barely affected by the addition of a weld patch on top of the defects. Also this method has been able to detect rectangular notches with 0.5 mm width and at least 20% depth as well as machined pinholes with 1.5 mm diameter (Satyarnarayan et al., 2008). However, it is not clear how Lamb waves with negligible out-of-plane surface displacements are excited, nor it is evident which modes are excited and how they contribute to the formation of the reported cluster.

Thus, the first motivation for this work involves understanding the formation process of HOMC within a waveguide; this includes establishing the presence of the contributing Lamb wave modes for various excitation configurations and their effect on the characteristics of HOMC. To achieve this, it is necessary to predict the excitation response which requires understanding of the mode selectivity and excitability of Lamb modes, for a given excitation configuration.

The second motivation is to evaluate the performance of HOMC relative to other possible techniques when used to test for corrosion at inaccessible regions; this involves investigating the effect of various surface features/conditions, such as liquid loading, surface coatings, rough surfaces and T-joints, on the wave propagation. In order to further establish the sensitivity of the method, it is necessary to investigate the wave interaction with different types of defect associated with corrosion damage including localised, sharp defects as well as wide-area, gradual, wall thinning.

Overall, the main aim of the thesis is to investigate different possible means of corrosion detection using guided waves, considering both sharp and gradual corrosion patches and to establish the performance of each method when testing at inaccessible locations by evaluating the influence of various surface features/conditions which are common over such regions.

1.2 Outline of Thesis

Chapter 2 reviews the basic physics of guided waves, including the prediction of dispersion curves and mode shapes for different wave modes, plus the use of FE analysis to predict the field generated by different transducer geometries as well as the reflection from defects of different shapes.

Chapter 3 looks at the excitation of HOMC and it is shown that the cluster discussed in the literature is essentially a pure A1 Lamb mode. The possibility of single A1 mode generation at high frequency-thickness products and the effect of different excitation parameters, including the excitation signal in time, transducer size and wedge angle, on the transduction of Lamb waves is investigated analytically; these predictions are then verified through FE analysis and experimental measurements.

In Chapter 4, the relative ability of wedge-mounted piezoelectric and Electro-Magnetic Acoustic Transducer (EMAT) probes for pure mode excitation at medium and high frequency-thickness products is established and recommendations on the appropriate transducer type for a given application are presented.

Chapter 5 compares the performance of HOMC/A1 mode with other corrosion inspection methods. The effect of surface features/conditions such as liquid loading, coatings, rough surface and T-joints on each method is also investigated in this chapter, along with the sensitivity of each method to sharp and gradual defects.

Chapter 6 looks at the sensitivity of HOMC/A1 mode to 3-D part-depth holes in a realistic test setup. Here, two extremes are considered: a circular defect in which there is no planar surface normal to the incident wave, and a square defect oriented with one face normal to the beam.

Chapter 7 summarises the key findings and contribution of the thesis and discusses the potential for future work.

Chapter 2

Guided Waves

Background

2.1 Background

This chapter introduces the basic concepts of ultrasonic guided wave propagation within a waveguide such as a plate or a pipe. This includes establishing the fundamental physics of guided waves along with the use of dispersion curves and mode shapes; the characteristics and application of different guided wave frequency regimes is also discussed. Finally, the employment of FE in understanding the application of various corrosion inspection techniques within complex geometries, via 2-dimensional and 3-dimensional models, is outlined.

In unbounded, elastic media, there are two types of wave possible: longitudinal (also known as compression) and shear (also known as transverse) waves which are both classified as bulk waves, meaning their propagation characteristics are determined solely by the material properties of the medium. Bulk waves have been used extensively in the NDT industry and is a well-documented subject (Auld, 1991; Brekhovskikh, 1976; Graff, 1975; Rose, 2014); although they can provide accurate and reliable inspection, guided waves are preferred when testing large structures where most often the access is limited, e.g. in the case of insulated pipes or pipe supports. Contrary to bulk waves, guided waves can only exist in bounded structures. The difference between the two arises through the application of boundary conditions which are dictated by the geometry of the waveguide. Essentially, guided waves are generated by the constant interaction of longitudinal and shear waves with the boundaries of the waveguide which leads to reflection, refraction and mode conversion between the two, so consequently, their behaviour can be predicted via the application of appropriate boundary conditions.

However, the implementation of guided waves can be highly complex as they are characterised, unlike bulk waves, by an infinite number of modes that are often dispersive, meaning their propagation velocity depends on frequency. As a result, each guided wave mode can only exist along a line in the frequency-wavenumber space; this relationship is often presented by the use of dispersion curves.

2.1.1 Equations of motion in unbounded, isotropic media

As mentioned above, both bulk and guided waves are governed by the same equations of motion; the wave equations in unbounded, isotropic media is well documented (Auld, 1991) and so the fundamental governing equations are outlined in this section.

By combining the Hooke's law for an isotropic, homogeneous, linearly elastic media and the Euler's equation of motion derived from Newton's second law, the Navier's differential equation of motion can be obtained:

$$\mu\nabla^2\mathbf{u} + (\lambda + \mu)\nabla(\nabla.\mathbf{u}) = \rho\frac{\partial^2\mathbf{u}}{\partial t^2} \tag{2.1}$$

where $\mathbf{u}$ is the displacement field, μ and λ are the Lamé constants, ρ is the material density and ∇ is the vector differential operator and ∇^2 is the scalar differential operator. Equation 2.1 can be expanded in its three spatial components x, y, and z:

$$\mu\left(\frac{\partial^2}{\partial x^2} + \frac{\partial^2}{\partial y^2} + \frac{\partial^2}{\partial z^2}\right)u_x + (\lambda + \mu)\frac{\partial}{\partial x}\left(\frac{\partial u_x}{\partial x} + \frac{\partial u_y}{\partial y} + \frac{\partial u_z}{\partial z}\right) = \rho\frac{\partial^2 u_x}{\partial t^2} \tag{2.2}$$

$$\mu\left(\frac{\partial^2}{\partial x^2} + \frac{\partial^2}{\partial y^2} + \frac{\partial^2}{\partial z^2}\right)u_y + (\lambda + \mu)\frac{\partial}{\partial y}\left(\frac{\partial u_x}{\partial x} + \frac{\partial u_y}{\partial y} + \frac{\partial u_z}{\partial z}\right) = \rho\frac{\partial^2 u_y}{\partial t^2}$$

$$\mu\left(\frac{\partial^2}{\partial x^2} + \frac{\partial^2}{\partial y^2} + \frac{\partial^2}{\partial z^2}\right)u_z + (\lambda + \mu)\frac{\partial}{\partial z}\left(\frac{\partial u_x}{\partial x} + \frac{\partial u_y}{\partial y} + \frac{\partial u_z}{\partial z}\right) = \rho\frac{\partial^2 u_z}{\partial t^2}$$

These equations must be satisfied by all elastic waves propagating in the material and are referred to as the wave equations. By the use of Helmholtz decomposition on the wave equation 2.1, the displacement field $\mathbf{u}$ can be expressed as a sum of the rotational (shear) component $\nabla \times \mathbf{H}$ and a non-rotational (longitudinal) component $\nabla \phi$:

$$\mathbf{u} = \nabla \times \mathbf{H} + \nabla \phi \tag{2.3}$$

where ϕ is a scalar potential and $\mathbf{H}$ is a zero divergence $(\nabla . \mathbf{H} = 0)$ vector potential. Then, substituting equation 2.3 into Navier's differential equation 2.1, the equation of motion can be de-coupled into two independent terms, each representing a potential:

$$\frac{\partial^2 \phi}{\partial t^2} = c_l^2 \nabla^2 \phi \tag{2.4}$$

$$\frac{\partial^2 \mathbf{H}}{\partial t^2} = c_s^2 \nabla^2 \mathbf{H} \tag{2.5}$$

where c_l and c_s are the longitudinal and shear wave velocities in an unbounded isotropic material, respectively and can be expressed as:

$$c_l^2 = \frac{\lambda + 2\mu}{\rho} \tag{2.6}$$

$$c_s^2 = \frac{\mu}{\rho} \tag{2.7}$$

The equations 2.4 and 2.5 are known as the Helmholtz differential equations and their general solution can be obtained as:

$$\phi = \phi_0 e^{i(k_l x - \omega t)} \tag{2.8}$$

$$\mathbf{H} = \mathbf{H}_0 e^{i(k_s x - \omega t)} \tag{2.9}$$

where ϕ_0 and $\mathbf{H}_0$ are arbitrary initial constants, x is the spatial coordinate indicating the wave propagation direction, $\omega = 2\pi f$ is the angular frequency, t is the time variable and $k_{l,s}$ are the longitudinal and shear wavenumber vectors which can be expressed as following:

$$\left|k_{l,s}\right| = \frac{\omega^2}{c_{l,s}^2} \tag{2.10}$$

2.2 Guided Waves in Constant Thickness Structures

An ultrasonic guided wave is an acoustic wave travelling within the boundaries of a structure. When ultrasonic excitation occurs in a waveguide, the energy traveling from the excitation region interacts with the upper and lower boundaries of the structure resulting in mode conversion between the longitudinal and shear waves. With the propagation of these partial waves, the mode conversion process repeats itself continuously, where superposition enables the formation of wave packets otherwise known as guided wave modes.

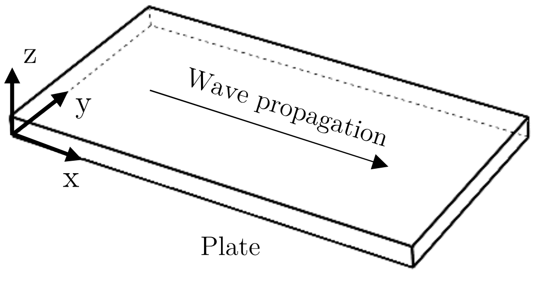

Figure 2.1: *Schematic diagram of a plate in a Cartesian coordinate system.*

Figure 2.1 shows the schematic diagram of a plate in a Cartesian coordinate system. The plate is assumed to be infinite in x and y directions while, as shown, the origin of the z axis (z=0) is located on the bottom surface; the propagation is in the x direction and the fields in the y direction are assumed to be uniform. Also the boundary conditions determined by the geometry of the plate can be imposed by the application of traction and/or displacements at the boundaries; in the case of a free isotropic plate, the parallel surfaces at z=0 and z=t (here, t indicates the thickness of the plate) must be considered to be traction free.

In order to obtain the exact solution to the wave equations 2.4 and 2.5, there have been a number of approaches proposed. The most popular methods of solution are the displacement potentials [as discussed above, see (Achenbach, 1973) for details] and the partial wave technique [see (Auld, 1991) for details]. Using the displacement potential approach, the wave equations can be simplified, in the case of Lamb waves, by assuming that the particle displacement is zero in the y direction (plain strain case) and the only rotational component is about the y axis ($H_x = H_z = 0$), so:

$$\frac{\partial^2 \phi}{\partial t^2} = c_l^2 \left(\frac{\partial^2 \phi}{\partial x^2} + \frac{\partial^2 \phi}{\partial z^2}\right) \tag{2.11}$$

$$\frac{\partial^2 \mathbf{H}_y}{\partial t^2} = c_s^2 \left(\frac{\partial^2 \mathbf{H}_y}{\partial x^2} + \frac{\partial^2 \mathbf{H}_y}{\partial z^2}\right) \tag{2.12}$$

In the case of a free plate, the solution to 2.11 and 2.12 can be represented as the dispersion equations of symmetric and anti-symmetric modes, while in the case of Shear Horizontal (SH) waves, the wave equations can be further simplified by assuming that the only component of displacement is in the y direction, and uniform along the y axis, the scalar potential 2.4 can be eliminated (Auld, 1991) and therefore:

$$\frac{\partial^2 \mathbf{H}}{\partial t^2} = c_s^2 \left(\frac{\partial^2 \mathbf{H}}{\partial z^2}\right) \tag{2.13}$$

The solution to 2.13 can be represented as the dispersion equations of the SH modes.

The dispersion equations can be visualised using the dispersion curves, where the phase velocity of each of the guided wave modes is plotted against the frequency-thickness product; this enables the curves to be used for a plate with any thickness. The general purpose software package DISPERSE (Pavlakovic et al., 1997), developed by the NDE group at Imperial College, is used extensively in this thesis, in order to obtain the dispersion curves associated with the guided wave modes along with their corresponding mode shape which are employed to determine the appropriate method for a given application.

2.2.2 Dispersion curves

The propagation of a wave mode can be characterised by its phase and group velocities. Phase velocity, c_p, is defined as the rate at which the phase of a mode propagates in space while group velocity, c_{gr}, is the speed at which a guided wave packet travels within the waveguide. Phase velocity can be defined in terms of angular frequency ω and wavenumber k:

$$c_p = \frac{\omega}{k} \tag{2.14}$$

More conveniently, equation 2.14 can also be stated in terms of wavelength λ and frequency f:

$$c_p = \lambda f \tag{2.15}$$

The group velocity of a guided wave mode is related to its phase velocity through the following equation (Graff, 1975; Rose, 2014):

$$c_{gr} = \frac{d\omega}{dk} = c_p + k\frac{dc_p}{dk} \tag{2.16}$$

Dispersion occurs because of the frequency-dependent velocity variation of a wave; the manifestation of this phenomenon is when a guided wave mode is excited by a signal finite in duration, the signal is distorted in time and space as it propagates in the structure. Guided waves are generally dispersive and the severity of this property depends on the nature of the mode, centre frequency and the absolute frequency bandwidth. In order to best understand the dispersion characteristic of each guided wave mode, dispersion curves are employed.

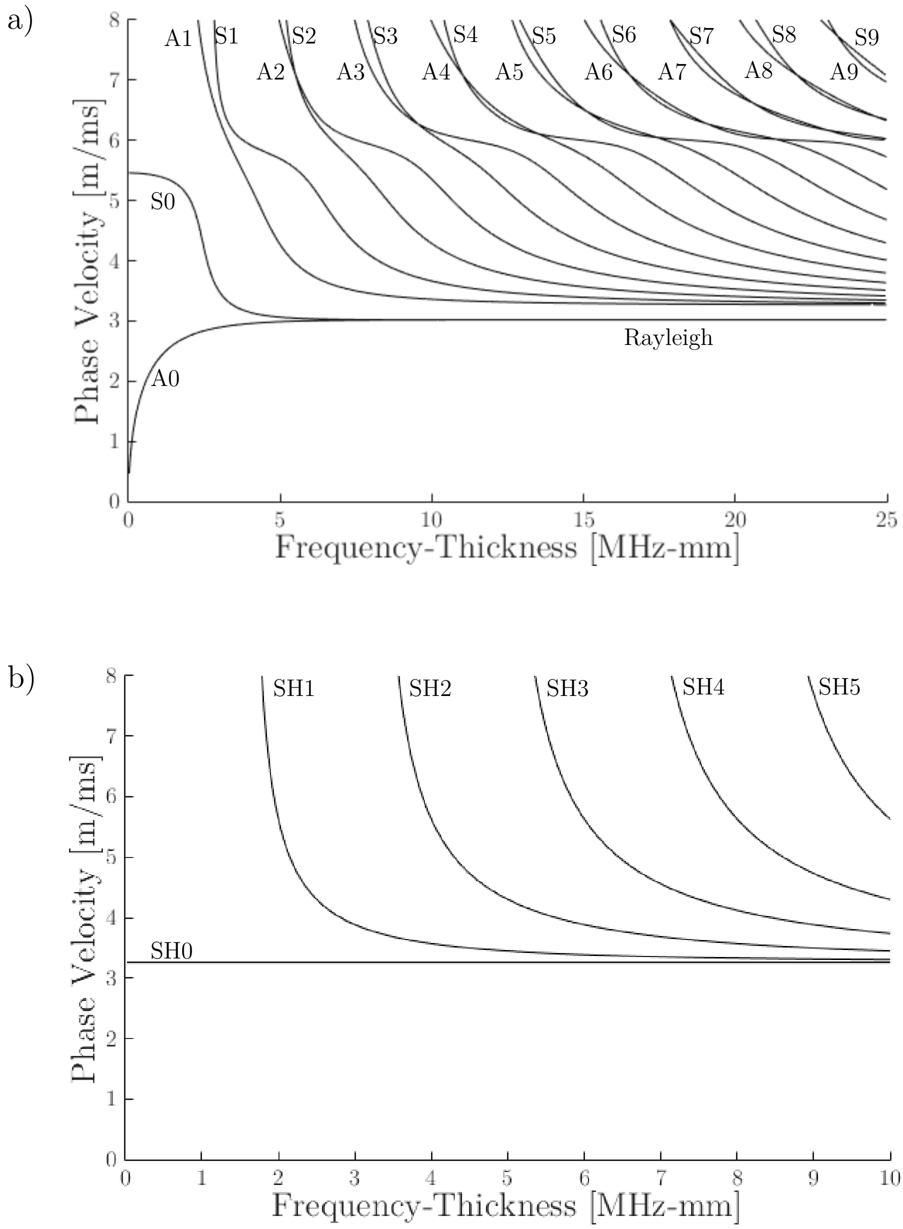

Figure 2.2: *Phase velocity dispersion curves of guided waves in a steel plate a) Lamb modes; b) shear horizontal (SH) modes; generated using DISPERSE (Pavlakovic et al., 1997).*

Figure 2.2 shows the typical phase velocity dispersion curves of the Lamb (a) and SH (b) modes in a steel plate; due to the nature of the dispersion relations (Rose, 2014), the frequency axis can be scaled with the plate thickness for generality. Lamb wave modes (shown in Figure 2.2a) are conventionally labelled as S (symmetric) modes and A (anti-symmetric) modes, followed by a counter number which indicates the harmonic order of the mode; SH wave modes (shown in Figure 2.2b) can also be either symmetric or anti-symmetric but in this thesis, these two families are differentiated via their counter number; here even numbers (including 0) indicate the symmetric modes (SH0, SH2, SH4, …) and odd numbers represent the anti-symmetric modes (SH1, SH3, SH5, …). It is evident from the figure that all the guided wave modes, except for the fundamental SH0 mode, are dispersive and multiple modes can coexist at higher frequencies.

In order to demonstrate the effect of dispersion on the propagation of the guided wave modes, simulated signals (using DISPERSE) are shown in Figure 2.3; here, a 5-cycle Hanning windowed excitation signal at 1.5 MHz-mm (a) has been considered and the responses of the SH0 (b) and S0 (c) modes have been obtained after a 500 mm propagation distance. It is clear that, unlike the SH0 mode which maintains the shape of the excitation signal since being non-dispersive, the S0 mode at this frequency-thickness product suffers from high dispersion which results in the distortion of the wave packet in space (as shown in Figure 2.3c). However, dispersive modes, such as S0 at 1.5 MHz-mm, can still be implemented for inspection if a shorter propagation distance is considered; Figure 2.3d shows the response of the S0 mode over a 100 mm propagation distance where the signal distortion is largely reduced compared to Figure 2.3c. While, in practice, it is more convenient to use modes with no or minimal levels of dispersion, compensation methods (Roux et al., 1997; Wilcox et al., 2001b) can be implemented if the use of a dispersive mode is beneficial.

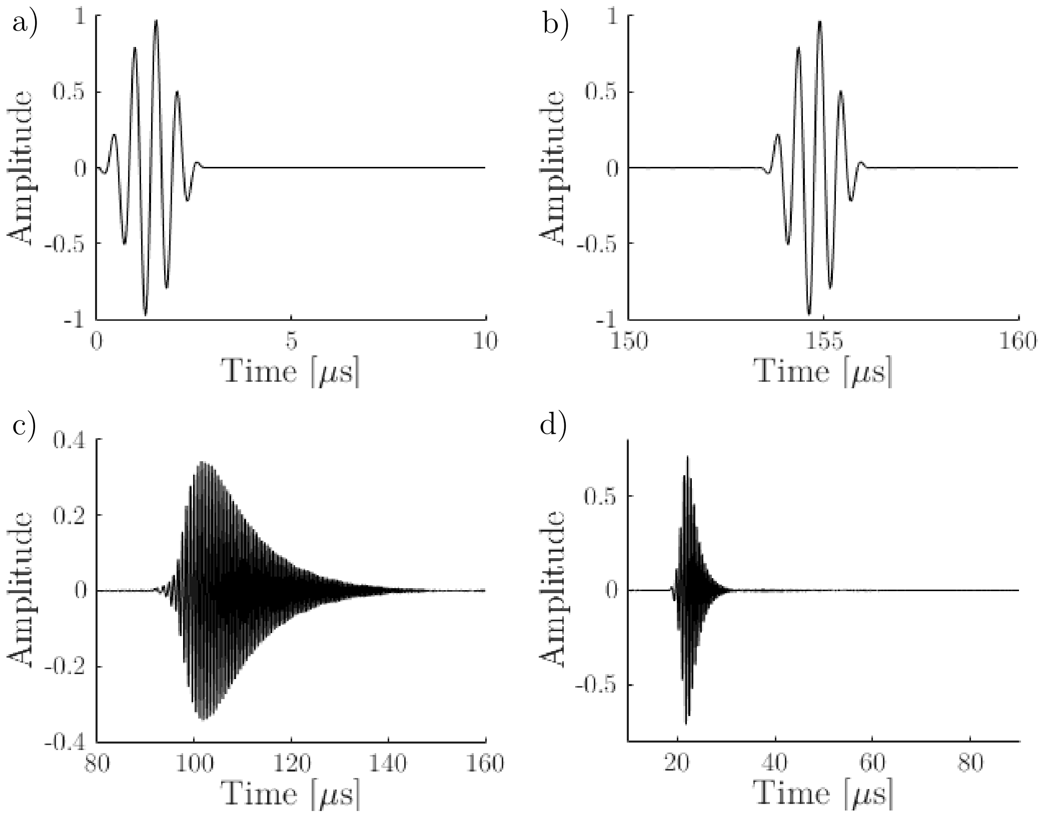

Figure 2.3: *a) 5-cycle Hanning windowed toneburst excitation signal at 1.5 MHz-mm (150 kHz centre frequency on a 10 mm thick steel plate); b) predicted SH0 mode signal after 500 mm propagation distance; c) predicted S0 mode signal after 500 mm propagation distance; d) predicted S0 mode signal after 100 mm propagation distance; generated using DISPERSE (Pavlakovic et al., 1997).*

2.2.3 Mode shapes

The mode shape of a guided wave mode represents the distribution of field parameters (stress, energy, displacement etc.) of the corresponding mode along the cross-section of the waveguide, so it can be a very useful tool in predicting the behaviour of a mode in a given situation. Displacement mode shapes, in particular, are used to characterise the different mode families such as symmetric, anti-symmetric Lamb waves as well as shear horizontal modes. Figure 2.4 shows the displacement mode shapes of the S0 (b), A0 (c) and SH0 (d) modes at 0.5 MHz-mm; the coordinate system (a) is also displayed. It is clear that the S0 mode is dominated by the in-plane displacement in the direction of propagation (U_x) with small presence of out-of-plane motion (U_z), while the A0 mode exhibits a large out-of-plane displacement with smaller presence of in-plane motion. The SH0 mode on the other hand, only contains the in-plane displacement perpendicular to the propagation direction (U_y).

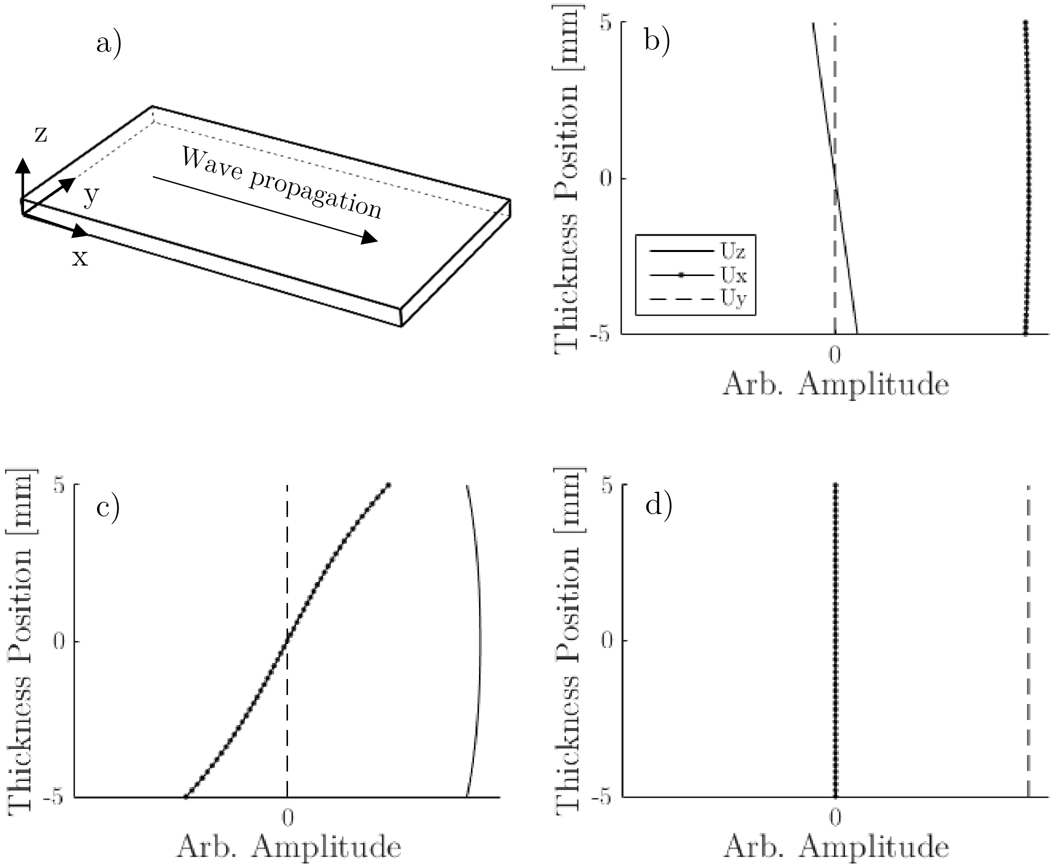

Figure 2.4: *a) Coordinate system; Displacement mode shapes at 0.5 MHz-mm of the b) S0 mode; c) A0 mode; d) SH0 mode; obtained from DISPERSE (Pavlakovic et al., 1997).*

2.2.4 Low frequency regime

Long distance propagation of Lamb waves is achieved at frequencies below the A1 mode cut-off (up to ~1 MHz-mm, so in a 10 mm thick plate the frequency is below 100 kHz), which minimises the number of the existing modes but due to the low frequency content, and therefore the long wavelength of the guided wave modes, this method is best suited for detecting severe (wide-area) defects (Carandente et al., 2010; Mudge and Catton, 2008; Rose et al., 2004). Examples include the use of long range guided waves to detect circumferential defects (Alleyne et al., 1998) with various depths and profiles (Carandente and Cawley, 2012); also there has been interest in using this method for inspection of rail and thin-walled tubes (Mohr and Holler, 1976). In addition, due to the limited number of guided wave mode that can exist at low frequencies, this method has been shown to offer good application potential, such as in guided wave tomography (Belanger and Cawley, 2009; Huthwaite, 2014a; Huthwaite and Simonetti, 2013).

There are a number of techniques to implement the low frequency guided wave method; the transduction is commonly achieved through an array of point sources which can be done via direct contact piezoelectric transducers (PZT) (Belanger and Cawley, 2009; Clarke et al., 2009; Ning Hu et al., 2008), ring excitation with EMATs (Herdovics and Cegla, 2016; Seher et al., 2014, 2015) or magnetostrictive probes (Kim et al., 2005; Vinogradov, 2009).

2.2.5 Medium frequency regime

The medium frequency regime is considered from 1 MHz-mm to around the 5 MHz-mm frequency-thickness region of the dispersion curves. The main advantage of using this method, over the long range guided waves, is the improved sensitivity to small defects which arises from the raised frequency content. However, the presence of multiple and often dispersive modes, limits defect detectability with this method (Alleyne and Cawley, 1992a; Ditri et al., 1992; Quarry and Rose, 1999; Wilcox et al., 2001a). There has been growing interest in remnant thickness mapping (Howard and Cegla, 2016, 2017) that takes advantage of the typical dispersive nature of the modes, as their propagation velocity is highly sensitive to thickness changes which are introduced by defects such as corrosion damage.

There are various excitation techniques used for implementation in this frequency-thickness region; here the transduction is usually achieved via piezoelectric transducers mounted on an angled wedge (Ditri et al., 1993; Li and Rose, 2001; Rose, 2014; Wilcox et al., 2002) or EMATs (Dixon and Palmer, 2004; Guo et al., 1997; Salzburger et al., 2012; Salzburger, 2009; Thompson et al., 1972).

2.2.6 High frequency regime

As mentioned above, there has been a growing interest in guided wave testing from 1 m to 5 m range at much higher frequencies (>5 MHz-mm) as the reflection coefficient due to the presence of surface features, such as T-joints/welded patches, reduces with frequency (Galvagni and Cawley, 2011), and also the sensitivity of the test to smaller pitting-type defects is improved. Balasubramaniam et al. have introduced a technique called Higher Order Mode Cluster (HOMC) where the higher order Lamb modes, excited around 20 MHz-mm, combine to form a non-dispersive cluster (Balasubramaniam et al., 2012; Chandrasekaran et al., 2009, 2010; Jayaraman et al., 2009; Ratnam et al., 2012; Satyarnarayan et al., 2008; Swaminathan et al., 2011). Such Lamb waves have reduced surface sensitivity since at higher frequencies, the surface motion of the relevant modes reduces (Jayaraman et al., 2009) while the sensitivity to deep defects with small footprints is improved. However, as shown in Figure 2.2a, multiple modes can coexist at around 20 MHz-mm which adds to the complexity of the inspection.

Understanding the generation of higher order Lamb waves can be challenging because, as shown in Figure 2.2a, there are a large number of modes that exhibit similar dispersion characteristics. Transduction of such modes is mostly achieved via piezoelectric transducers mounted on an angled wedge (Hirao et al., 1982; Khalili and Cawley, 2016; Masserey and Fromme, 2013; Satyarnarayan et al., 2008) with rarer applications of EMATs (Ratnam et al., 2012).

2.3 Finite Element (FE) Method

The solution to the dispersion equations which can be obtained analytically provides very useful information on the nature of the guided wave modes; however, in order to develop and understand the behaviour of an inspection technique, there is some information, such as the propagation of ultrasonic waves within complex waveguides that would be very difficult to obtain through analytical means.

Finite Element (FE) analysis is a highly beneficial tool because it allows a variety of complex geometries and boundary conditions to be considered which otherwise would be costly to investigate experimentally. In FE, the desired structure/waveguide is divided into a finite number of elements which are connected to each other via “nodes” at their boundaries; nodes are coordinate locations in space where the degrees of freedom (DOF) associated with a body are defined (Drozdz, 2008). These DOFs also determine the moments and forces that are transferred from one element to the adjacent element (Drozdz, 2008). The field variable (e.g. displacements) associated with each element can be determined through simple equations; these equations are then combined in order to obtain a global equation based on the user-defined boundary conditions (Drozdz, 2008).

FE was used extensively in this thesis in order to model ultrasonic wave propagation in various geometries and waveguides with different surface conditions/features. The simulations carried out used a combination of two general purpose software packages: the commercial package ABAQUS CAE (Abaqus 6.14, 2014) and Pogo (Huthwaite, 2014b), which is an FE solver, developed by the NDE group at Imperial College, which runs on graphics cards to greatly reduce the required simulation time.

FE works by discretising the equations 2.4 and 2.5, where the simplified governing equations for a free body, in the most general case, can be expressed as:

$$\overline{\mathrm{M}}\ddot{u} + \overline{\mathrm{K}}u = 0 \tag{2.17}$$

where $\overline{\mathrm{M}}$ and $\overline{\mathrm{K}}$ refer to mass and stiffness matrices respectively. Using a time marching procedure, the equation 2.17 can be solved in sequenced time steps which enables the simulation of wave propagation within a structure.

FE allows the equation 2.17 to be solved via implicit and explicit schemes; throughout this thesis, an explicit scheme has been used as it is less computationally expensive, but since the scheme relies on the integration of acceleration to obtain the displacement field, for it to generate accurate results, the time increments (Δt) must be sufficiently small. Also, in order to accurately simulate a propagating wave, the spatial discretisation (element size Δx) should allow at least 10 elements along the shortest wavelength possible within the frequency bandwidth of the wave (Drozdz, 2008):

$$\Delta x \leq \frac{\lambda_{min}}{10} \tag{2.18}$$

Also to ensure a convergent solution for the FE model, the time step must be set as (Drozdz, 2008):

$$\Delta t \leq 0.8 \frac{\Delta x}{V_{max}} \tag{2.19}$$

where V_{max} is the velocity of the fastest wave (conservatively, the longitudinal wave velocity, c_l, is usually considered).

Full 3-dimentional (3-D) FE models can be used to simulate the wave propagation in a complex geometry; however, these can be very time consuming and computationally expensive, especially if a large number of elements is required to produce accurate results. In order to simplify the simulations, 2-D models are often employed in cases where the effect of width (y direction in Figure 2.1) on the wave propagation can be neglected, such as for the simulation of planar waves where the beam spread is minimal.

2.3.1 2-dimensional model

2-D FE analysis has been used to obtain the majority of the results presented in this thesis because it captures most of the important physics and, as mentioned, it is much more efficient computationally. The key disadvantages of 2-D models are the neglecting of the beam spread and also that the effects of diffraction around small defects are not captured, where, in both cases, lower frequency methods are affected more than the higher ones because of their larger wavelengths.

In general, based on the nature of the study, the excitation of the ultrasonic waves was performed via either phased surface excitation or mode shape transduction. Figure 2.5a illustrates the phased surface excitation which was used to simulate a piezoelectric transducer (T) mounted on a wedge configuration without the need to model the probe assembly; here the appropriate force was applied to nodes on the red line and the wedge was not modelled. Figure 2.5b shows the mode shape excitation of an arbitrary mode which involves the application of force along the plate thickness weighted according to the desired mode shape; this allows pure mode excitation with minimal intrusion of the other modes.

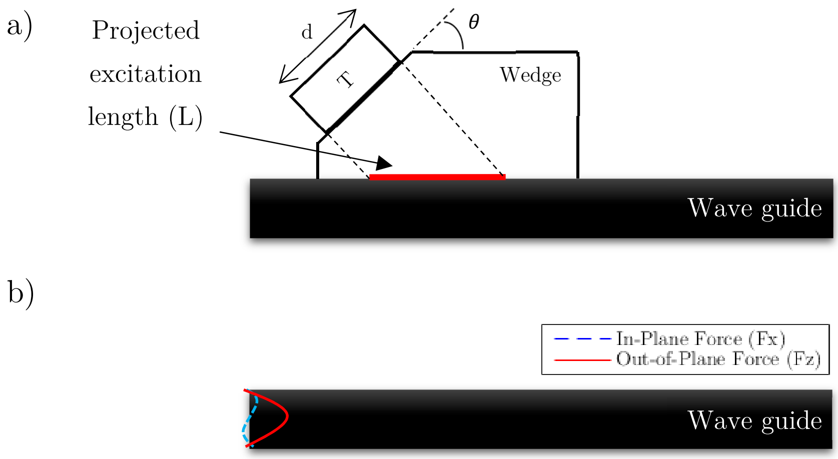

Figure 2.5: *(a) Transducer schematic of the piezoelectric transducer mounted on an angled wedge (Khalili and Cawley, 2016); (b) Schematic of the mode shape excitation of an arbitrary mode with in-plane and out-of-plane forces.*

According to the application and the inspection method, the reception of the ultrasonic waves was also tailored; in order to simulate the phasing effect associated with wedge reception, phased addition of the surface time-traces was employed, while in cases where accurate amplitude readings of a particular mode in a complex, multi-mode signal were required, modal decomposition was carried out by the use of a 2-D Fourier transform (FFT) (Alleyne and Cawley, 1991). In some cases, cross-sectional time-traces were monitored in order to further confirm the presence of a particular guided wave mode.

All 2-D simulations were performed in a plane strain configuration where the waveguide models were created using square elements [CPS4R (Abaqus 6.14, 2014)]. A typical model used to simulate a high frequency ultrasonic wave method incorporated around 4 million elements (model of a 10 mm thick, 1 m long steel plate with 50 μm side length square elements). The majority of the simulations were performed using Pogo, where due to the properties of this software

(Huthwaite, 2014b), individual simulations took only around 5 minutes to complete (compared to around 8 hours on a CPU based FE package) on a data cruncher with 4× NVIDIA GeForce GTX Titan Black graphic cards, 2× quad-core Intel Xeon E5-2609 v2 processors and 32GB DDR3 memory.

2.3.2 3-dimensional model

For cases where the effect of beam spread and diffraction around small defects needed to be studied, full 3-D FE simulations were employed; this allowed the investigation of ultrasonic wave propagation in a more realistic setup. However, as mentioned above, using 3-D models can be very computationally expensive, especially in the case of the high frequency inspection methods because such techniques exhibit small wavelengths which require very small element sizes (equation 2.18) to ensure accurate results. As shown in Figure 2.6, in order to make the simulations practical, only the necessary portion of the desired structure can be modelled where the results would be extrapolated for longer propagation distances; here an example to record the reflection from a flat bottomed hole is illustrated where symmetry was employed to halve the model size.

Due to the size limitations of such models, the generation of the guided wave modes was done by exciting the mode shape through the thickness of the plate. For accurate reception of the desired mode, mode shape reception was carried out; this process involved summing the displacements along the cross-section weighted according to the corresponding mode shape. In order to eliminate the interference of edge reflections which arise due to the small size of the model, Absorbing Layers using Increasing Damping (ALID) (Drozdz, 2008; Rajagopal et al., 2012) boundary was placed around the waveguide (as shown in Figure 2.6).

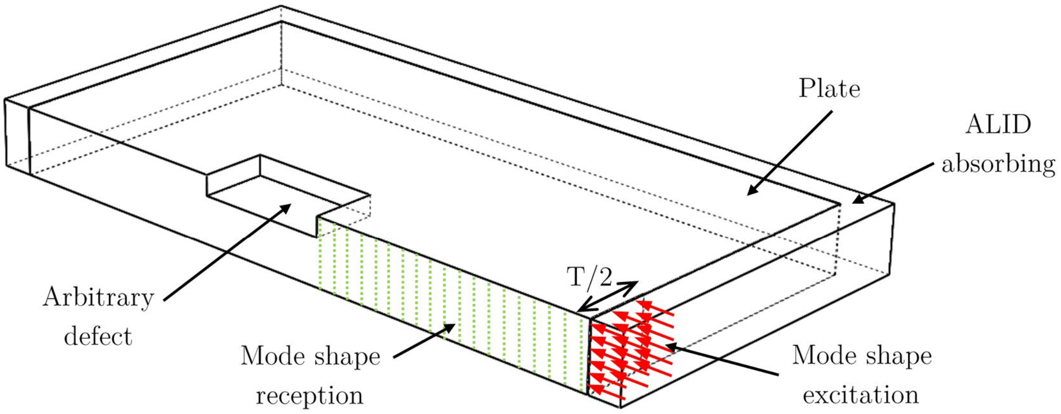

Figure 2.6: *Schematic of a general 3-D FE setup with the plane of symmetry through an arbitrary defect. The red arrows represent the mode shape excitation along the equivalent width of the transducer (T); the green dotted lines show the mode shape reception of the reflected wave* (Khalili and Cawley, 2018a).

All the 3-D FE models were created using cubic elements [C3D8R (Abaqus 6.14, 2014)] where a typical model involved around 28 million elements (model of a 10 mm thick, 100 mm × 25 mm steel plate with 100 μm side length cubic elements + ALID elements). FE was carried out on ABAQUS CAE commercial package (Abaqus 6.14, 2014) where each individual simulation took around 8 hours to complete on a data cruncher with an 8-core Intel Xeon E5-2690 processor and 256GB DDR4 memory. It is noteworthy that while the Pogo software preferable when dealing with complex models because of the much shorter simulation times, due to the lack of system availability at the time when the numerical simulations for this study were carried out, ABAQUS was employed for the large, element-dense 3-D models. It is noteworthy that based on recent developments, Pogo has been able to accommodate much larger models compared to ABAQUS.

2.4 Summary

In this chapter, the fundamental concepts of sound propagation in unbounded media have been presented where the possibility of two bulk wave modes was discussed: longitudinal and shear waves. The formation and basic physics associated with guided waves in a constant thickness structure were also addressed where it was shown that such ultrasonic waves are mostly dispersive, meaning their propagation velocities are dependent on their frequency content.

The use of analytical methods, in the form of the DISPERSE software, for determining the dispersion characteristics of the guided wave modes in waveguides with constant cross-section has also been discussed; this included the introduction of the dispersion curves and mode shapes of different modes as a function of their frequency as well as brief explanation of various frequency regimes associated with guided wave inspection.

Finally, FE analysis was introduced when dealing with waveguides with complex geometries/surface conditions. Here, the use of both 2-D and 3-D FE models have been elaborated which includes a brief description of key characteristics of each setup as well as parameters such as element sizes/types, excitation and reception methods and the overall pros and cons related to each FE model.

Chapter 3

Single-Mode Transduction in the High Frequency-Thickness Regime

As mentioned in previous chapters, guided wave inspection is used extensively in petrochemical plants to check for defects such as corrosion. Long range, low frequency inspection can be used to detect relatively large defects, while higher frequency inspection provides improved sensitivity to small defects, but the presence of multiple dispersive modes makes it difficult to implement. This chapter investigates the possibility of exciting a single mode Lamb wave with low dispersion at a frequency-thickness of around 20 MHz-mm. The A1 mode is chosen as it has low surface motion, making it insensitive to surface coatings, rough surfaces etc. and it will also only give a small reflection from features such as T-joints. However, the low surface motion also makes it difficult to excite.

The chapter starts with a discussion of previous work on guided wave inspection at high frequency-thickness products and identifies the higher order mode cluster (HOMC) method as being particularly interesting. It then goes on to investigate the modal composition leading to HOMC observations and, via analytical, numerical and experimental means, aims to study the possibility of single mode transduction at such frequency-thickness products. This work is published in IEEE Trans. Ultras. Ferr. Freq. Control 2016 [P1] and the chapter follows the structure of the paper.

3.1 Introduction

There has been growing attraction in guided wave testing at higher frequencies, especially at regions with limited access, as it is shown that the reflection from a surface obstacle such as a support reduces with frequency (Galvagni and Cawley, 2011) and this could also improve the sensitivity of the test to smaller, pitting-type defects.

Higher frequency guided modes have been used in a number of applications and have been extensively studied. Much work has been done in the frequency range around 100-300 kHz; for example, Alers et al. (Alers, 1994; Thompson et al., 1972) studied the reflection from a cylindrical surface defect with electromagnetic transducers at frequency-thickness products around 1.2 MHz-mm, while Köhler (Kehlenbach et al., 2003; Kohler et al., 2004) investigated the interaction of Lamb waves with drilled holes in an aluminium plate and the possibility of sizing them. Other examples include Salzburger (Salzburger et al., 2012; Salzburger, 1995) considering the use of guided shear waves for laser weld, pipe corrosion and crack inspection.

There has also been interest in testing over distances in the 1-5 m range at higher frequencies. For example, the multi-skip (M-skip) method (Burch et al., 2007; Lorenz and Lewandowski, 2012) uses angled shear waves bouncing between the plate/pipe surfaces in a pitch-catch configuration. Balasubramaniam (Balasubramaniam et al., 2012; Chandrasekaran et al., 2009, 2010; Jayaraman et al., 2009; Ratnam et al., 2012; Satyarnarayan et al., 2008; Swaminathan et al., 2011) has pioneered a technique he terms Higher Order Mode Cluster (HOMC) that uses Lamb modes in the ~20 MHz-mm frequency-thickness range to detect pitting and corrosion in plates and pipes. It has been used to inspect the annular ring of the base of oil storage tanks from the rim outside the tank wall; the low surface motion means that it propagates under the wall with minimal reflection (Chandrasekaran et al., 2009). Likewise propagation is insensitive to loading conditions at simple supports so it would be potentially attractive for monitoring pipe supports. The HOMC can be excited via a piezoelectric transducer and a wedge setup, the wedge angle corresponding to excitation of waves at close to the bulk shear velocity in the wave-guide (Balasubramaniam et al., 2012; Chandrasekaran et al., 2010; Jayaraman et al., 2009; Swaminathan et al., 2011). However it is not evident how waves with negligible out-of-plane surface displacement are excited nor is it clear which modes are excited and how they contribute to the formation of the reported cluster. Ratnam et al. (Ratnam et al., 2012) showed that HOMC can also be generated using EMATs but the waveforms obtained experimentally are more similar to a single, non-dispersive mode packet than the corresponding finite element predictions, leaving some uncertainty about the generation mechanism.

The phase velocity dispersion curves of the first six modes of an aluminium plate obtained using the DISPERSE software (Pavlakovic et al., 1997) are shown in Figure 3.1; aluminium is used here for comparison with Balasubramaniam (Jayaraman et al., 2009) but the curves for steel are very similar. Here the convergence of the A0 and S0 modes to the Rayleigh velocity is evident while other modes asymptote to the bulk shear velocity at high frequency-thickness products. The HOMC technique proposed by Balasubramaniam operates in the region around 20 MHz-mm indicated on the figure and the wedge angle used corresponds to a phase velocity of 3250 m/s i.e. ~4% higher than the bulk shear velocity.

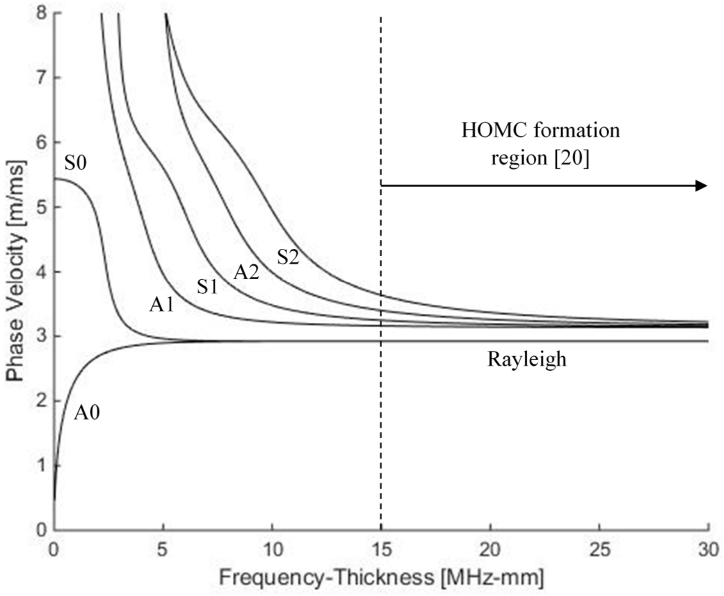

Figure 3.1: *Phase velocity dispersion curves of modes of interest in aluminium plate.*

This chapter studies the excitation of Lamb modes at high frequency-thickness products and investigates the possibility of single mode excitation within a high modal density region in the dispersion curves; it also looks at the modal composition leading to the HOMC observations. In order to understand the essential physics of the problem, a 2-D analysis was employed.

3.2 Prediction of Excitation Response via Mode Selectivity and Excitability

The response amplitude of a mode at a particular frequency/wavenumber excited within a waveguide is directly related to the product of the excitation force and the modal excitability at the corresponding frequency/wavenumber. With all forms of excitation, the frequency bandwidth is dictated by the nature of the excitation signal in time; typically in guided wave applications this is specified by the centre frequency, the number of cycles used and the window applied (Alleyne and Cawley, 1992a). Following Balasubramaniam et al. (Balasubramaniam et al., 2012; Chandrasekaran et al., 2009, 2010; Jayaraman et al., 2009; Satyarnarayan et al., 2008; Swaminathan et al., 2011), this chapter considers the case of excitation via a piezoelectric transducer on an angled wedge. Here the wavenumber bandwidth is determined by a combination of the transducer size and the wedge angle (Alleyne and Cawley, 1992a); these two parameters govern the projected excitation length on the surface of the plate as well as the phasing of the applied force as shown in Figure 3.2.

In order to calculate the excitation wavenumber bandwidth, the wedge configuration was simulated by phased point forces on the surface of the plate. Firstly the length of the line force (L) on the surface was obtained from transducer size (d) and wedge angle (θ) as defined in Figure 3.2; then the time delay between adjacent point forces was calculated according to the angle and the acoustic properties of the wedge. The excitation signal of each point force was determined according to the applied signal in time and its corresponding time delay. Finally a Fourier transform in space and time (2-D FFT) was used to calculate the excitation bandwidth. In this very simple model, a collimated beam in the wedge was assumed.

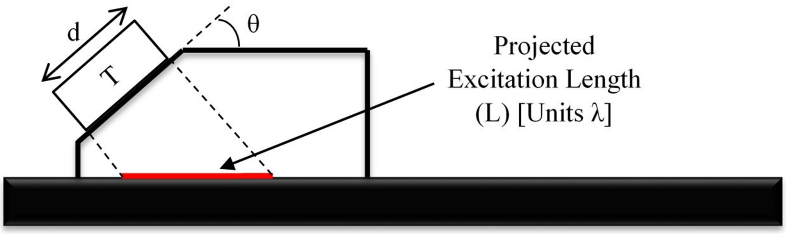

Figure 3.2: *Phased force excitation on surface of plate (red) to simulate angled wedge.*

3.2.2 Influence of excitation signal, transducer size and wedge angle on induced modes

At high frequency-thickness products, as the dispersion curves of higher modes asymptote to the bulk shear velocity, the generated modal response is very sensitive to the excitation configuration, so understanding the influence of each excitation parameter on the force bandwidths is vital. It should be noted that aluminium was used as the test plate to provide easy comparison to related studies (Jayaraman et al., 2009). However, the dispersion relationships for steel are very similar so the same broad conclusions can also be applied to steel (in both cases it was assumed that the material is isotropic).

Some examples of the effects of excitation length, wedge angle, window in space and signal in time are shown in Figure 3.3. The influence of projected excitation length (L) is illustrated in Figure 3.3a and 3.3b where the reduction of wavenumber bandwidth as the excitation length is increased from 2 to 15 wavelengths is apparent. Both figures are for a rectangular window excitation in space which produces multiple sidelobes, clearly seen in Figure 3.3b. In order to demonstrate the effect of a real piezoelectric transducer which does not produce a pure piston-like response, Figure 3.3c shows the effect of a Hanning window in space for the same excitation length and wedge angle as Figure 3.3b; here significant reduction of sidelobes is seen while the wavenumber bandwidth of the central lobe is increased.

Figure 3.3d shows the effect of increasing the excitation length to 40 wavelengths; this case corresponds to a 1 inch transducer on a 62° PMMA (c_L = 2692 m/s, ρ = 1180 kg/m3) wedge at centre frequency of 2.25 MHz. Figure 3.3e displays the effect of wedge angle reduction from 62° to 56° on the excitation force compared to Figure 3.3d; here the sensitivity of the modal excitation to the wedge angle is apparent –

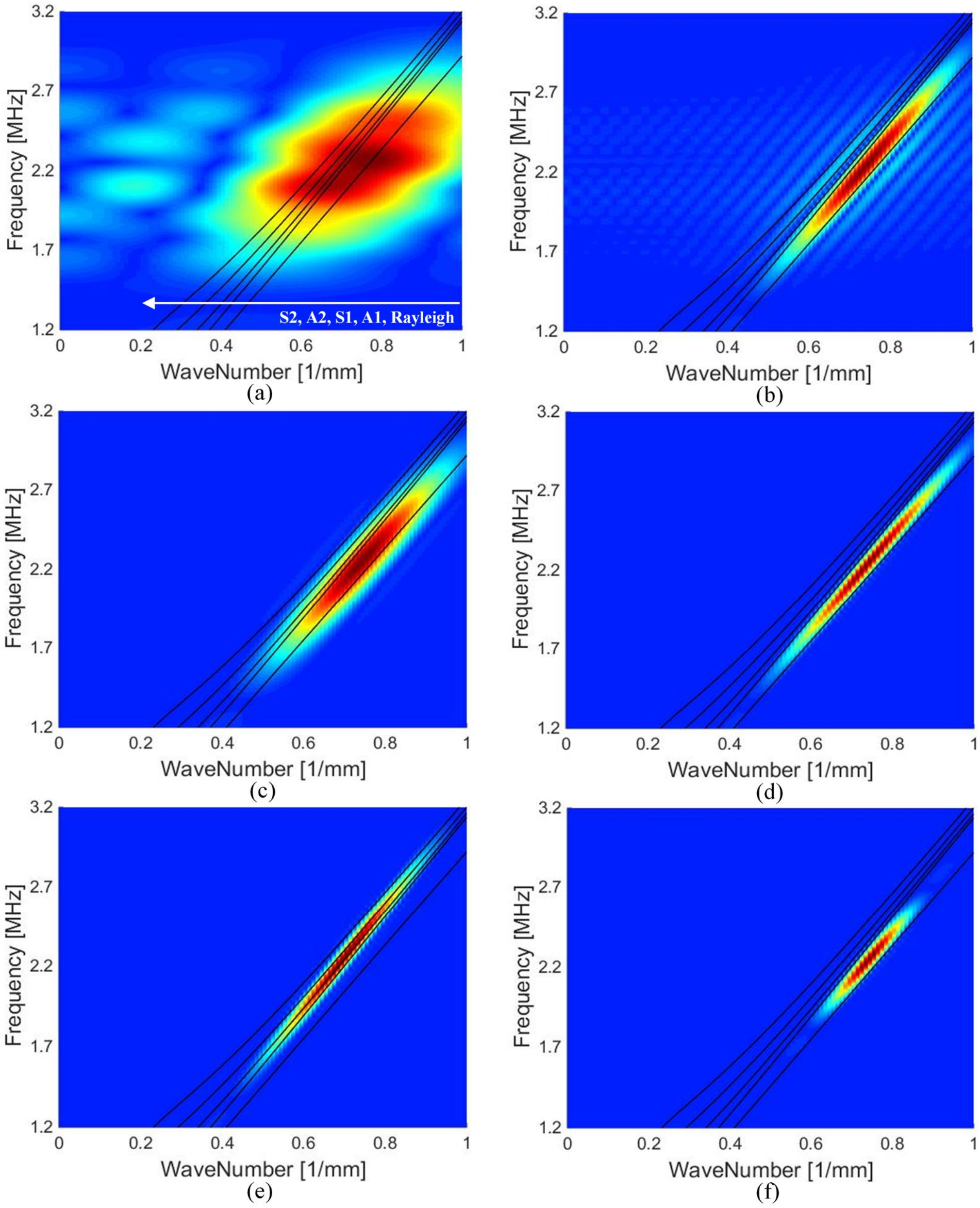

(a) (b) (c) (d) (e) (f)

Figure 3.3: *Examples of 2-D FFT colour plot (blue (low) – red (high) linear scale) for excitation configurations with respectively PMMA wedge angle, projected excitation length, number of cycles and window in time, window in space of (a) 62°, 2λ, 5 cycle toneburst in Hanning window, rectangular window in space (b) 62°, 15λ, 5 cycle Hanning, rectangular (c) 62°, 15λ, 5 cycle Hanning, Hanning (d) 62°, 40λ, 5 cycle Hanning, Hanning (e) 56°, 40λ, 5 cycle Hanning, Hanning (f) 62°, 40λ, 10 cycle Hanning, Hanning.*

at 62^0 (Figure 3.3d) the excitation is centred between the Rayleigh and A1 modes, while at 56^0 (Figure 3.3e) it is centred on the S1 mode. Finally, Figure 3.3f illustrates the reduction of frequency bandwidth by increasing the excitation signal from 5 to 10 cycles.

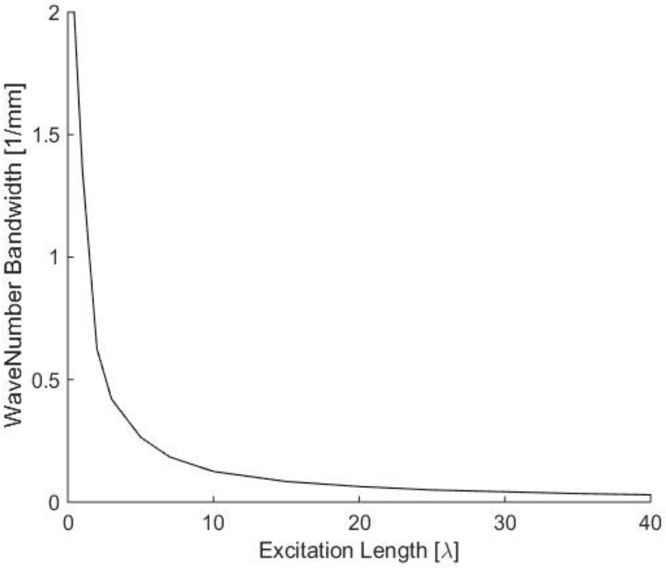

Figure 3.4: *10dB wavenumber bandwidth as function of projected excitation length (L) for time delay equivalent to 62° PMMA wedge along with Hanning window in space.*

Figure 3.4 shows the 10dB wavenumber bandwidth as a function of projected excitation length (L) for a 62° PMMA wedge and Hanning window in space setup. Here it is evident that for a single point excitation (L=0), the wavenumber bandwidth is infinite which results in excitation of all the modes present at the corresponding frequency-thickness product on the dispersion curves (Figure 3.1). Figure 3.4 also illustrates that the wavenumber bandwidth asymptotes to zero at high projected excitation lengths (measured in wavelengths), suggesting that single mode excitation in a high modal density region will be possible with a large transducer.

Guided wave inspection is often easier with a non-dispersive mode (Alleyne and Cawley, 1992a; Wilcox et al., 2001a) and the A1 mode is the least dispersive with lowest surface motion in the frequency-thickness range employed by Balasubramaniam et al. (Balasubramaniam et al., 2012; Chandrasekaran et al., 2009, 2010; Jayaraman et al., 2009; Ratnam et al., 2012; Satyarnarayan et al., 2008; Swaminathan et al., 2011); the deflected shape of the higher order mode cluster shown in [(Jayaraman et al., 2009), Figure 4] is also similar to that of the A1 mode. It was therefore decided to investigate the feasibility of exciting a pure A1 mode. It should be noted that while the Rayleigh wave provides completely non-dispersive properties, it exhibits large surface motion which means it is highly sensitive to surface loading and roughness, as well as surface coatings and attachments (Dransfeld and Salzmann, 1970).

It was decided to operate around 18 MHz-mm, as was done by Balasubramaniam et al. (Jayaraman et al., 2009), corresponding to a centre frequency of 2.25 MHz in an 8 mm thick plate. The wavelength at this frequency is 1.35 mm so the 40λ projected excitation length of Figure 3.3d corresponds to a transducer size of about 1 inch on a 62° wedge. Transduction was simulated, in the case of force bandwidth calculations and finite element analysis, by phased excitation via the application of time delays calculated according to the time of flight of the longitudinal wave in an angled PMMA wedge.

The excitation force bandwidth for a 1 inch transducer on a 62° PMMA wedge at a centre frequency of 2.25 MHz is illustrated in Figure 3.5. Here the presence of the sidelobes is clearly shown, but Hanning window weighting means their maxima are 32dB down compared to the central lobe.

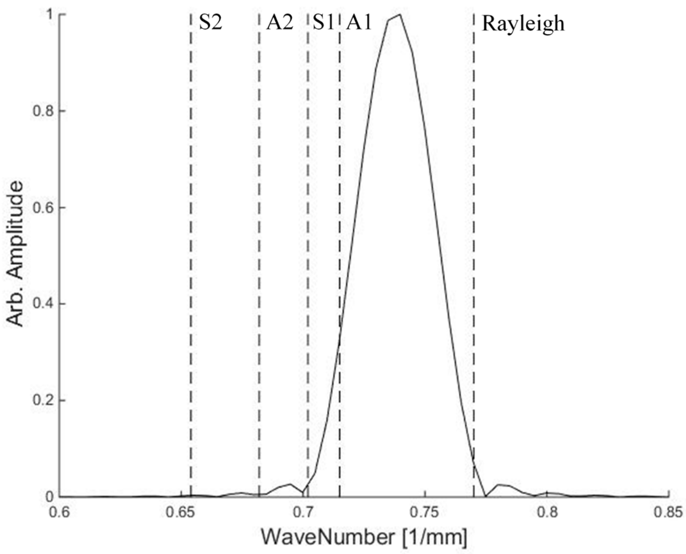

Figure 3.5: *Linear scale excitation amplitude wavenumber spectrum at centre frequency of 2.25MHz for 1 inch transducer, 62° PMMA wedge, 5 cycle Hanning window in time and Hanning window in space configuration.*

3.2.3 Excitability of Lamb waves generated using fluid coupled wedge

Excitability is defined as the parameter which relates the amplitude of the excitation force and the modal response of a particular mode at a specific frequency; the excitability of a mode is determined by its mode shape surface displacement at the excitation frequency of interest. The 2-D excitability of each mode can be obtained from (Wilcox, 2004):

$$E_k^{(2D)} = \frac{\omega}{4}\left(\frac{\upsilon_k}{\sqrt{P}}\right)^2 \tag{3.1}$$

where υ_k is the surface displacement of the mode shape (in desired direction k) and P is the power flow signified by the mode shape; the mode shapes are often normalized to give unit power flow (DISPERSE: User's Manual, 2013).

Figure 3.6 shows the excitability values of the modes of interest as a function of frequency-thickness product, where convergence of A0 and S0 to the Rayleigh mode is evident and the excitability of higher modes asymptote to zero at raised frequency-thickness values. It is clear that A1 exhibits the lowest excitability value within the non-dispersive region of the dispersion curve due to its low out-of-plane surface motion.

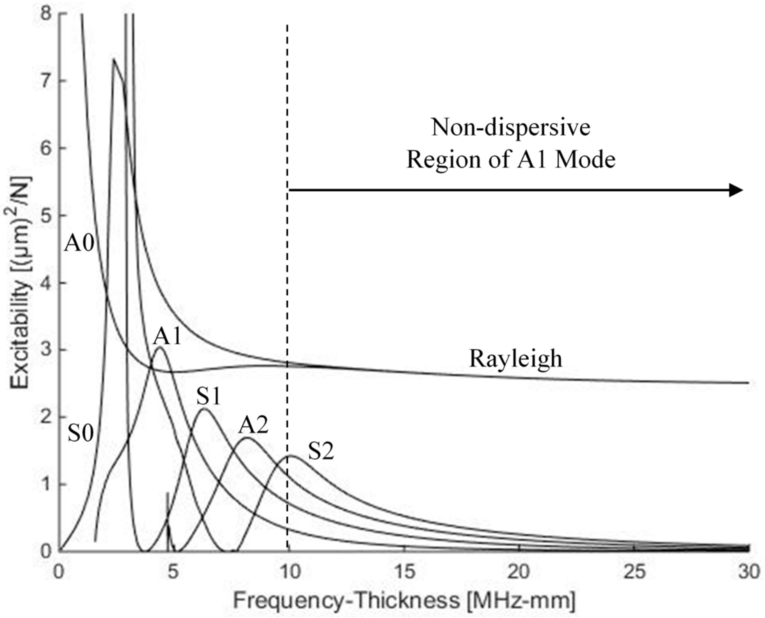

Figure 3.6: *Excitability of Lamb wave modes as a function of frequency-thickness for an out-of-plane line excitation for an aluminium plate.*

3.2.4 Modal response calculation

The response amplitude of the modes of interest as a function of wedge angle was obtained from:

$$R(\omega)_m = F(\omega)_m \times E(\omega)_m \tag{3.2}$$

where R is the modal response amplitude, F is the excitation amplitude from the force wavenumber spectrum (extracted from 2D FFT results, similar to Figure 3.5) and E is the excitability value (Figure 3.6); all three values are obtained for a specific forcing direction (out-of-plane in this study) on mode m at angular frequency ω.

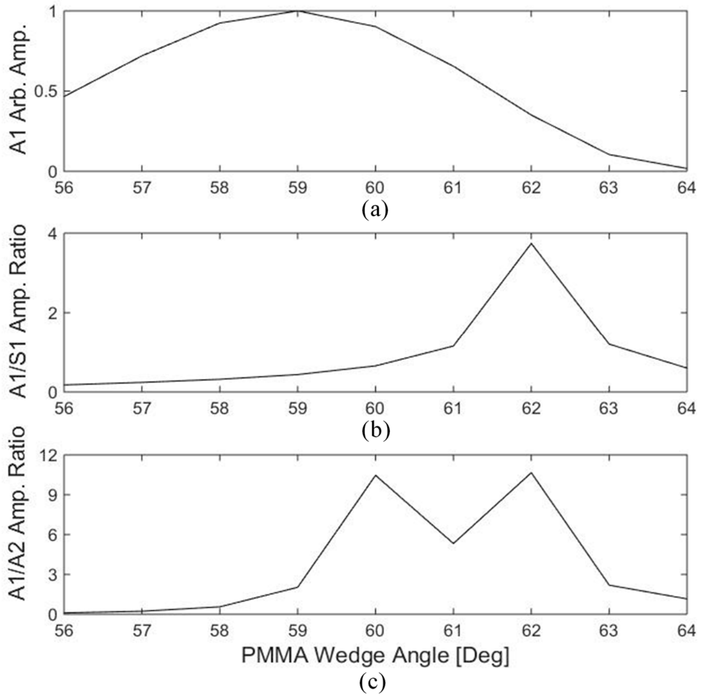

Figure 3.7: *Out-of-plane modal response characteristics of a 5 cycle Hanning window in time and Hanning window in space signal at centre frequency 2.25 MHz at surface as a function of PMMA wedge angle (a) A1 amplitude; (b) A1/S1 amplitude ratio; (c) A1/A2 amplitude ratio.*

Figure 3.7a shows the surface modal response amplitude in the out-of-plane direction of the A1 mode for wedge angles from 56° to 64°, the maximum amplitude being at 59°. However, the ratio of the amplitude of the mode of interest to that of other modes is often more important in the practical signal to noise ratio than the absolute amplitude; Figure 3.7b and 3.7c illustrate the A1/S1 and A1/A2 out-of-plane modal response amplitude ratios as a function of wedge angle respectively. It can be seen that a 62° angle provides the largest response amplitude ratios of A1 to both the S1 and A2 modes. The minimum in the A1/A2 ratio at a 61° wedge angle shown in Figure 3.7c was found to be caused by a sidelobe in the force wavenumber spectrum (Figure 3.5) that produced a local maximum in the amplitude of the A2 mode.

3.3 Finite Element Verification

In order to verify the validity of the selectivity and excitability predictions, finite element (FE) analysis was used, where excitation equivalent to that in the selectivity calculations was applied and the out-of-plane surface displacement was output along a line; a 2-D FFT was performed to identify the modes excited within the wave guide. To further establish the nature of each mode, in-plane and out-of-plane deflected shapes were obtained from a set of cross-sectional monitoring points.

3.3.1 FE model setup

The FE simulations were performed on the ABAQUS CAE package in a 2-D plane strain configuration. Figure 3.8 shows the overall FE simulation setup, where an 8 mm thick aluminium plate was created using CPS4R elements and to maintain stability and accuracy, appropriate time step (8 ns) and element size (square 0.05 mm) were applied. Excitation with a 1 inch transducer on a fluid coupled 62° PMMA wedge was simulated by phased out-of-plane point forces on the top surface of the plate while the excitation signal in time was a 5 cycle Hanning windowed toneburst at 2.25 MHz centre frequency. A 200 mm surface line scan was employed to perform the 2-D FFT which was used to identify the induced modes in the plate; also in order to obtain the deflected shapes of each mode, cross-sectional monitoring points were positioned approximately 710 mm from the excitation.

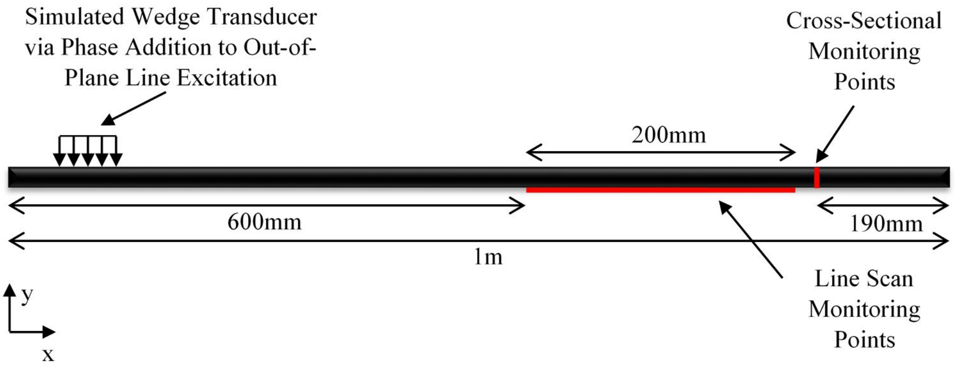

Figure 3.8: *Schematic of the FE setup and position of monitoring points.*

The monitoring line was placed on the opposite surface of the plate from the excitation, as shown in Figure 3.8. This was done in order to avoid the response being dominated by the Rayleigh wave that has very high excitability, as shown in Figure 3.6; the modes of interest have the same absolute amplitudes on the top and bottom surfaces. In practice the Rayleigh wave is heavily damped by leakage into the excitation wedge that extends beyond the excitation region, but for computational efficiency the wedge was not modelled in the main simulations. The damping of the Rayleigh wave was verified in a separate simulation in which a PMMA block of 100 mm length and 30 mm height was coupled to the plate after the excitation region in the out-of-plane direction to simulate a fluid coupled wedge; it was found that no significant Rayleigh wave was transmitted past the block, so validating the approach.

3.3.2 Modal decomposition with 2-D FFT

The 2-D FFT in space and time was performed on the out-of-plane displacement time traces recorded by the surface line scan located around 500 mm from the excitation. Figure 3.9 shows the 2-D FFT colour plot of the line scan where the presence of A1 mode is clearly displayed while S1 exhibits lower amplitude which correlates closely with the predictions from selectivity and excitability (Figure 3.7b and 3.7c).

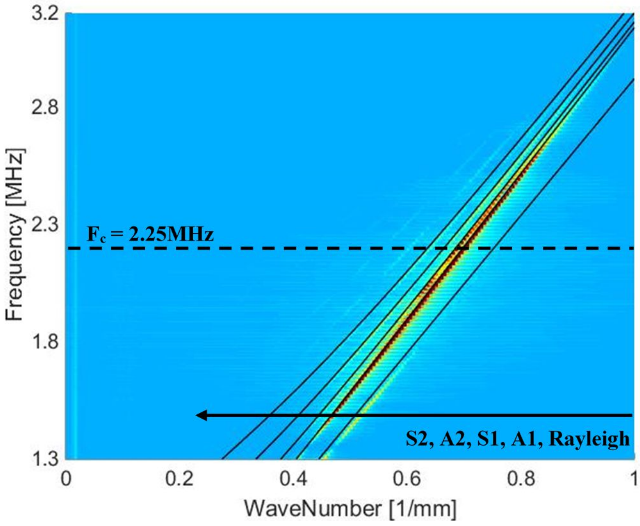

Figure 3.9: *2-D FFT colour plot (blue (low) – red (high) linear scale) of the out-of-plane displacement recorded in FE from surface line scan for a 5 cycle Hanning windowed toneburst in time and Hanning window in space excitation along with a 62° PMMA wedge angle at 2.25 MHz centre frequency.*

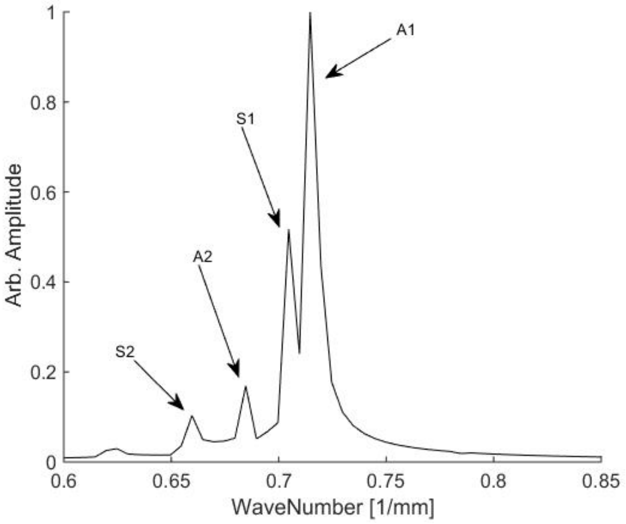

Figure 3.10: *Amplitude as a function of wavenumber at centre frequency (2.25MHz) obtained from 2-D FFT of surface displacement of Figure 3.9.*

Figure 3.10 illustrates the 2-D FFT amplitude of Figure 3.9 at the centre frequency (2.25 MHz) where each peak corresponds to a Lamb mode present within the plate.

3.3.3 Mode shape verification of excited modes

To further study the nature of the excited modes reported by the 2-D FFT, the in-plane and out-of-plane deflected shapes of each mode were obtained from the cross-sectional monitoring points positioned approximately 710 mm from the excitation.

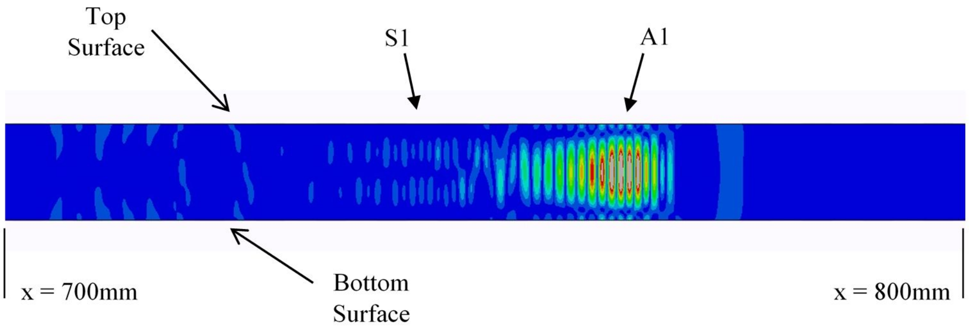

Figure 3.11: *FE displacement magnitude contour (blue (low) – red (high) linear scale) at time step of t=272 •s approx. 750 mm from the excitation.*

Figure 3.11 shows the displacement magnitude snapshot at 272 •s at around 750 mm from the excitation obtained from the FE results; due to small differences in group velocities, the A1 mode can be separated from smaller amplitude S1 mode.

Figure 3.12a and 3.12b show the deflected shapes recorded at around 710 mm from excitation at step times of 247 •s and 253 •s respectively. By comparing these figures with the mode shapes of different plate modes, it is clear that Figure 3.12a and 3.12b illustrate the deflected shapes of the A1 and S1 modes respectively; here it is clear that the A1 mode exhibits small surface motion which means lower sensitivity to surface loading. It is noteworthy that the deflected shape of Figure 3.12a correlates closely with the deflected shape of HOMC reported by Balasubramaniam [(Jayaraman et al., 2009), Figure 4].

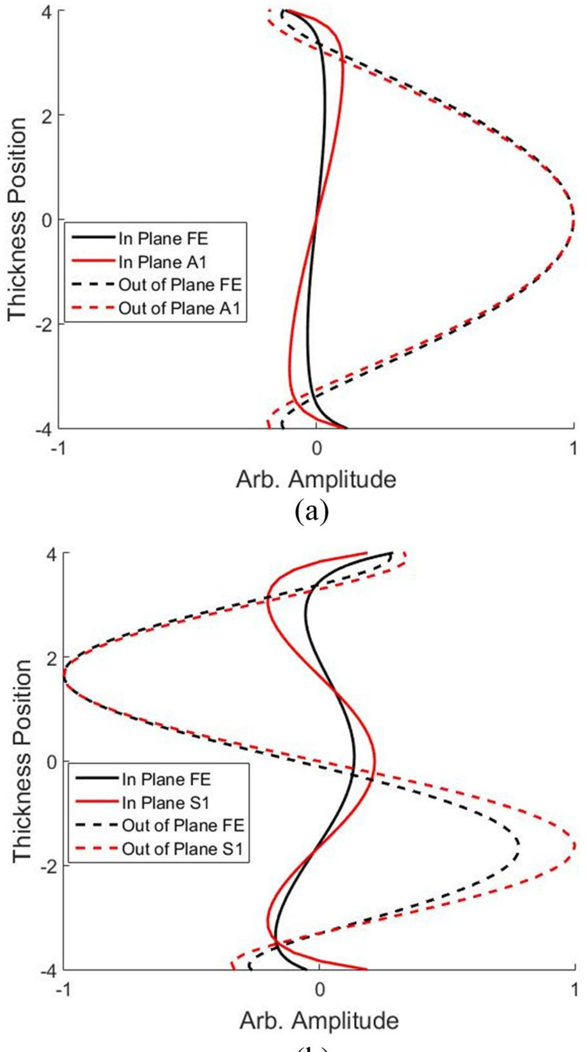

(a)

(b)

Figure 3.12: *Deflected shapes obtained from FE (Black) at cross-section located approx. 710 mm from excitation at step times (a) t=247 •s; (b) t=253 •s. Corresponding mode shapes from DISPERSE (Red) are also superimposed for comparison (a) A1 mode; (b) S1 mode.*

3.3.4 Wedge signal reception

In an experimental pitch-catch setup, the response signal is typically received via an angled wedge similar to that used for transmission (in pulse-echo the same wedge is used). To simulate this effect, phased addition of the surface out-of-plane surface displacements was performed.

Figure 3.13a shows the out-of-plane surface displacement time trace recorded at a single point approximately 600 mm from the excitation, where the presence of the A1 and S1 modes is clearly displayed. Figure 3.13b illustrates the time trace of the out-of-plane surface displacement signal received via a 1 inch transducer on a 62°

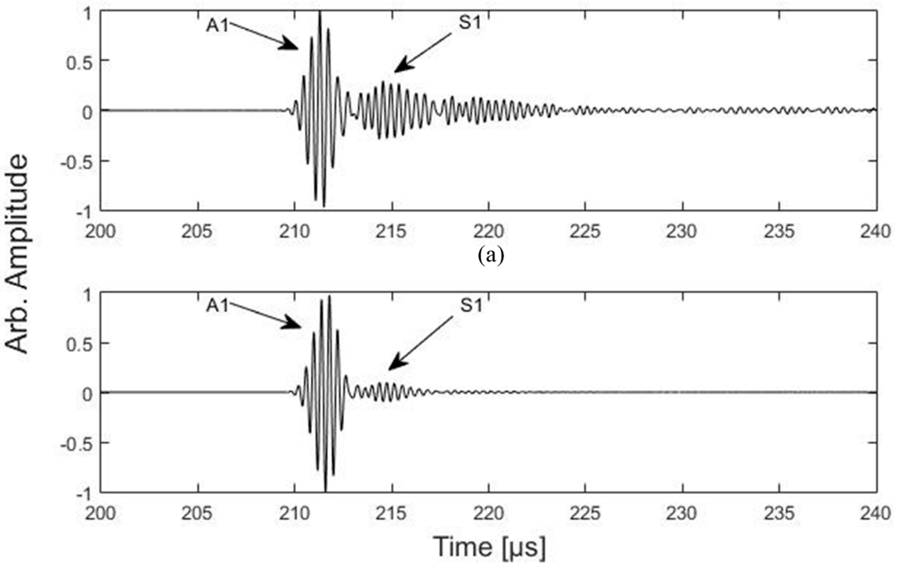

(a)

(b)

Figure 3.13: *Predicted pitch-catch time traces of out-of-plane displacement (centred at same point approx. 600 mm from excitation) generated by excitation setup of 62° PMMA wedge, 1 inch transducer, 5 cycle Hanning window in time (at centre frequency of 2.25 MHz) and Hanning window in space, received (a) at surface monitoring point; (b) with 1 inch transducer on 62° PMMA wedge (simulated by phased addition of surface amplitudes).*

PMMA wedge. Here the presence of A1 as a single mode is evident due to the selectivity process of the angled wedge. It should also be noted that, as expected, the A1 mode experiences minimal dispersion in the time traces of Figure 3.13.

3.4 Interaction of Pure A1 Mode with T-Joint

One application of guided wave inspection is the detection of corrosion in the annular ring of the base of oil storage tanks from the rim outside the tank wall; Chandrasekaran et al. (Chandrasekaran et al., 2009) report that the low surface motion of what they term a higher order mode cluster means that it propagates under the wall with minimal reflection. It is therefore of interest to investigate the interaction of the A1 mode at high frequency-thickness with a T-joint.

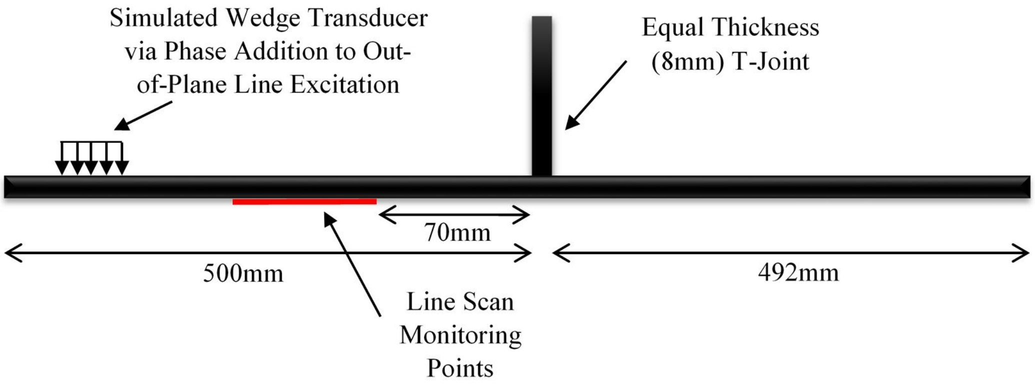

Figure 3.14: *Schematic of the positioning of the T-joint relative to the excitation.*

The joint considered was an 8mm thick aluminium plate rigidly attached to a similar plate at right angles to it; Figure 3.14 shows the FE simulation setup where in order to generate A1 as a single mode, a similar excitation configuration to that used above (1 inch transducer length, 5 cycle Hanning windowed toneburst in time at centre frequency 2.25 MHz, Hanning window in space and a 62° PMMA wedge) was applied. In order to quantify the reflection from the T-joint, a 100 mm surface line scan situated 70 mm behind the T-joint was employed. It should be noted that to avoid interaction with the Rayleigh wave, as with the previous simulations, the surface line scan was positioned on the bottom surface of the main plate.

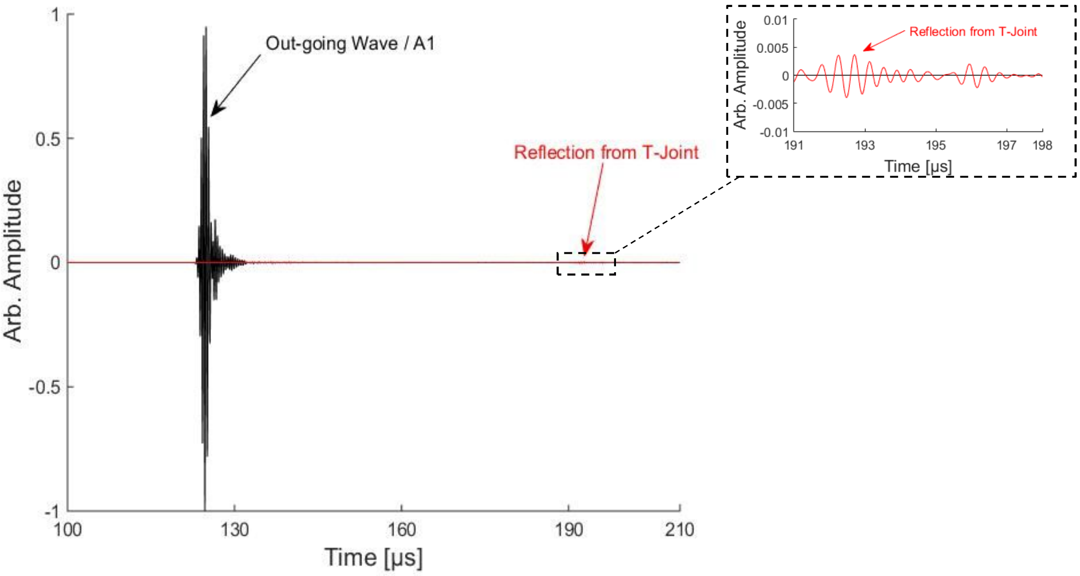

Figure 3.15: *Predicted 62° wedge reception time traces with 1 inch transducer from surface line scan situated 70 mm behind T-joint, in pitch-catch configuration for out-going wave (black) and reflected wave (red). Both measurements were simulated by phased addition of surface out-of-plane displacements.*

Figure 3.15 illustrates the superimposed time traces of the out-going (A1) mode and the reflected waves from the T-joint received with a 1 inch transducer on a 62° PMMA wedge where it is clear that virtually no reflection (~ -45dB amplitude ratio compared to the incident wave) is recorded. In order to simulate the wedge reception for the out-going and the reflected waves, the phased addition was carried out in opposite directions for the transmitted and received signals since the wave packets propagate in opposite directions.

3.5 Experimental Measurements

In order to establish the validity of the FE predictions on the possibility of pure mode excitation at high frequency-thickness values, experimental measurements on an aluminium plate were carried out. As with the FE simulations, a 2-D FFT was performed on the out-of-plane surface displacements recorded via a line scan. The presence of each mode was further confirmed through group velocity calculations.

3.5.1 Experimental setup

Figure 3.16 illustrates the configuration of the experimental setup used to obtain the out-of-plane surface displacements along a line on a 10 mm aluminium plate. Excitation was performed at 18 MHz-mm (1.8MHz centre frequency) via a 5 cycle Hanning windowed toneburst with a 1 inch diameter 2.25 MHz centre frequency piezoelectric compression wave transducer (Panametrics A104S-RB) on a gel coupled 63° PMMA wedge ($c_L = 2710$ m/s, •= 1188 kg/m^3). A 10 mm plate was used in the experiments since it was readily available, while an 8 mm plate was used in the predictions for comparison with the work of Balasubramaniam et al. (Jayaraman et al., 2009). Since the frequency-thickness values for the FE (8 mm Al plate) and the experiment (10 mm Al plate) are equal, the phase velocities of the A1 mode are the same, but the required wedge angles are slightly different since, as explained in section 3.2.4, for pure mode excitation, the aim is to maximise the ratio of the amplitude of the mode of interest to that of other modes rather than maximising the absolute amplitude of the mode of interest (where the wedge angle is constant for the same frequency-thickness product). Therefore a wedge angle of 63° was used in the experiments compared to 62° in the predictions to compensate for the change in centre frequency. To ensure an acceptable signal-to-noise ratio (SNR), the transducer was gel coupled to the wedge and held against it with a bolted clamp, and the wedge was gel coupled to the plate and pressed down with weights (not shown in Figure 3.16).

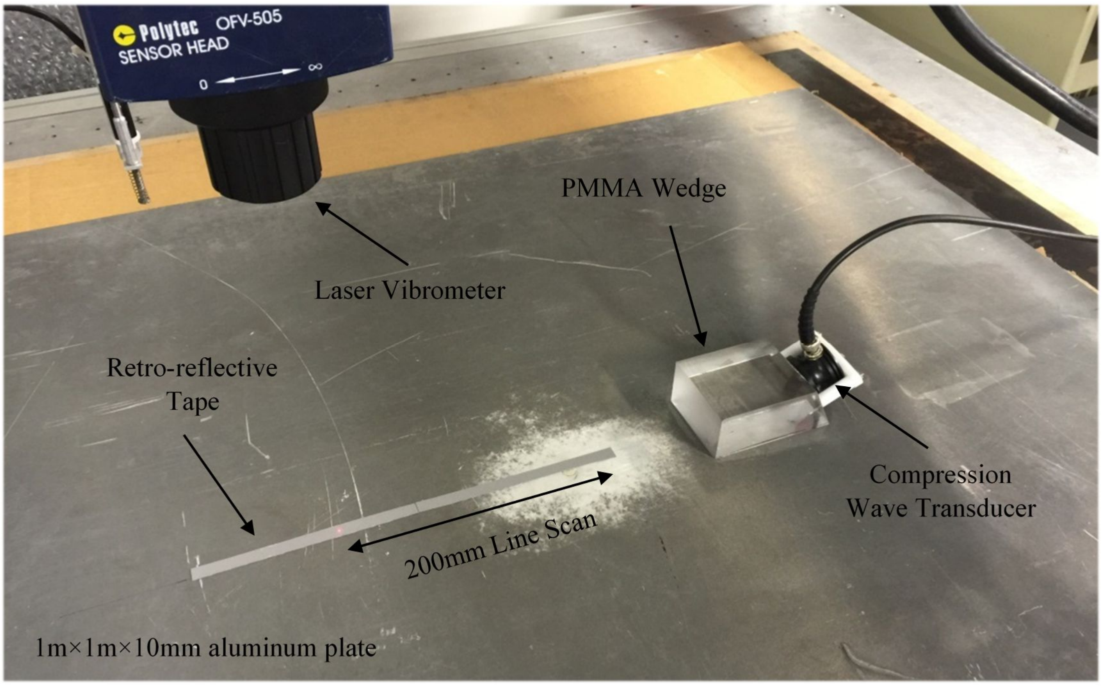

Figure 3.16: *Experimental setup schematic on 1 m × 1 m × 10 mm aluminium plate consisting of a compression wave transducer mounted on a gel coupled 63° PMMA wedge and reflective tape for a 200 mm line scan using the laser vibrometer.*

The toneburst was generated via a HandyScope HS3 connected to a computer. The excitation signal was amplified via a Wavemaker Duet wave generator and then fed to the transducer. The out-of-plane surface displacement was measured using a non-contact laser vibrometer (Polytec OFV-505 Sensor Head) from which the output was amplified using the wave generator and fed back to the HandyScope. In order to perform accurate line scans, the vibrometer was mounted on a 3-axis scanning frame where its position was controlled by the computer. To ensure sufficient resolution in the 2-D FFT, the line scan was performed over a 200mm distance at 0.5 mm steps and to improve SNR, 2000 averages were used for each measurement point.

3.5.2 Results

Similar to the FE results, a 2-D FFT in space and time was applied to the out-of-plane surface displacement time traces recorded in the line scan. The resulting amplitude plot is shown in Figure 3.17 where it is clear that A1 is the dominant mode, as predicted by the FE analysis of Figure 3.9.

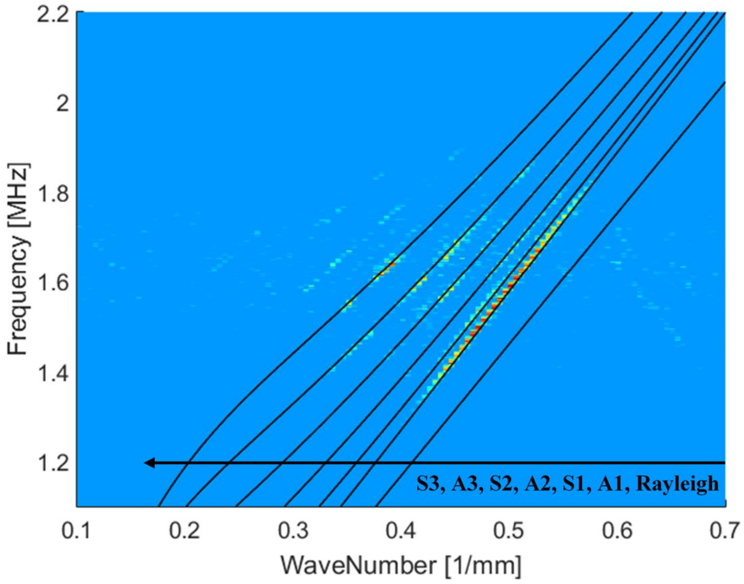

Figure 3.17: *2-D FFT colour plot (blue (low) – red (high) linear scale) of out-of-plane displacement recorded from surface line scan using a non-contact laser vibrometer for a 5 cycle, 1.8 MHz centre frequency Hanning windowed toneburst excitation signal generated via a 1 inch diameter compression wave transducer on a gel coupled 63° PMMA wedge.*

Figure 3.18 displays the out-of-plane surface displacement time trace at around 300 mm from the excitation recorded by the laser vibrometer after application of a 12dB/decade band-pass filter (6dB bandwidth 1.44 MHz - 2.16 MHz). Here the indicated A1 and S1 modes exhibit a 2:1 amplitude ratio which shows good agreement with the FE results (Figure 3.13a). It is noteworthy that as predicted by FE, the presence of the wedge was sufficient to completely attenuate the

Rayleigh wave. It should be stressed that Figure 3.18 shows a single point measurement similar to the predictions of Figure 3.13a; the S1 mode would be further suppressed relative to the A1 mode by receiving with a wedge transducer (due to reciprocity causing the suppression of other modes to square), as would be done in practical testing.

In order to further confirm the nature of each mode, the group velocity of the wave packets was obtained through time-of-flight calculations, the peak of each wave packet being obtained from a Hilbert transform of the time trace. The dominant wave packets of Figure 3.18 had group velocities of 3150 m/s and 3000 m/s which are within 1.5% and 1% respectively of the A1 and S1 group velocities obtained from the DISPERSE software.

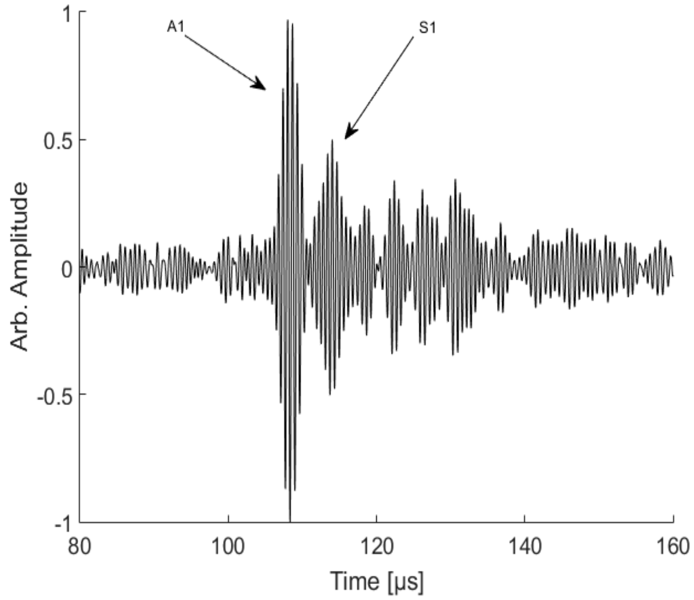

Figure 3.18: *Measured out-of-plane surface displacement at a single point approx. 300mm from excitation generated by a 5 cycle Hanning windowed toneburst at 1.8MHz centre frequency excitation signal from a 1 inch compression wave transducer on a gel coupled 63° PMMA wedge.*

3.6 Conclusions

The possibility of exciting a single mode Lamb wave with low dispersion at a frequency-thickness of around 20 MHz-mm has been investigated. Numerical predictions of the modal response were obtained from mode selectivity and excitability calculations; these were then used to obtain the optimum excitation configuration to enable pure mode generation. It was found that given the small wavelengths at high frequencies, a typical ultrasonic transducer is many wavelengths in diameter, allowing the excitation to be centred on a narrow wavenumber bandwidth which provides the possibility of pure mode generation, even though the modes appear close together in the dispersion curves.

Excitation of the A1 mode was considered due to its non-dispersive nature and low surface motion at high frequency-thickness products; this makes it attractive for NDE as it will be relatively unaffected by surface roughness and attenuative coatings. Using selectivity calculations, the appropriate excitation setup for pure A1 mode generation was established and applied to FE simulations. A 2-D FFT was performed on predicted out-of-plane surface displacements recorded in the form of a line scan. The results showed that a signal dominated by the A1 mode could be generated. Balasubramaniam et al. (Balasubramaniam et al., 2012; Chandrasekaran et al., 2009, 2010; Jayaraman et al., 2009; Ratnam et al., 2012; Satyarnarayan et al., 2008; Swaminathan et al., 2011) used a very similar configuration to generate what they term a higher order mode cluster (HOMC); the HOMC deflected shape they report (Jayaraman et al., 2009) is very similar to the mode shape of the A1 mode and the group velocity of A1 mode is within 2% of the reported HOMC group velocity (Jayaraman et al., 2009).

The low sensitivity of the A1 mode to surface features was examined in FE by studying the interaction of the A1 mode at 18 MHz-mm with a T-joint, virtually no reflection being obtained. Again, this is in line with the reported features of HOMC.

Experimental measurements were performed on a 10 mm aluminium plate to validate the predictions; the modal decomposition was carried out using a 2-D FFT on out-of-plane surface displacements obtained via a line scan with a laser vibrometer. The measurements showed good agreement with the predicted results, confirming the possibility of pure mode generation at high frequency-thickness products.

Chapter 4

Transducer Selection for Single-Mode Transduction

Ultrasonic guided waves are mostly generated using piezoelectric transducers on an angled wedge or EMATs in different configurations. At higher frequencies, the presence of multiple wave modes limit defect detectability, so achieving practical single Lamb mode excitation via careful transduction is very beneficial. This chapter investigates the relative ability of angled piezoelectric and meander coil EMAT probes to produce single mode transduction in the medium (~1 to 5 MHz-mm) and high (> 5 MHz-mm) frequency-thickness regions of the dispersion curves.

Firstly, the nature of each transducer is investigated via analytical means in order to understand the fundamental physics; the predictions are then used to obtain the appropriate probe configuration for each of the transducer types which is necessary for single-mode excitation of chosen modes at medium and high frequency-thickness regimes. The chapter then goes on to validate these predictions experimentally and demonstrates the advantages and disadvantages of each type of transducer in different regimes. This work is in print at the IEEE Trans. Ultras. Ferr. Freq. Control 2018 [P3] and the chapter follows the structure of the paper.

4.1 Introduction

Low frequency transduction is commonly achieved through an array of point sources which can be done via direct contact piezoelectric transducers (PZT) (Belanger et al., 2010; Clarke et al., 2009; Ning Hu et al., 2008), ring excitation with electromagnetic acoustic transducers (EMATs) (Herdovics and Cegla, 2016; Seher et al., 2014, 2015) or magnetostrictive probes (Kim et al., 2005; Vinogradov, 2009). The medium frequency regime from 1 MHz-mm to around 5 MHz-mm gives better sensitivity to smaller defects but the presence of multiple and often dispersive modes limits defect detectability with this method (Alleyne and Cawley, 1992a, 1992b; Ditri et al., 1992; Hay and Rose, 2002; Quarry and Rose, 1999; Rose et al., 1998; Wilcox et al., 1997, 2001a). Here the transduction is usually achieved via piezoelectric transducers mounted on an angled wedge (Ditri et al., 1993; Li and Rose, 2001; Rose, 2002, 2014; Wilcox et al., 2002) or EMATs (Dixon and Palmer, 2004; Guo et al., 1997; Salzburger et al., 2012; Salzburger, 2009; Thompson et al., 1972). As mentioned before, there has also been interest in guided wave testing over the 1 – 5m range at much higher frequencies (> 5 MHz-mm); such as the introduction of HOMC (Chandrasekaran et al., 2009, 2010; Jayaraman et al., 2009; Ratnam et al., 2012; Satyarnarayan et al., 2008; Swaminathan et al., 2011) while in Chapter 3 we have shown that the features of HOMC are essentially those of the A1 mode in this frequency-thickness regime (Khalili and Cawley, 2016). There have also been studies that use high a frequency Rayleigh wave to test for sharp surface cracks (Hirao et al., 1982; Masserey and Fromme, 2009, 2013). The generation of higher order Lamb waves is mostly achieved via piezoelectric transducers mounted on an angled wedge (Chandrasekaran et al., 2009, 2010; Hirao et al., 1982; Jayaraman et al., 2009; Khalili and Cawley, 2016; Masserey and

Fromme, 2009, 2013; Satyarnarayan et al., 2008; Swaminathan et al., 2011) with fewer applications of EMATs (Ratnam et al., 2012).

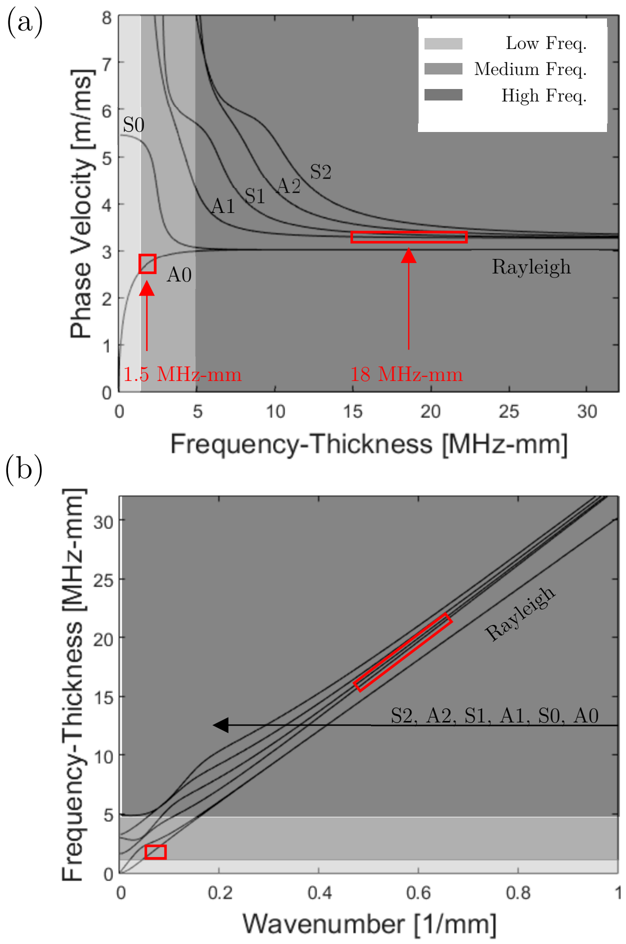

Figure 4.1: *Lamb wave dispersion curves in steel plate showing (a) phase velocity; (b) wavenumber; generated using DISPERSE (Pavlakovic et al., 1997) software.*

A challenge faced by guided wave inspection is the presence of multiple wave modes, particularly in the medium and high frequency regimes, so achieving practical single Lamb mode excitation through careful transduction is very beneficial (Guo et al., 1997; Khalili and Cawley, 2016; Seher et al., 2014, 2015). The excitation of a pure mode can be very difficult at high frequency-thickness products as the Lamb modes exhibit very similar dispersion characteristics as shown in Figure 4.1.

As stated above, guided waves are mostly generated using piezoelectric transducers on an angled wedge and EMATs in different configurations; however, practical single mode excitation with each type of transducer is less investigated, particularly at higher frequencies. This chapter studies the relative ability of angled PZT and EMAT probes to give pure mode excitation in the medium and high frequency-thickness regimes. For the medium frequency case, the A0 mode at 1.5 MHz-mm was chosen as it offers good application potential in structural health monitoring (SHM) (Clarke et al., 2008, 2009; Ning Hu et al., 2008; Xu and Giurgiutiu, 2007); the A1 mode at 18 MHz-mm was studied for the high frequency case as it provides desirable characteristics for corrosion inspection especially at inaccessible regions as discussed in Chapter 3 and further in Chapter 5 (Chandrasekaran et al., 2009, 2010; Jayaraman et al., 2009; Khalili and Cawley, 2016; Ratnam et al., 2012; Satyarnarayan et al., 2008; Swaminathan et al., 2011).

Section 4.2 gives a brief background on the governing physics of piezoelectric transducers on an angled wedge and meander coil EMATs and the design parameters which determine their ability to generate a single mode. Section 4.3 then introduces the analytical prediction of the excitation force bandwidths for a given setup through the use of a Fourier transform in time and space (2-D FFT). Then these predictions are verified experimentally in Section 4.4 and the findings are summarised in section 4.5.

4.2 Background

Guided waves are often generated by piezoelectric probes where the vibration of the piezoelectric crystal is transmitted to an angled wedge that is connected directly to the surface of the structure through the use of a couplant. This provides strong signal amplitudes and can be implemented with basic equipment but requires direct contact so inconsistent coupling over the footprint, particularly over curved or rough surfaces, is a problem; there are also issues with poor high temperature performance (Attarian et al., 2014) and reverberations within the wedge.

Figure 4.2 shows a schematic of a piezoelectric transducer mounted on an angled wedge. In this configuration, the frequency bandwidth is governed by the nature of the excitation signal in time; typically, for guided wave applications, this is specified by the centre frequency, the number of cycles used and the window applied (Khalili and Cawley, 2016; Rose, 2014). The wavenumber bandwidth is determined by a combination of the wedge angle (θ) and the transducer size (d); these parameters dictate the projected excitation length (L) as well as the phasing of the force acting on the surface of the waveguide, as shown in Figure 4.2. The key characteristic of the angled wedge assembly is that the frequency and wavenumber bandwidths are interdependent, meaning that if the frequency content (ω) is changed, it causes the wavelength within the wedge (λ_w) and hence the induced wavelength on structure surface (λ) to change which consequently results in a change in the number of cycles in space (L/λ), thus affecting the wavenumber (k) bandwidth. This characteristic can be formulated as:

$$k_w = \frac{\omega}{c_{Lw}} \tag{4.1}$$

where k_w, c_{Lw} and ω are the wedge wavenumber, longitudinal wave velocity in the wedge and the angular frequency respectively. The wavenumber within the wave guide (k) is:

$$k = \frac{\omega}{c_p} \tag{4.2}$$

where c_p is the phase velocity of the guided wave mode of interest.

As illustrated in Figure 4.2b, the coupling mechanism can be stated:

$$\lambda = \frac{\lambda_w}{\sin(\theta)}\ so\ k = k_w \sin(\theta) \tag{4.3}$$

From (4.3) and (4.1),

$$k = \frac{\sin(\theta)}{c_{Lw}}\omega \tag{4.4}$$

Equation (4.4) shows that the relationship between frequency and wavenumber can be represented as a straight line with a constant slope of $\frac{\sin(\theta)}{c_{Lw}}$ in the frequency-wavenumber spectrum. Therefore the frequency-wavenumber relationship of the wedge excitation runs roughly parallel to most regions of the dispersion curves of Figure 4.1b.

Guided wave inspection is often done using a broadly non-dispersive mode (Alleyne and Cawley, 1992a) where excitation at constant phase velocity, c_p, with frequency is achieved with a constant wedge angle. Therefore for ideal modal selectivity, the wedge angle (θ) can be calculated:

$$\sin(\theta) = \frac{c_{Lw}}{c_p}. \tag{4.5}$$

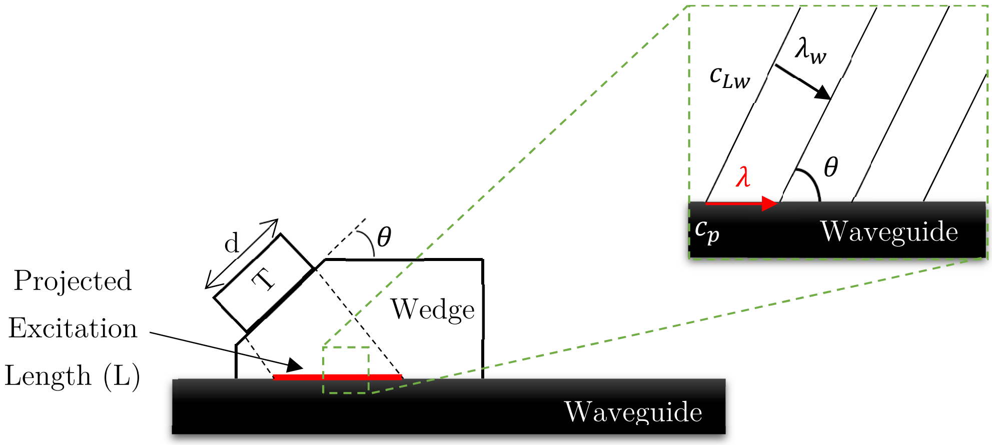

Figure 4.2: *Transducer schematic of the piezoelectric transducer mounted on an angled wedge; inset shows the relationship between the wavelengths of the compression wave in the wedge and the guided wave in the waveguide.*

EMATs on the other hand rely on the interaction of the dynamic magnetic field of the eddy currents generated by a coil and the bias magnetic field of a permanent (or electro-) magnet to produce a force resulting in generation of elastic waves in the structure (Mirkhani et al., 2004). Hence they do not require direct contact which eliminates the need for a couplant; this allows transduction over coatings/paint and rough surfaces and also good high temperature/long term performance; however, they suffer from poor signal-to-noise ratio (SNR) and often require bulky and expensive electronics.

A typical configuration of a meander coil EMAT is shown in Figure 4.3 (Mirkhani et al., 2004; Thompson, 1990; Thompson et al., 1974). Similar to the piezoelectric probe, the frequency bandwidth is determined by the nature of the excitation signal in time; in contrast, however, the wavenumber bandwidth is dictated by the geometry of the meander coil: the wavelength (λ) and the number of cycles in space, as shown in Figure 4.3. Therefore due to the nature of the design, the frequency and wavenumber bandwidths are fully decoupled and independent of each other.

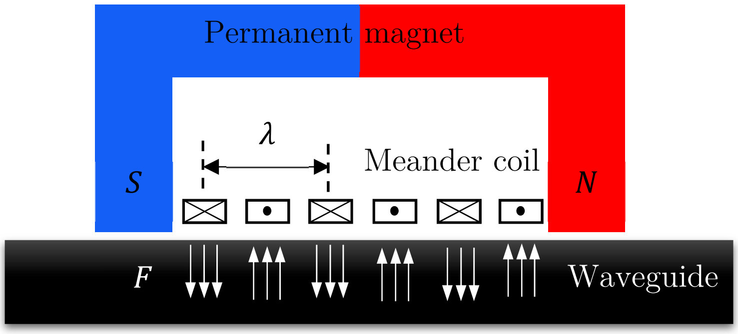

Figure 4.3: *Transducer schematic of an out-of-plane Meander coil EMAT. Note that the cross and dots represent the in and out directions of the current flow in the meander coil.*

For ideal modal selectivity in the case of a meander coil EMAT, for a given frequency, the wavelength of the coil (λ) is chosen according to the wavelength of the mode of interest, while the frequency and wavenumber bandwidths must be carefully calculated in order to minimize the excitation of the unwanted guided modes. In the case of other transducer designs such as periodic permanent magnet (PPM) EMATs and magnetostrictive devices, the wavenumber bandwidth (and thus selectivity) is also determined by the periodicity of the coil or magnets (Hirao and Ogi, 1999; Ribichini et al., 2011; Vasile, 1978; Vasile et al., 1981).

4.3 Analytical Prediction of the Excitation Force Bandwidths

The response amplitude of a mode in a waveguide at a particular frequency/wavenumber is directly related to the excitation force acting on the surface at the corresponding frequency/wavenumber (Wilcox, 2004). As mentioned above, the frequency and wavenumber bandwidths are dictated by the nature of the transducer design so it is necessary to investigate how to obtain the optimal setup for pure mode excitation in different frequency-thickness regimes for each transducer type. Here a simple analytical model, implemented in the MATLAB software, was employed as it can produce the essential physics while enabling the study of a large number of probe configurations practically. In order to predict the wavenumber and frequency bandwidths of the excitation force, the surface force generated by each transducer was simulated by out-of-plane surface forces followed by the use of a Fourier transform in space and time (2-D FFT). It should be noted that steel was used as the test plate throughout this study. However, the dispersion relationships for aluminium are similar so the same broad conclusions can also be applied to aluminium (in both cases, it was assumed that the material is isotropic).

In the case of a piezoelectric transducer mounted on an angled wedge, the length of the line force (L) on the surface was obtained from the transducer size (d) and wedge angle (θ) as shown in Figure 4.2; then, the time delay as a function of distance along the surface was calculated according to the angle (θ) and the acoustic properties of the wedge (c_{Lw}) (Khalili and Cawley, 2016). In this simple model, a collimated beam in the wedge was assumed.

The force pattern for the meander coil EMAT was determined by out-of-plane surface forces with opposite polarity depending on the direction of the acting Lorentz force (F), as shown in Figure 4.3; this pattern is repeated according to the wavelength (λ) and the number of cycles of the coil in space. Here, for simplicity, the force acting on the surface was assumed to be constant across the width of the coil “finger” (Monkhouse et al., 1997). The excitation signal for each coil finger was therefore determined by the applied signal in time and the polarity of the Lorentz force.

4.3.1 Medium frequency-thickness regime

As an example of the use of the two transducer types in the medium frequency-thickness regime, this section investigates the relative ability of each transducer type to generate a pure A0 mode at around 1.5 MHz-mm (150 kHz centre frequency on a 10 mm thick steel wave guide). Different practical excitation setups were studied for each of the transducer designs through the use of 2-D FFT; for brevity, only the desired excitation configurations are presented in this chapter.

Figure 4.4a shows the excitation force amplitude in frequency-wavenumber space for a 25.4 mm (1 inch) compression wave piezoelectric transducer mounted on a 70° PMMA ($c_{Lw} = 2710$ m/s, $\rho = 1180$ kg/m^3) wedge where the excitation signal in time consists of a 5-cycle Hanning windowed toneburst at a centre frequency of 150 kHz. In order to demonstrate the effect of a real piezoelectric transducer that does not produce a pure piston-like response, a Hanning window in space was employed; this allows for significant reduction of sidelobes while the wavenumber bandwidth of the central lobe is increased compared to a piston-like response (not shown here) (Khalili and Cawley, 2016). Here it was found that a 25.4 mm (1 inch) piezoelectric transducer is sufficiently large to achieve a narrow enough wavenumber bandwidth to suppress the undesired wave modes. Figure 4.4a also displays a mismatch between the position of the peak force amplitude and the A0 mode dispersion curve; this is because the phase velocity of the A0 mode at 1.5 MHz-mm ($c_p = 2610$ m/s) is smaller than the longitudinal wave velocity in the PMMA wedge ($c_{Lw} = 2710$ m/s) and as demonstrated by equation (4.5), ideal selectivity cannot be achieved with PMMA wedge excitation.

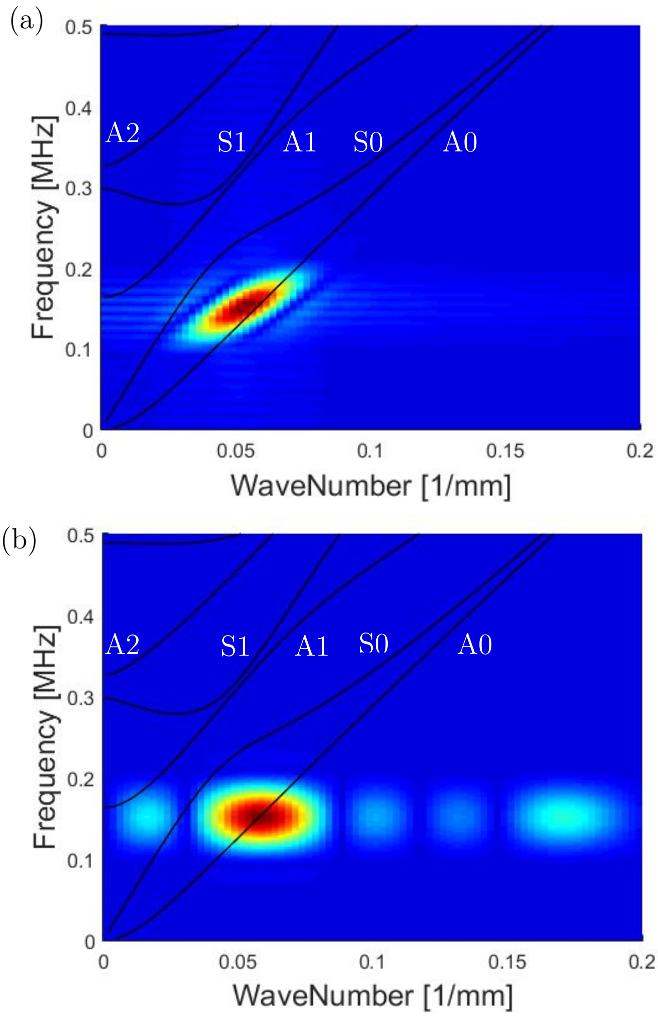

Figure 4.4: *2-D FFT colour plot [blue (low)–red (high) linear scale] showing the excitation force amplitude in frequency-wavenumber space of (a) 25.4 mm (1 inch) compression wave piezoelectric transducer mounted on a 70° PMMA wedge with a 5-cycle Hanning windowed toneburst signal in time at a centre frequency of 150 kHz; (b) 2-cycle meander coil EMAT with a 17 mm wavelength in space and a 5-cycle Hanning windowed toneburst signal in time at a centre frequency of 150 kHz.*

Figure 4.4b illustrates the excitation force amplitude for a 2-cycle meander coil EMAT with a 17 mm wavelength in space (λ) and a 5-cycle Hanning windowed toneburst signal in time at a centre frequency of 150 kHz. It can be seen that due to the evident separation of the A0 and S0 dispersion curves, the use of a 2-cycle coil in space and a 5-cycle toneburst signal in time provides sufficiently narrow wavenumber and frequency bandwidths for pure A0 mode excitation. Also, as shown in Figure 4.4b, the sidelobes do not coincide with the undesired modes, hence maintaining pure mode excitation.

4.3.2 High frequency-thickness regime

The example studied in the high frequency-thickness regime concerns the relative ability of each transducer type to produce pure mode excitation of the A1 mode at 18 MHz-mm (1.8 MHz centre frequency on a 10 mm thick steel wave guide). As above, a 2-D FFT is used to calculate the frequency and wavenumber bandwidths in order to find the optimum setup for the best selectivity.

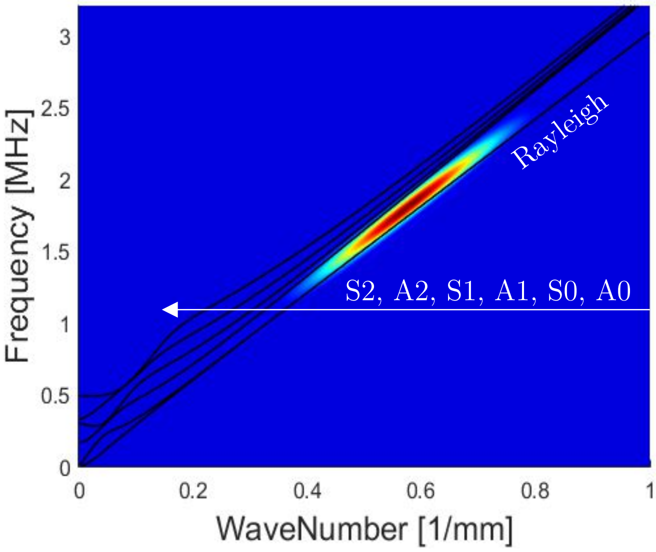

Figure 4.5: *2-D FFT colour plot [blue (low)–red (high) linear scale] showing the excitation force amplitude in frequency-wavenumber space of a 25.4 mm (1 inch) compression wave piezoelectric transducer mounted on a 60° PMMA wedge with a 5-cycle Hanning windowed toneburst signal in time at a centre frequency of 1.8 MHz.*

Figure 4.5 shows the excitation force amplitude in frequency-wavenumber spectrum for a 25.4 mm (1 inch) compression wave piezoelectric transducer mounted on a 60° PMMA wedge where the excitation signal in time consists of a 5-cycle Hanning windowed toneburst at a centre frequency of 1.8 MHz; as before, a Hanning window in space was also applied along the projected length (L) in order to mimic the real response of a piezoelectric transducer. As predicted [by equation (4.4)], the relationship between the frequency and wavenumber of the wedge excitation is represented as a straight line with a constant slope in the frequency-wavenumber spectrum which, as shown in Figure 4.5, runs roughly parallel to the dispersion curves; this means that the frequency bandwidth, which is determined by the signal in time, plays a less crucial role in the selectivity process. Therefore for a fixed centre frequency, the selectivity is dictated by the size of the transducer and the angle of the wedge (Khalili and Cawley, 2016).

Figure 4.6a illustrates the excitation force amplitude for a 30-cycle meander coil EMAT with a 1.8 mm wavelength in space (λ) and a 5-cycle Hanning windowed toneburst signal in time at a centre frequency of 1.8 MHz. Here it is clear that the frequency and wavenumber bandwidths are completely independent of each other, which results in a gradient mismatch between the dispersion curves and the excitation force distribution. This means that pure mode excitation of the A1 mode is not possible with a similar signal in time to that used for the wedge excitation. Consequently, in order to suppress the excitation of the other modes compared to the A1 mode, a narrower frequency bandwidth is required.

Figure 4.6b illustrates the excitation force amplitude for the same meander coil (30-cycle with a 1.8 mm wavelength in space) but with a 50-cycle Hanning windowed toneburst signal in time at a centre frequency of 1.8 MHz. The significant narrowing of the frequency bandwidth is clearly evident which provides better selectivity of the A1 mode. It should be noted that due to the small wavelength of A1 at 18 MHz-mm (~1.8 mm in a 10 mm thick plate), the 50-cycle signal in time maintains good spatial resolution (compared to conventional long range/low frequency guided wave methods) as the total pulse width is around 90 mm.

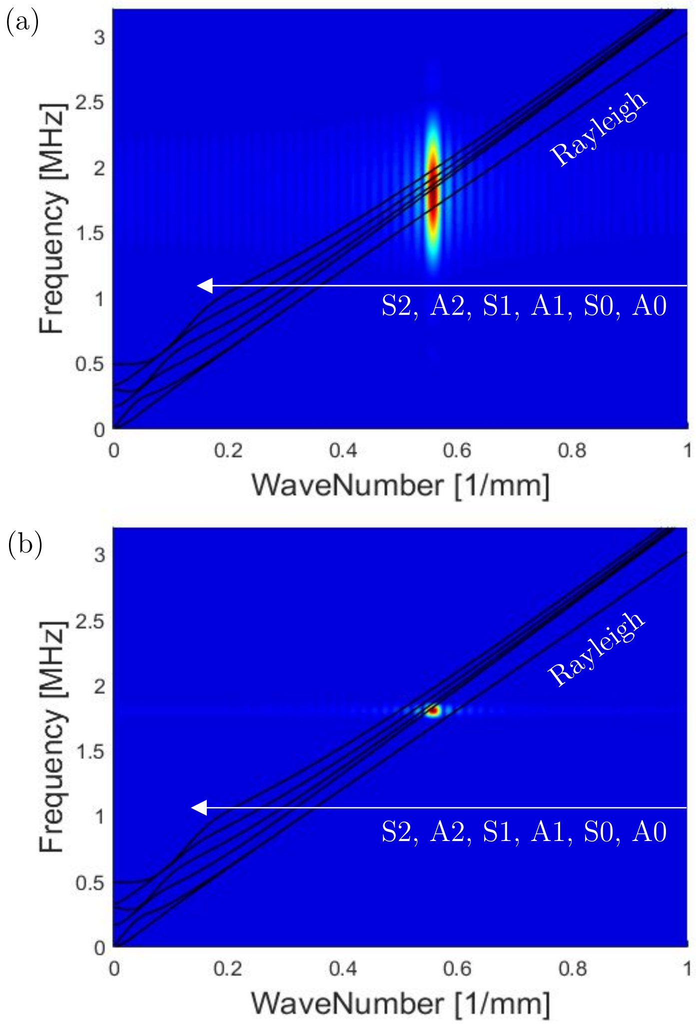

Figure 4.6: *2-D FFT colour plot [blue (low)–red (high) linear scale] showing the excitation force amplitude in frequency-wavenumber space of a 30-cycle meander coil EMAT with a 1.8 mm wavelength in space and an excitation signal in time of (a) 5-cycle Hanning windowed toneburst at a centre frequency of 1.8 MHz; (b) 50-cycle Hanning windowed toneburst at a centre frequency of 1.8 MHz.*

4.4 Experimental Validation

In order to establish the validity of the analytical predictions on the ability of each transducer type to generate pure mode excitation of the A0 and A1 modes, experimental measurements on a steel plate were performed. In the medium frequency-thickness regime, group velocity measurements were sufficient to identify the propagating mode(s) while for the high frequency-thickness regime, as with the analytical predictions, 2-D FFT was employed on the surface time traces recorded via a line scan.

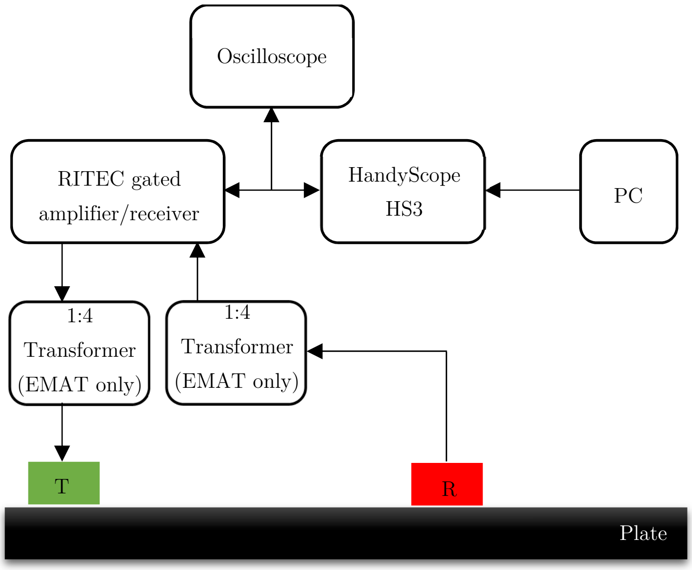

Figure 4.7: *Schematic diagram of the experimental setup.*

4.4.2 Experimental setup

Figure 4.7 illustrates the configuration of the experimental setup used on a 10 mm thick steel plate. The excitation toneburst was generated via a HandyScope HS3 connected to a computer, the signal being amplified using a RITEC RPR4000 gated amplifier (Ritec Inc. Warwick, RI). In the case of EMAT measurements, transformers were used both for excitation and reception in order to match the relatively low impedance of the EMAT to the relatively high impedance of the amplifier. The output signal from the receiver was then amplified and recorded on a digital oscilloscope.

All the measurements presented here were obtained in pitch-catch configuration. Also in order to ensure sufficient resolution in the 2-D FFT, a line scan was carried out over a 200 mm distance with 0.5 mm step intervals.

4.4.3 Pure A0 mode excitation

Wedge excitation of the lower order Lamb modes has been extensively covered in the literature (Ditri et al., 1993; Li and Rose, 2001; Rose, 2002, 2014; Wilcox et al., 2002) so only the EMAT transduction was validated experimentally.

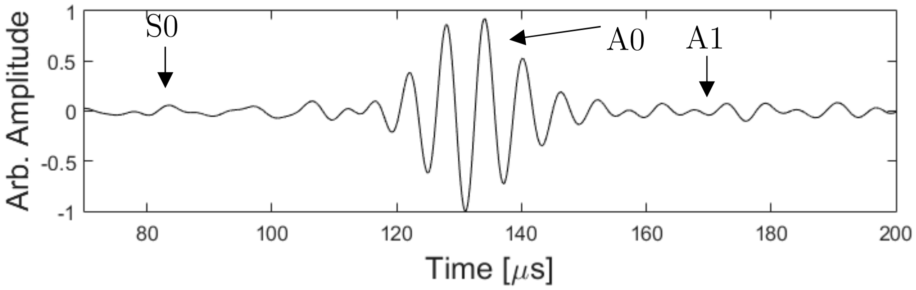

Figure 4.8: *Time-trace obtained in pitch-catch configuration on a 10 mm thick steel plate using two similar 2-cycle meander coil EMATs with a 17 mm wavelength in space over a propagation distance of around 400 mm; the excitation was a 5-cycle Hanning windowed toneburst at 150 kHz centre frequency.*

As in the predictions, the EMAT excitation was performed at 150 kHz centre frequency via a 5-cycle Hanning windowed toneburst which was then amplified and fed into a 2-cycle out-of-plane meander coil EMAT with a 17mm wavelength in space; a similar EMAT was used for reception. To ensure acceptable signal-to-noise ratio (SNR), the EMATs were electrically shielded and 1000 averages were also performed.

Figure 4.8 shows the normalized time trace obtained in pitch-catch configuration over a propagation distance of around 400 mm. Here the group velocity of the wave packet was obtained through time-of-flight measurements where the peak of the wave packet was obtained from a Hilbert transform of the time trace (assuming dispersion is negligible in this case as no obvious peak can be obtained from the Hilbert transform if otherwise). The wave packet shown in Figure 4.8 had a group velocity of 3250 m/s, which is within 1% of the group velocity of the A0 mode obtained from the DISPERSE software (Pavlakovic et al., 1997). The arrival times of the S0 and A1 modes are also displayed on Figure 4.8; here the amplitude ratios of A0/S0 and A0/A1 are around 30:1 and 18:1 respectively.

4.4.4 Pure A1 mode excitation

This section investigates the ability of each transducer type to produce single mode excitation of the A1 mode at 18 MHz-mm. Due to the possibility of multiple modes and their similar dispersion characteristics, a 2-D FFT was employed for modal decomposition purposes.

Figure 4.9a shows a pair of 25.4 mm (1 inch) diameter 2.25 MHz centre frequency piezoelectric compression wave transducers (Panametrics A104S-RB) on gel coupled 60° PMMA wedges on a 10 mm thick steel plate, the excitation being a 5 cycle, 1.8 MHz centre frequency Hanning windowed toneburst.

Figure 4.9b shows the 30-cycle flexible printed circuit board (PCB) meander coil with a 1.8 mm wavelength in space used for the EMAT where the excitation was again performed at 1.8 MHz centre frequency but in this case using a 50-cycle Hanning windowed toneburst. Again, the EMATs were electrically shielded and 1000 averages were used for each measurement.

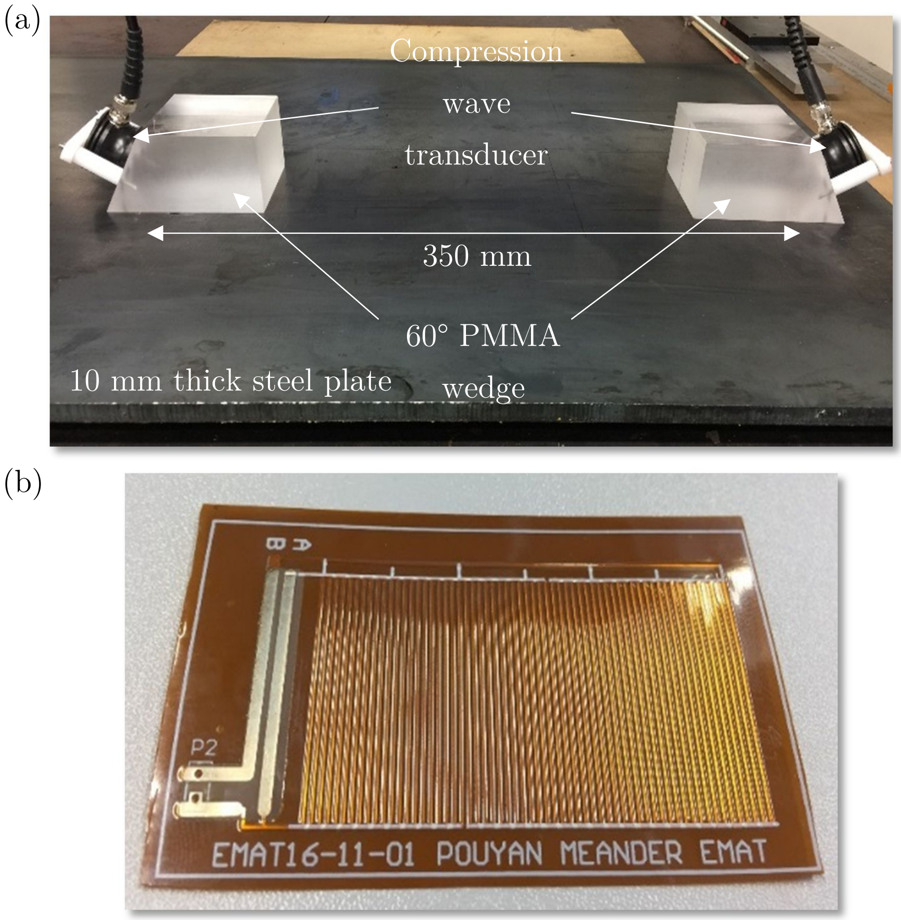

Figure 4.9: *Picture of the (a) 25.4 mm (1 inch) diameter compression wave piezoelectric transducer mounted on a 60° PMMA wedge probes on a 10 mm steel plate; (b) 30-cycle flexible printed circuit board (PCB) meander coil with a 1.8 mm wavelength in space.*

Figure 4.10a shows the time trace obtained using angled wedge excitation in pitch-catch configuration over a 350 mm propagation distance; here the presence of a dominant mode is clearly evident. Figure 4.10b shows the corresponding time trace for the out-of-plane meander coil EMAT where again the presence of a dominant mode is apparent; in this case the signal duration is much higher because of the use of a 50 cycle excitation signal. For both dominant wave packets displayed in Figures 4.10a and 4.10b, the group velocity was found to be within 1.5% of the A1 mode group velocity obtained from the DISPERSE software (Pavlakovic et al., 1997). It is noteworthy that the relatively short propagation distance (dictated by the experimental setup), at which the Figure 4.10a and 4.10b time traces were obtained, is not sufficient for complete mode separation as the A1 and S1 modes exhibit similar dispersion characteristics, therefore the figures (4.10a and 4.10b) do not indicate the true displacement amplitude ratios.

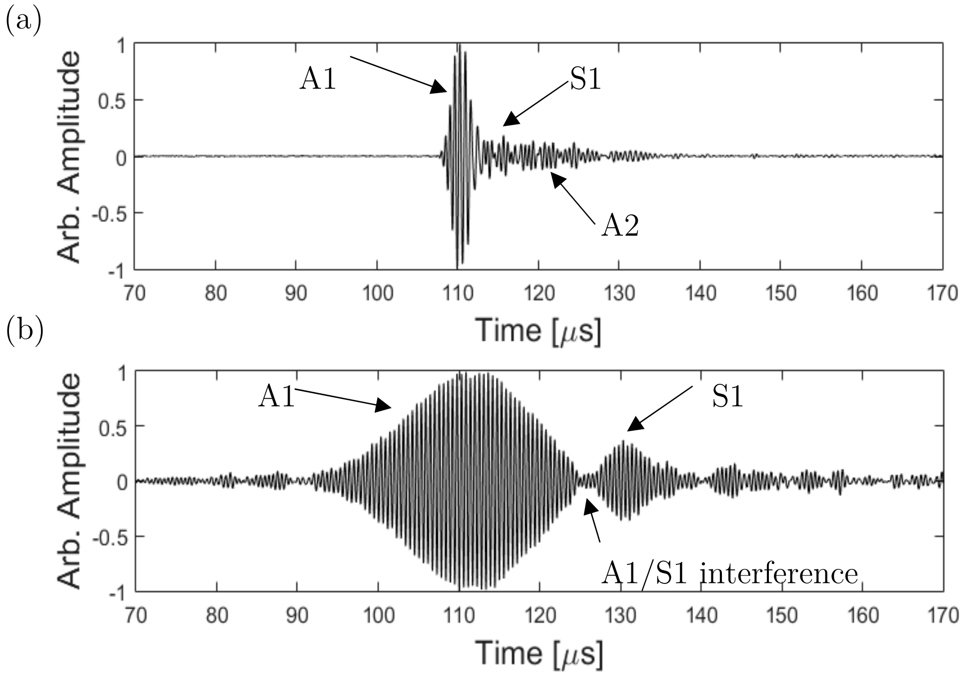

Figure 4.10: *Time-traces obtained in pitch-catch configuration on a 10 mm steel plate with around 350 mm probe separation using (a) two similar probes consisting of a 25.4 mm (1 inch) diameter compression wave piezoelectric transducer mounted on a gel coupled 60° PMMA wedge where the excitation was performed with a 5-cycle Hanning windowed toneburst at 1.8 MHz centre frequency; (b) two similar 30-cycle meander coil EMATs with a 1.8mm wavelength in space where the excitation was performed with a 50-cycle Hanning windowed toneburst at 1.8 MHz centre frequency.*

To further confirm the presence of a dominant A1 mode, a 2-D FFT was performed on the time traces obtained from a 200mm line scan; the EMAT was very difficult to scan accurately at the small intervals necessary for the 2D-FFT, due to its particular design involving the use of strong magnets, so for both excitation transducer types, the time traces were recorded via a 25.4 mm (1 inch) diameter compression wave piezoelectric transducer mounted on a gel coupled 60° PMMA wedge which was moved at intervals of 0.5 mm in the direction of propagation; here a fine adjustment screw was used to push the probe along guiding tracks and to accurately measure the movement of the probe, a digital Vernier calliper was employed.

Figure 4.11a shows the amplitude in the frequency-wavenumber spectrum for the piezoelectric probe, where, as also predicted analytically, A1 is the dominant mode. Figure 4.11b shows the amplitude as a function of wavenumber at the centre frequency (1.8 MHz) obtained from the 2-D FFT of Figure 4.11a; here the presence of the A1 mode is clearly evident and its amplitude is 2.5 and 10 times higher than that of the S1 and A2 modes respectively.

Figure 4.12a shows the linear scale amplitude in the frequency-wavenumber spectrum for the meander coil EMAT transducer where, again, A1 is the dominant mode. Figure 4.12b shows the amplitude as a function of wavenumber at the centre frequency (1.8 MHz) obtained from the 2-D FFT of Figure 4.12a; this shows that the A1 mode is dominant but the precise EMAT-EMAT amplitude ratios cannot be determined because of the use of a wedge receiver rather than the EMAT-EMAT system that was used in the result of Figure 4.10b.

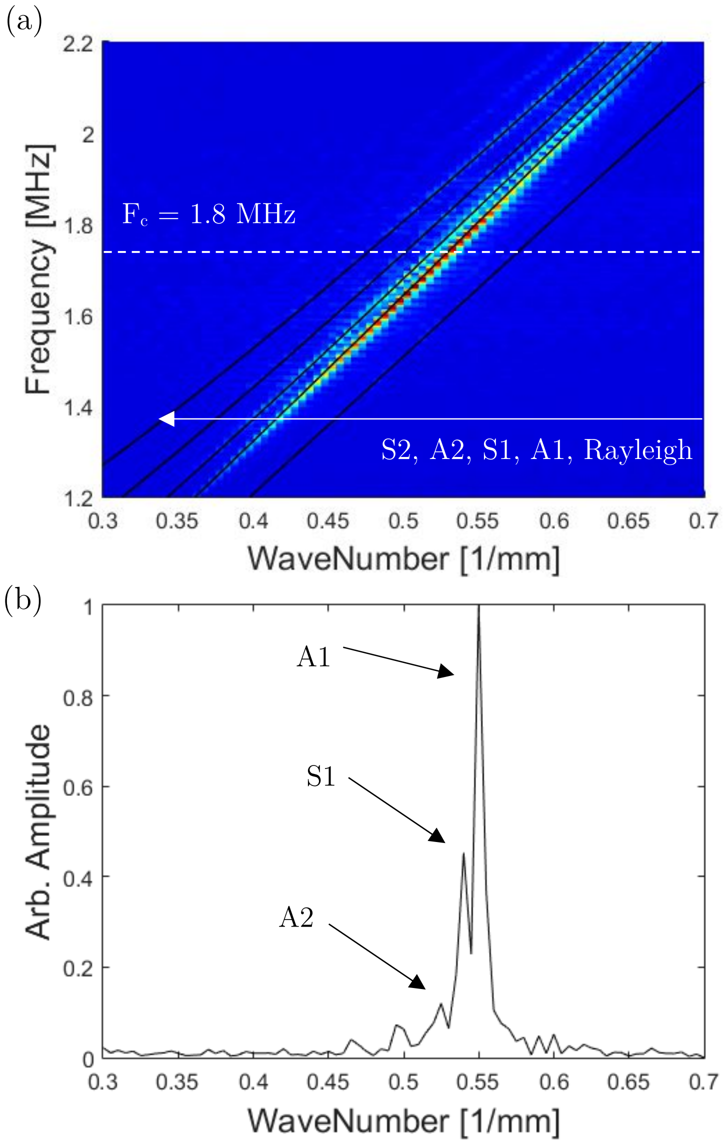

Figure 4.11: *(a) 2-D FFT colour plot [blue (low)–red (high) linear scale] of experimental signal recorded from surface line scan using a 25.4 mm (1 inch) diameter compression wave piezoelectric transducer mounted on a gel coupled 60° PMMA wedge for a 50-cycle 1.8 MHz centre frequency Hanning windowed toneburst excitation signal generated via a similar piezoelectric probe; (b) amplitude as a function of wavenumber at centre frequency (1.8 MHz) obtained from (a).*

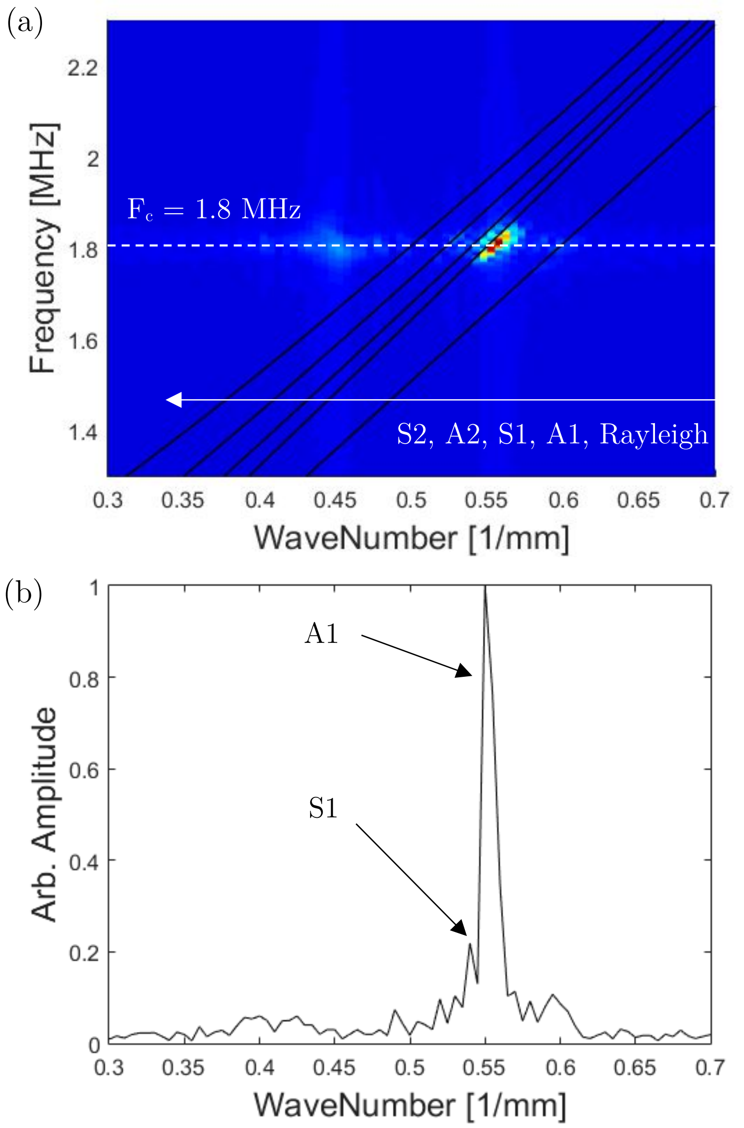

Figure 4.12: *(a) 2-D FFT colour plot [blue (low)–red (high) linear scale] of experimental signal recorded from surface line scan using a 25.4 mm (1 inch) diameter compression wave piezoelectric transducer mounted on a gel coupled 60° PMMA wedge for a 50-cycle 1.8 MHz centre frequency Hanning windowed toneburst excitation signal generated via a 30-cycle meander coil EMAT; (b) amplitude as a function of wavenumber at centre frequency (1.8 MHz) obtained from (a).*

4.5 Conclusions

The relative ability of the angled piezoelectric and meander coil EMAT probes to give pure mode excitation in the medium and high frequency-thickness Lamb mode regimes has been investigated. Analytical predictions of the excitation force amplitude were obtained by simulating the surface forces associated with each transducer followed by the use of a 2-D FFT to highlight the excitation region in wavenumber-frequency space. It was found that with angled wedge excitation there is a linear relationship between the excitation frequency and the wavenumber which means the excitation tends to track typical dispersion curves, allowing for easier pure mode generation. In contrast, the EMAT controls frequency and wavenumber separately which makes it more difficult to generate a pure mode when dispersion curves are close together.

Firstly the excitation of the A0 mode at 1.5 MHz-mm with each transducer type was considered; here it was found that either of the transducer types operate well due to the wide separation of the dispersion curves. It was shown that good selectivity for the A0 mode can be achieved with a simple 2-cycle meander coil EMAT.

Excitation of the A1 mode at 18 MHz-mm was also studied analytically for each transducer type. In the case of wedge excitation, it was shown that given the small wavelengths at higher frequencies, a typical piezoelectric probe is many wavelengths in diameter, allowing for the excitation to be centred on a narrow wavenumber bandwidth which improves the possibility of pure mode transduction even at a high modal density region of the dispersion curves. As mentioned, due to the nature of the meander coil EMAT, it is more difficult to generate a pure mode at high modal density region of the dispersion curves; however, acceptable selectivity could be achieved by narrowing the frequency bandwidth through increasing the number of cycles in the excitation signal. Given the high frequency, this could be achieved while still maintaining a pulse length below ~30 μs; this would give adequate spatial resolution in applications where the aim is to inspect over a range of several metres.

Experimental measurements were carried out on a 10 mm thick steel plate to validate the analytical predictions. The measurements showed good agreement with the predicted results, establishing the possibility of pure mode generation at medium and high frequency-thickness products with both angled piezoelectric and EMAT probes.

Chapter 5

Performance Comparison for Inspection at Inaccessible Locations

There are a number of guided wave and related techniques implemented for corrosion inspection over a limited range from the transducer (up to ~5m) that are attractive for inspection of inaccessible areas such as pipe supports (Burch, 2016; Swaminathan et al., 2011) and the annular ring of storage tanks (Chandrasekaran et al., 2009). This chapter presents a systematic analysis of the defect detection performance of each method with sharp and gradual defects, as well as their sensitivity to attenuative coatings, liquid loading, surface roughness and ability to test beyond features such as T-joints.

The chapter starts by providing a background on the setup and industrial applications of each inspection technique mentioned above; then using analytical and numerical means, the effect of various commonly found surface features, when testing at inaccessible locations (such as T-joints and rough surfaces), on each technique is investigated. Next the characteristics of each method for the detection of sharp and gradual defects are studied numerically and experimentally. Finally, by summarising the key findings, the chapter goes on to provide recommendations on the appropriate method(s) in different inspection circumstances. This work is in print at the NDT&E Int. 2018 [P2] and the chapter follows the structure of the paper.

5.1 Introduction

Corrosion under pipe supports (CUPS) is problematic for guided wave inspection as at the low frequencies required to detect gradual wall thinning, the support itself gives a significant reflection (Carandente et al., 2010; Carandente and Cawley, 2012; Galvagni and Cawley, 2011), and the locations of concern are inaccessible for conventional ultrasonic thickness gauging. Similar issues arise when testing the floor of storage tanks from the small region of the floor protruding outside the tank wall. Also, deep defects with relatively small plan area are sometimes a concern as shown in Figure 5.1a (Burch, 2016). Figure 5.1b shows a typical pipe support involving pipework resting on a secondary structure. Corrosion and pitting are known to develop at the contact area between the support and the pipe which compromise the integrity of the structure; hence, establishing a reliable method for inspecting such regions is crucial.

There has been a number of guided wave and related techniques proposed to address these issues:

- S0 mode Lamb wave at ~ 1.5 MHz-mm (Bloom et al., 2009; Corrosion Inspection Technologies, 2016; ROSEN, 2016)
- SH0 and SH1 modes at ~ 3 MHz-mm (Innerspec, 2016; Sonomatic, 2016a)
- Creeping Head-wave Inspection Method (CHIME) ~ 20 MHz-mm (Ravenscroft et al., 1998; Sonomatic, 2016b)
- Multi-skip (M-skip) ~ 20 MHz-mm (Burch et al., 2007; Lorenz and Lewandowski, 2012; Sonomatic, 2016c)

- Higher order mode cluster (HOMC) ~ 18 MHz-mm (Balasubramaniam et al., 2012; Chandrasekaran et al., 2009; Satyarnarayan et al., 2008; Swaminathan et al., 2011)

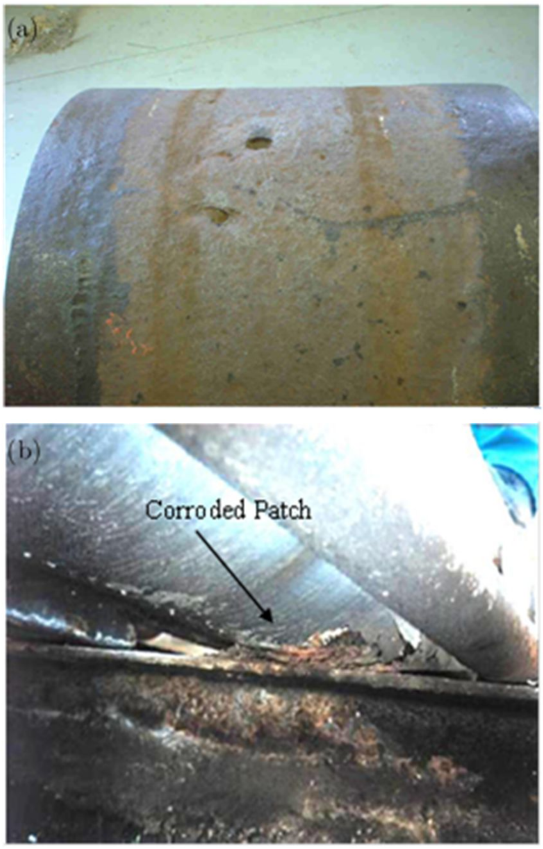

Figure 5.1: *Photographs of (a) deep, highly localised pits (Burch, 2016); (b) simple pipe support (Lorenz and Lewandowski, 2012).*

The operating points of the guided wave methods are shown on the dispersion curves for Lamb (Figure 5.2a) and SH (Figure 5.2b) waves. It is not clear from previous work which of these methods is the most appropriate in different circumstances. This chapter undertakes a systematic analysis of their defect detection performance with sharp and gradual defects, and their sensitivity to attenuative coatings, liquid loading, surface roughness and ability to test beyond features such as T-joints. Most of the results are obtained analytically or with finite element simulations, key points being validated experimentally. Section 5.2 gives a brief description of each of the methods and the previous work done on them and section 5.3 then introduces the finite element analysis used to produce most of the results. Section 5.4 then studies the influence of different coatings, surface conditions etc. in turn on each of the inspection techniques, followed by an analysis of the sensitivity of the methods to different types of defect. The results with the most promising methods are validated experimentally in section 5.5 and the findings are summarised in Section 5.6, together with recommendations on the most appropriate method(s) in different circumstances.

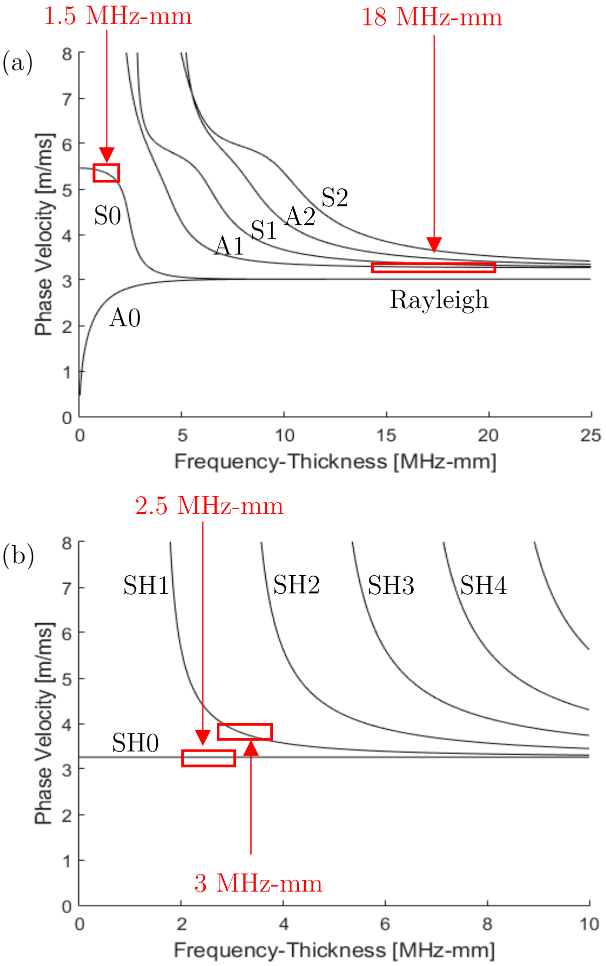

Figure 5.2: *Phase velocity dispersion curves of guided waves in steel plate a) Lamb modes b) shear horizontal (SH) modes; generated using DISPERSE (Pavlakovic et al., 1997) software.*

5.2 Background to the Inspection Methods

The S0 mode Lamb wave at around 1 MHz-mm exhibits desirable properties such as being fairly non-dispersive at low frequencies and also for having a simple mode shape which provides roughly constant sensitivity to defects at different depths. Generic applications of the S0 mode for detecting various types of defect in pulse-echo and pitch-catch setups have been studied extensively (Alleyne and Cawley, 1992b; Lowe and Diligent, 2002); however, the use of the method in more specific circumstances such as detection of CUPS is less well covered in the literature. Commercial users of this method include the Rosen Group (ROSEN, 2016) who employ electromagnetic acoustic transducers (EMATs) to inspect pipelines with limited accessibility e.g. at pipe supports; here various guided wave modes including S0 can be generated for optimal feature detection and in the case of pitting, for example, a 30% cross-sectional loss is reported to be the detection threshold for a probability of detection (POD) of 80%. Also Corrosion Inspection Technologies (Corrosion Inspection Technologies, 2016) use group velocity measurements of the S0 mode in transmission for CUPS monitoring in a guided wave tomography configuration and claim a smallest detectable depth of 10% (Bloom et al., 2009).

Shear horizontal (SH) guided waves at around 3 MHz-mm provide an alternative inspection method since they are unaffected by non-viscous liquid loading of the structure and in the case of the fundamental SH mode (SH0), non-dispersive inspection can be carried out. Similarly to the S0 mode, general application of SH waves for detecting different types of defect has been studied in depth (Belanger, 2014; Hirao and Ogi, 1999; Ma and Cawley, 2010; Nurmalia et al., 2011, 2012), but the use of these waves for more specific applications such as corrosion detection in inaccessible regions is less well described. There is a number of commercial users of SH waves such as Sonomatic (Sonomatic, 2016a) who employ EMATs for thinner walled pipes (<15 mm) to excite both the SH0 and SH1 modes. The SH0 mode is non-dispersive so its arrival time can be used to determine the ratio of distance travelled to the shear wave velocity; all the higher order modes have a lower group velocity than SH0 and their arrival times are used to estimate the average remnant thickness between the probes. Sonomatic claim that localised corrosion at 20% depth is detectable (Sonomatic, 2016a); however, this is greatly influenced by factors such as the surface condition, coating type/thickness and defect morphology. Another example is Innerspec (Innerspec, 2016) who employ EMATs in an automatic inspection system to scan for defects in the axial and circumferential directions; a transmission configuration is used for the circumferential scan which can use the excitation transducer to receive waves that have travelled around the pipe circumference, while reflection in a pulse-echo configuration is measured for axial scans. It is reported (Innerspec, 2016) that the system is able to detect corrosion damage with 20% and 30% wall loss in the axial and circumferential directions respectively.

One of the more specialised methods of corrosion testing with up to 1 m range is the Creeping Head-wave Inspection Method (CHIME) which uses a conventional setup of a piezoelectric transducer mounted on a wedge at the critical angle to produce surface creeping, head and bulk waves (Duffill and Silk, 2000; Ravenscroft et al., 1998). In order to satisfy the surface boundary conditions, creeping waves must continuously produce head-waves which reflect multiple times from the plate/pipe surfaces and on each reflection the head wave partially mode converts back to a creeping wave (Erhard and Kröning, 1984; Ravenscroft et al., 1998). The received signal therefore consists of a series of peaks made of the original creeping wave followed by the second creeping wave which is generated by mode conversion of the head wave which has done one full skip and so on; this allows complete volume inspection of the waveguide as the presence of a defect or a thickness change alters the arrival time and/or amplitude of these peaks (Ravenscroft et al., 1998). If, however, the structure boundaries are not parallel, the head wave to creeping wave mode conversion cannot occur which limits the application of this method to pipes whose outer/inner diameter ratio is less than 1.19 (Ravenscroft et al., 1998). The separation of the bulk waves and the creeping/head waves is also strongly dependent on the thickness of the structure which is the reason why CHIME is usually employed on structures thicker than 12mm (Ravenscroft et al., 1998). Ravenscroft et al. (Ravenscroft et al., 1998) applied this method to test for machined notches, isolated pits and general corrosion on a pipe and reported that a corrosion patch of 50mm width and minimum wall loss of 23% is detectable. Sonomatic (Sonomatic, 2016b) use CHIME to inspect inaccessible regions such as pipe supports and claim that the method is able to qualitatively rank the depth of corrosion into categories of <10%, 10% to 40% and >40% corrosion.

Other methods of corrosion inspection with up to 2 m range include multi-skip (M-skip) which uses piezoelectric transducers mounted on wedges with an angle larger than the first critical angle in a pitch-catch configuration to produce shear vertical waves that reflect multiple times between the structure boundaries without mode conversion (Burch et al., 2007). This therefore allows the inspection of the complete volume between the transmitting and receiving probes as the arrival time of each skip depends on the separation distance of the probes and the thickness of the material; since the shear wave cannot mode convert to longitudinal waves, the signal losses are minimised, hence enabling larger probe separation (Burch et al., 2007). However, the presence of a secondary feature on the surface of the plate/pipe, such as an attenuative coating, causes energy leakage when the shear wave is reflected from the corresponding surface which is why, to avoid a large number of surface skips, M-skip is mostly applied to structures thicker than 12mm

(Burch et al., 2007). Also the reflection of the shear wave from a boundary is strongly dependent on the surface condition which as a result limits the application of this method to test structures with uneven boundaries (Lorenz and Lewandowski, 2012). Burch et al. (Burch et al., 2007) studied the performance of M-skip on pitting type defects and provided a comparison between CHIME and M-skip for naturally corroded pipe support testing. They concluded that while M-skip is able to estimate the average wall loss between the probes, the maximum depth of an area of varying wall loss cannot be indicated. Shell (Lorenz and Lewandowski, 2012) used the M-skip method for clamped saddle support inspection and suggested that the method is more suited to detect local wall loss, while CHIME can be used to identify the degree of general thinning. Other commercial users of M-skip include Sonomatic (Sonomatic, 2016c) who employ the method to test for corrosion in inaccessible areas such as pipe supports and, by using B-scans, they are able to estimate the depth of localised flaws while in the case of general degradation, the average remaining wall thickness can be approximated.

Finally, the use of HOMC (Balasubramaniam et al., 2012; Chandrasekaran et al., 2009, 2010; Jayaraman et al., 2009; Ratnam et al., 2012; Satyarnarayan et al., 2008; Swaminathan et al., 2011) was considered, the fundamental characteristics/properties of which were discussed in the previous chapters. We also have shown that the features of HOMC are essentially those of the A1 mode in this frequency-thickness regime (Khalili and Cawley, 2016).

The methods introduced in this section are assessed against different criteria in Section 5.4.

5.3 Finite Element Analysis

In order to assess the performance of each method against a number of different criteria, Finite Element (FE) analysis was used. In general a two-dimensional (2D) model of a plate was used to simulate the propagation of the excited wave and for the cases of the guided wave methods, a Fourier transform in space and time (2D FFT) (Alleyne and Cawley, 1991; Khalili and Cawley, 2016) was employed to measure the parameters of interest such as attenuation, reflection and transmission coefficients whereas due to the nature of the bulk wave methods, these parameters were obtained via surface amplitude comparison recorded from the out-of-plane time traces. 2D analysis has been used throughout this chapter because it captures most of the important physics and is much more efficient computationally than full 3D analysis; it should be noted that in order to imitate a 2D model for the SH methods, a single element wide 3D model was created where appropriate boundary conditions were utilised to mimic a plain strain configuration. Use of 2D analysis means that the attenuation values reported do not include the effects of beam spreading that will affect the lower frequency techniques more than the higher ones (for example, when considering a typical reflector, such as a defect, the length/wavelength ratio would be significantly higher for the high frequency techniques due to their smaller wavelengths meaning the beam spread effect is reduced for such techniques compared to the lower frequency ones). Also the effects of diffraction around small defects are not captured and this again will affect the lower frequency methods more severely.

The majority of the FE simulations were performed using the Pogo software package (Huthwaite, 2014b), an FE solver which runs on graphics cards to greatly reduce the required simulation time. Pogo does not currently permit mixing of elastic and acoustic elements so ABAQUS CAE was employed in a 2D plane strain configuration for the liquid loading cases. Figure 5.3 shows the overall FE setup, where a 10 mm thick steel plate was created using CPS4R elements (linear elastic material properties were considered); suitable element sizes and time steps were applied according to the frequency regime of each method to maintain stability and accuracy (Ludwig and Lord, 1988). The excitation setup was also tailored for each method; in the case of the S0 mode, the mode shape was excited along the cross-section of the plate to ensure minimal intrusion of the other modes, the excitation signal being a 150 kHz centre frequency, 5-cycle Hanning-windowed toneburst. A similar mode shape excitation technique was also used for the SH0 and SH1 mode methods at a higher centre frequency of 250 kHz and 300 kHz respectively. For the CHIME method, the excitation simulated a 1-inch transducer on a fluid coupled 27° PMMA wedge; this was achieved by phased out-of-plane point forces on the top surface of the plate and the excitation signal in time was at 2.25 MHz centre frequency, 5-cycle Hanning-windowed toneburst. Although, as mentioned above, CHIME is best suited for structures thicker than 12 mm (Ravenscroft et al., 1998), the simulations presented here were on a 10 mm plate for consistency with the other methods. M-Skip was simulated using the same setup as for CHIME with a wedge angle of 45°; the A1 mode method (similar to HOMC) was simulated in a similar way but with a 60° wedge angle, while the excitation signal in time was a 1.8 MHz, 5-cycle Hanning-windowed toneburst.

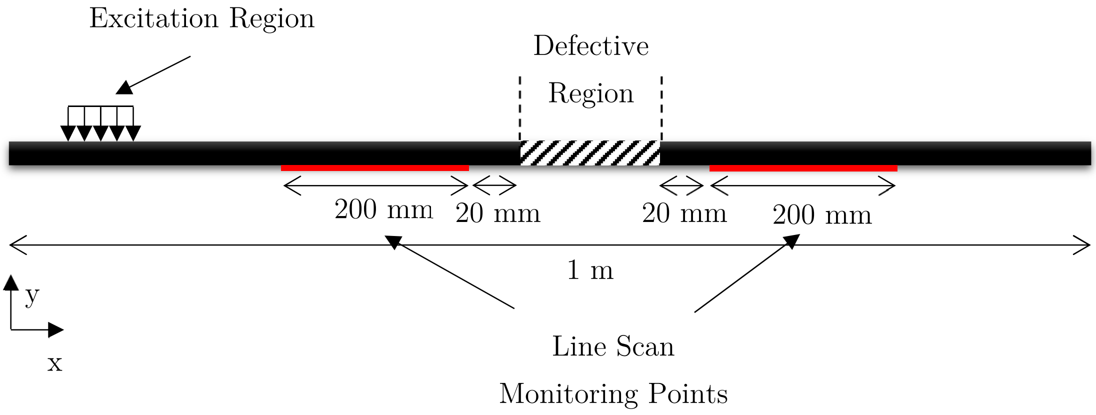

Figure 5.3: *Schematic of the general 2D FE setup.*

As shown in Figure 5.3, 200 mm line scans were utilised on each side of the defective region to enable 2D FFT analysis; the amplitude obtained from the modal decomposition was used to determine the reflection and transmission coefficients for a given mode compared to an undamaged/free plate. For the liquid loading and surface coating cases the transmission coefficient determines the attenuation level.

Figure 5.3 also shows the monitoring points being placed on the opposite surface of the plate relative to the excitation; this was done specifically for the A1 mode method to eliminate the presence of the Rayleigh wave which tends to dominate the response due to its high excitability. This does not affect the absolute amplitude of the modes of interest since they are equal on either surface. In practice, where the excitation is carried out using a fluid coupled wedge, the Rayleigh wave is damped by leakage into the wedge and is not seen in the received signals. This was verified in FE by analysing one case in which the excitation was applied to a wedge, rather than by simply applying surface tractions to the plate.

5.4 Results

5.4.1 Effect of liquids

In most cases of guided wave and bulk wave testing, the structure is assumed to be within a vacuum. This is a reasonable approximation if the surrounding medium has an acoustic impedance very different to that of the structure material such as a pipe in air and/or carrying a gas. However when dealing with liquid interaction, the impedance contrast is much smaller and the energy leakage of the propagating sound wave into the surrounding liquid cannot be neglected as before. In this section the attenuation of each method is predicted in a liquid loaded structure to establish their suitability in such conditions.

In this chapter water loading is considered; while liquids such as oil may result in different attenuation levels, the difference is expected to be minimal compared with the overall effects of liquid loading (Huthwaite et al., 2013). Attenuation levels of the guided wave methods were predicted analytically using the DISPERSE (Pavlakovic et al., 1997) software, while an FE model was developed in ABAQUS CAE to predict the energy leakage of the bulk wave methods (CHIME and M-skip) into the surrounding liquid. In both the analytical and numerical studies, a 10 mm steel plate was created and the vacuum boundary on one side of the plate was substituted with a half-space of water. In FE, the water boundary was generated using AC2D4R elements which are acoustic elements that do not support shear waves; these elements were appropriately tied to the surface of the plate and to mimic a semi-infinite space of water, Absorbing Layers using Increasing Damping (ALID) (Rajagopal et al., 2012) elements were placed adjacent to the acoustic element layer to absorb the leaked energy and prevent it from re-entering the plate structure.

Table 5.1 shows the attenuation levels of each method at their respective centre frequencies. As expected the SH wave methods experience no energy leakage since the surrounding water layer cannot support shear waves. The A1 mode method exhibits relatively low attenuation compared with other Lamb wave methods such as the S0 mode; this is due to the low surface motion of the A1 mode at high frequency-thickness products as established previously (Khalili and Cawley, 2016). The bulk wave methods performed particularly poorly as they rely on multiple boundary reflections for propagation, hence the condition of the surface and/or the presence of surface loading result in energy loss and scattering of the waves. The attenuation of CHIME was higher than that of M-skip since this method entails creeping waves propagating along the both surfaces of the plate that makes this method more susceptible to the presence of surface features.

Table 5.1: *Predicted attenuation of each method in 10 mm thick steel plate due to presence of half-space water; predictions obtained using DISPERSE (Pavlakovic et al., 1997) except where stated.*

Wave	Centre Frequency	Attenuation (dB/m)
S0	150 kHz	3.4
SH0	250 kHz	0
SH1	300 kHz	0
A1	1.8 MHz	2.3
CHIME	2.25 MHz	32.2 (FE)
M-Skip	2.25 MHz	26 (FE)

5.4.2 Effect of coatings

In order to minimise corrosion, coatings are often used on pipe surfaces. Some of the materials used, such as bitumen, are highly attenuative and can cause significant damping of the propagating wave, so reducing the length of pipe that can be inspected from a given transducer position. In general this damping effect depends on the type of coating material and its thickness; however, since the coatings are sometimes applied manually there can also be variations in the coating thickness and the bonding between the surface and the coating (Huthwaite et al., 2013).

In this study, bitumen coating was considered on one side of the plate-like structure in order to compare its damping effect for each method. Table 5.2 shows the bitumen material properties that were used in the analysis.

Table 5.2: *Properties of bitumen used in this study* (Simonetti, 2004a).

Density (kg/m^3)	970
Longitudinal Velocity (m/s)	2200
Shear Velocity (m/s)	700
Longitudinal Attenuation (Np/λ)	0.05
Shear Attenuation (Np/λ)	0.50

As with liquid loading, the attenuation levels of the guided wave methods were predicted analytically using the DISPERSE (Pavlakovic et al., 1997) software and the energy loss of the bulk wave methods were predicted using an FE model created in Pogo (Huthwaite, 2014b). In both models, a 2mm bitumen coating was placed on one side of a 10 mm steel plate.

Table 5.3: *Predicted attenuation of each method in 10 mm thick steel plate due to presence of 2mm bitumen coating; predictions obtained using DISPERSE (Pavlakovic et al., 1997) except where stated.*

Wave	Centre Frequency	Attenuation (dB/m)
S0	150 kHz	2.6
SH0	250 kHz	19.2
SH1	300 kHz	27.6
A1	1.8 MHz	1.8
CHIME	2.25 MHz	33.6 (FE)
M-Skip	2.25 MHz	16.6 (FE)

Table 5.3 shows the attenuation levels of each method at their respective centre frequencies. Unlike the liquid loading case, the SH wave methods experience much higher attenuation since the coating can support shear waves and exhibits relatively high shear attenuation; this energy loss is particularly high for the SH1 method due to the operating frequency being near a through-thickness resonance frequency of the bitumen layer (260kHz) (Simonetti, 2004b). However, even at frequencies away from resonance, this mode experiences minimum attenuation of around 12 dB/m. The S0 method performs better as the coating provides lower longitudinal attenuation compared to the shear attenuation and the A1 method was the least affected by the coating as it exhibits very low surface motion that limits the energy leakage into the coating layer; as with liquid loading, the bulk wave methods show high attenuation.

5.4.3 Effect of rough surfaces

One of the often overlooked factors in ultrasonic inspection is rough surfaces due to general corrosion. It has been shown (Bass and Fuks, 1979; Chimenti and Lobkis, 1997; Dobson and Cawley, 2017; Ogilvy, 1987, 2000) that general corrosion of pipework can cause significant scattering of incident waves, resulting in higher background noise and also increased energy loss of the wave, limiting its inspection range. The signal to noise ratio is therefore decreased and the sensitivity of the method is reduced. Since it is often of interest to detect deep corrosion patches in the presence of modest generalised corrosion, the influence of shallow, general corrosion on the different methods is an important issue in selecting between them.

In this study, the effect of a 400 mm long section of rough surface on a 10 mm thick steel plate was investigated; the model was 2D so the surface simulated was a series of parallel troughs running normal to the plane of the elements. It is noteworthy that while the response of each method to a 3D rough surface would be different, the 2D model was considered to be viable for this study as the aim was to compare the performance of each method as they were subjected to the same boundary conditions. Figure 5.4a shows the remnant thickness map of the rough surface; the profile was generated via a Gaussian distribution based on the parameters associated with a 30 year old generally corroded pipe sample that was obtained from industry in a previous investigation (normal distribution with a mean wall loss of 1.25 mm, standard deviation of 0.75 mm (Dobson and Cawley, 2017)). The surface grid was convolved with a Gaussian window that had a characteristic length equal to the correlation length of the surface roughness (Dobson and Cawley, 2017; Ogilvy, 2000). The correlation length, shown in Figure 5.4b, is measured as the distance from the peak to the point at which the amplitude distribution drops to 1/e of the maximum. Figure 5.4c illustrates the depth distribution of the simulated rough surface; the slight distortion of this distribution is because the depths less than zero were set to zero as the rough surface due to corrosion was modelled as thickness loss only. Further details of the generation of the surface are given in (Dobson and Cawley, 2017).

Table 5.4 shows the reflection and transmission coefficients for each method at their respective centre frequencies when interacting with the 400 mm rough surface described in Figure 5.4a. All the guided wave methods show high transmission and low reflection coefficients; the SH1 mode at 300 kHz in the 10mm thick plate is dispersive and so is very sensitive to thickness with high mode conversion explaining the low transmission coefficient compared to the SH0 mode. The bulk wave methods show minimal transmission past the rough surface as they require near-parallel boundaries to propagate. While some signal was transmitted, clear wave packets were not identifiable.

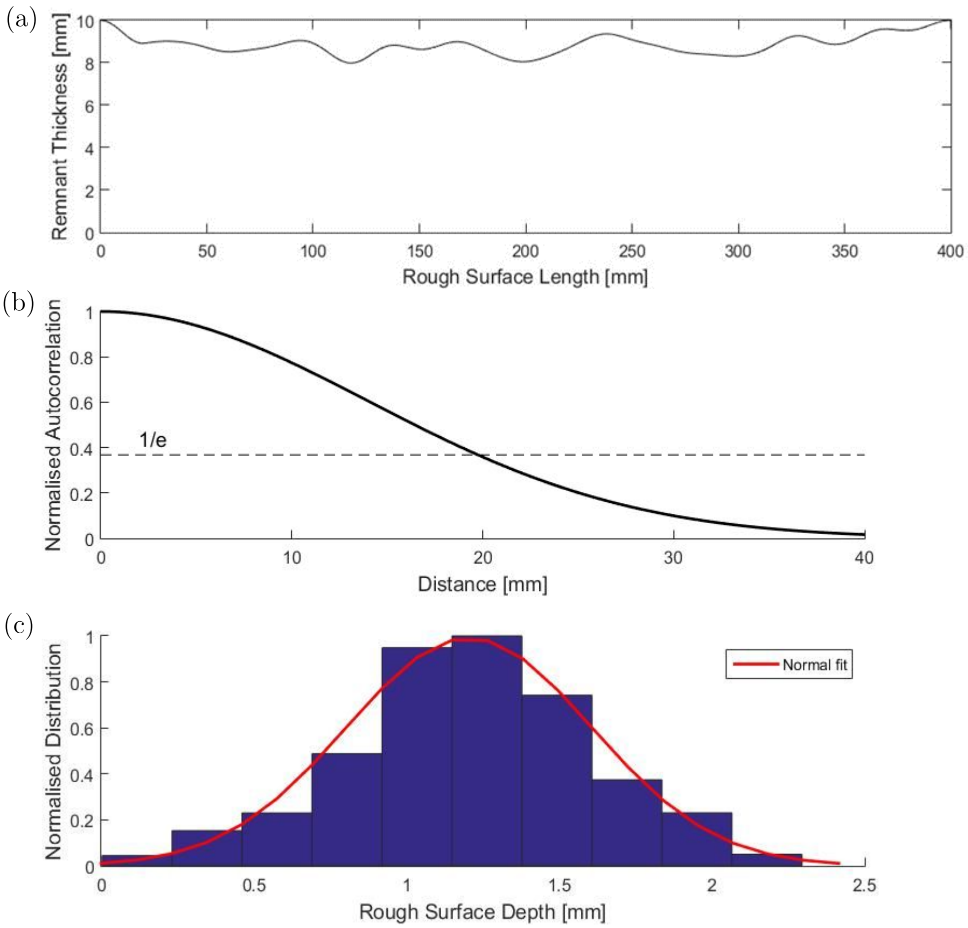

Figure 5.4: *Simulated rough surface using the moving average method showing a) the surface morphology; b) the autocorrelation length of the surface in the x-direction; c) the distribution of depths. Surface shown has a mean depth of 1.25 mm and a correlation length of 20 mm.*

Other cases of rough surfaces with different correlation lengths and mean depths were investigated to check whether the results of Table 5.4 are generally representative of likely corrosion profiles. Similar results were found, though it was found that the reflection coefficient of the A1 mode was increased by any random outliers present in the profile with depths over 20% of the wall thickness; this would be expected from the mode shape (Khalili and Cawley, 2016) and is seen in the defect reflection results of section 5.4.5 below. The SH1 mode showed high sensitivity to the specific profile of the rough surface since it exhibits high motion close to the surface which in turn also makes it sensitive to shallow defects.

Table 5.4: *Predicted reflection and transmission coefficients of each method obtained using 2D FFT in 10mm thick steel plate with the 400 mm rough surface described in Figure 5.4.*

Wave	**Centre Frequency**	**Reflection Coefficient**	**Transmission Coefficient**
S0	150 kHz	0.01	0.98
SH0	250 kHz	< 0.01	0.96
SH1	300 kHz	0.01	0.83
A1	1.8 MHz	0.01	0.88
CHIME	2.25 MHz	-	-
M-Skip	2.25 MHz	-	-

5.4.4 Inspection of T-joints

It is often necessary to inspect for corrosion beyond a feature in the structure. For example, pipes are sometimes welded to supports at the two support ends and it is necessary to detect corrosion in the middle of the supported region. Likewise it is desirable to detect corrosion in an oil storage tank by propagating waves along the floor plate from outside the tank; in this case it is necessary to test beyond the location where the tank wall is welded to the floor plate. These generic cases were investigated by studying propagation past a T-joint comprising a horizontal 10mm thick steel plate rigidly attached to a similar plate in the vertical direction as shown in Figure 5.5. A 2D FFT was used to predict the reflection and transmission coefficients of the guided wave methods while for the bulk wave methods, amplitude ratios of reflected and transmitted waves to the incident wave were used.

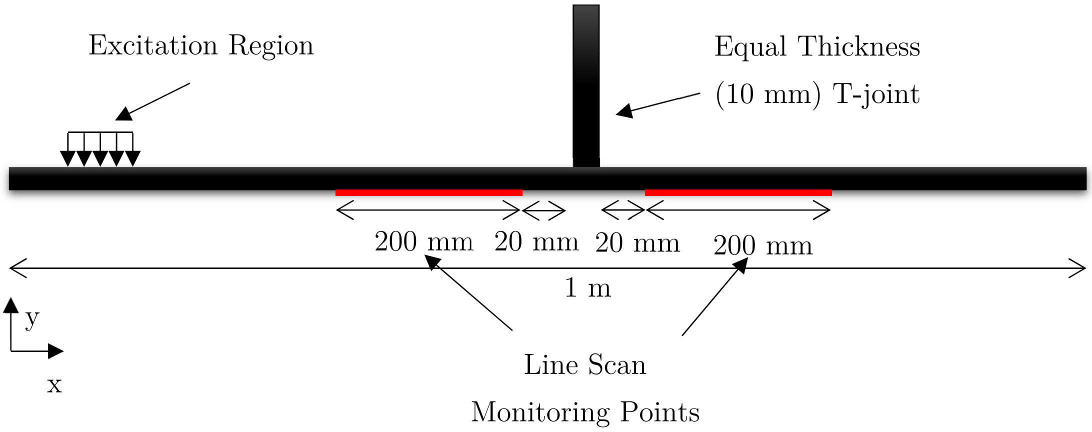

Figure 5.5: *Schematic of the 2D FE setup for T-joint.*

Table 5.5: *Reflection and transmission coefficients for each method through equal thickness (10 mm) T-joint interaction.*

Wave	**Centre Frequency**	**Reflection Coefficient**	**Transmission Coefficient**
S0	150 kHz	0.1	0.82
SH0	250 kHz	0.1	0.89
SH1	300 kHz	0.21	0.81
A1	1.8 MHz	0	0.95
CHIME	2.25 MHz	0	-
M-Skip	2.25 MHz	0	0.75

Table 5.5 shows the reflection and transmission coefficients for each method at their respective centre frequencies when interacting with the T-joint described in Figure 5.5. Apart from the A1 mode, the guided wave methods experience noticeable energy loss when propagating past the T-joint; the A1 mode at 18 MHz-mm exhibits minimal surface motion which allows negligible reflection from the T-joint and also reduces energy leakage to the structure. CHIME showed poor transmission past the T-joint as the surface creeping wave was scattered significantly by the feature so clear wave packets were not detectable. In the case of the M-skip, the performance was found to be very setup sensitive; parameters such as the separation distance between the excitation region and the T-joint and also the angle of excitation, determine the level of interaction of the propagating shear waves with the T-joint.

The results presented here are for a single geometry of T-joint. While the many other possible geometries will give somewhat different results, the key finding that the A1 mode is essentially unaffected will remain since its lack of sensitivity to additions at the surface is a result of its very low surface motion.

5.4.5 Inspection of sharp defects

The more common types of damage to the pipe include wide area gradual thickness loss and sharp pitting type defects. In this section, testing for sharp defects is considered. Interaction of generic, low frequency guided waves with localised sharp defects has been studied extensively (Alleyne et al., 1998, 2001; Cawley et al., 2003; Demma et al., 2004, 2003; Lowe et al., 2002; Mudge and Catton, 2008; Rose et al., 2004) but in order to improve sensitivity to such discontinuities it is of interest to raise the frequency; however, testing in the frequency-thickness region where multiple modes can exist is less well understood. This section studies the performance of the guided wave methods when interacting with sharp defects; the bulk wave methods were not considered in this case because of the poor performance of CHIME on the criteria above and also the performance of M-skip, as explained before, is very setup sensitive and therefore difficult to quantify.

Firstly the sensitivity of each method to the depth of defect was investigated by predicting the reflection and transmission coefficients when interacting with crack depths of 1% to 50%; these were modelled by disconnecting nodes in the FE mesh. Then the performance of each method was studied when the length of defect was introduced; here the rectangular notches were modelled by removing elements in the mesh and to understand the physics of each method, the length of the notch was changed as a function of their wavelength where the reflection and transmission coefficients were obtained using a 2D FFT. It should be noted that the wavelengths of the methods are very different, hence the absolute length of notch in figures 5.7 and 5.8 is different where wavelengths range between 2 mm for the A1 mode to 35 mm for the S0 mode.

Figure 5.6a shows the reflection coefficients of the S0, SH0, SH1 and A1 modes against the crack depth. Here it is clear that the cracks under 10% deep are difficult to detect through reflection while the A1 mode, in particular, cannot detect defects with 20% or lower thickness loss due to its mode shape that exhibits low surface motion at 18 MHz-mm. The S0 and SH0 modes allow a more linear response to the crack depth since their mode shape displacements are relatively constant across the thickness of the structure.

Figure 5.6b illustrates the corresponding transmission coefficients where the drop in transmission coefficient was due to a combination of energy loss through reflection and mode conversion in transmission.

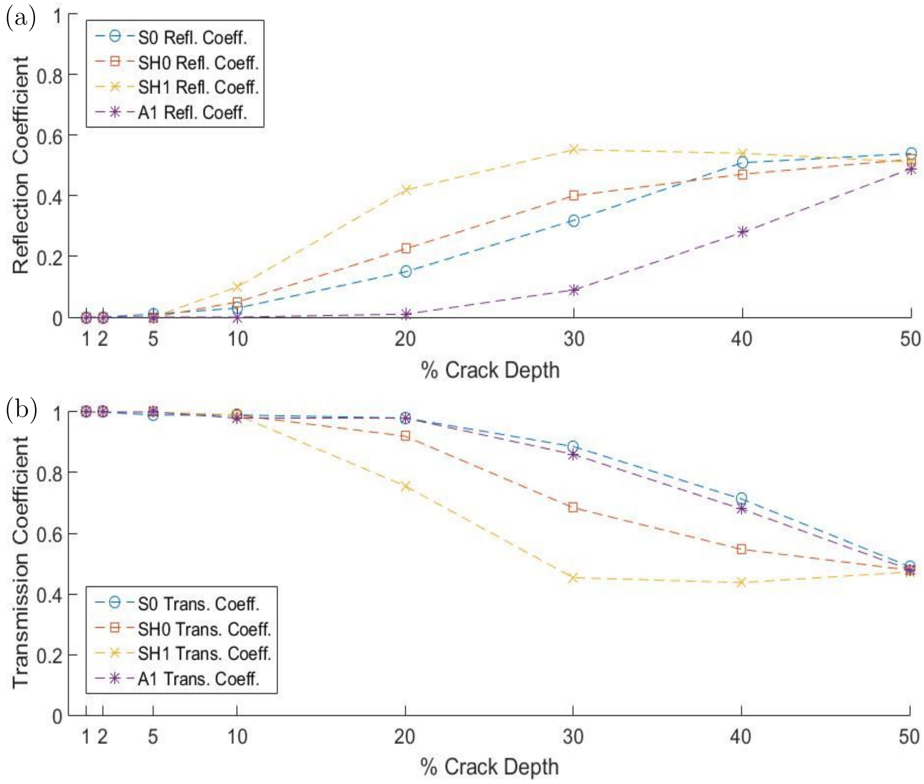

Figure 5.6: *2D FE predictions of reflection (a) and transmission (b) coefficients of the guided wave methods at crack depths of 1% to 50% in 10mm thick plate. The results are for the following methods at their corresponding centre frequencies (fc): S0 at fc=150 kHz (Blue), SH0 at fc=250 kHz (Red), SH1 at fc=300 kHz (Yellow), A1 at fc=1.8 MHz (Purple). (Points joined with straight lines to aid clarity)*

As suggested by Figure 5.6a and 5.6b, the reflection and transmission coefficients of all the guided wave methods tend to a similar value of about 50% for the 50% crack depth; this is likely to be due to the symmetric energy distribution of the guided wave modes about the thickness centre line of the waveguide which leads to the similar reflection and transmission coefficients.

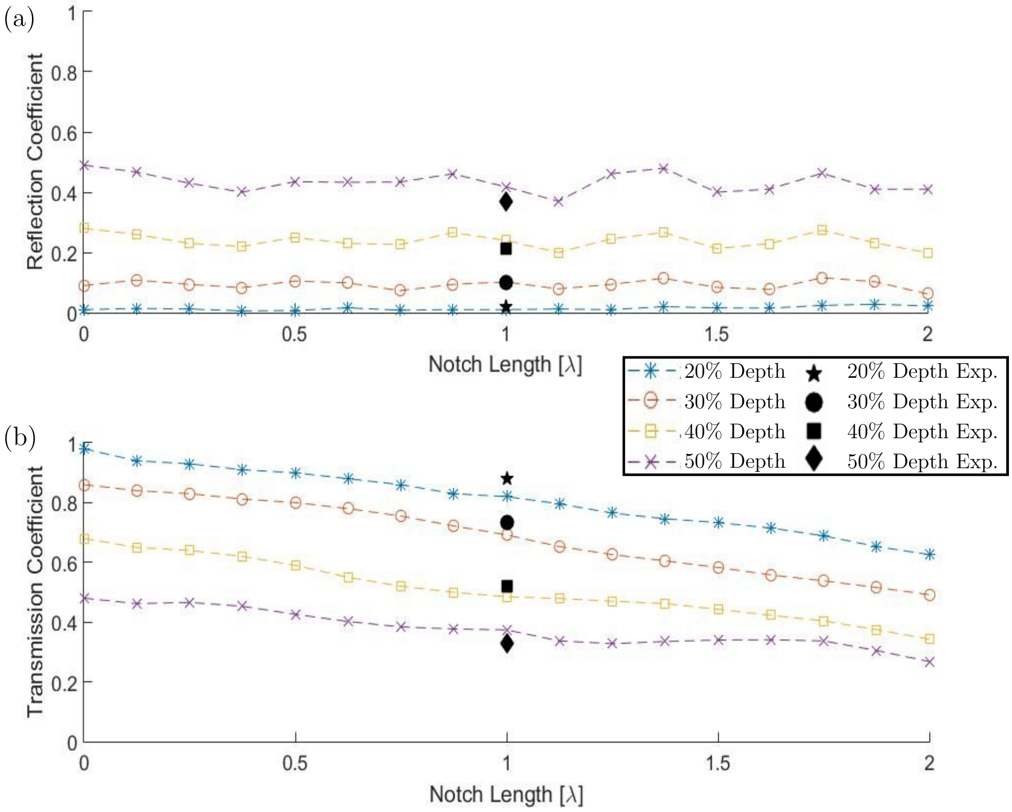

Figure 5.7: *2D FE predictions of reflection (a) and transmission (b) coefficients of the A1 mode at different depths (20% to 50%) and lengths (0 to 2λ) of notches (Points joined with straight lines to aid clarity). The reflection and transmission amplitudes obtained from experimental results in Figure 5.12 are also included.*

Figure 5.7a shows the reflection coefficient of the A1 mode against the notch length for depths of 20% to 50%. As expected, the reflection coefficient was predicted to increase for deeper notches and it is also evident that for a given depth of notch its value remains relatively constant with the notch length meaning the detectability of the notch is independent of its lateral dimension. This behaviour is due to the significant mode conversion to higher order modes which minimises the interference effect as a result of reverberations within the notch area. This contrasts with the behaviour seen when the SH0 mode at low frequency interacts with rectangular notches. Here a sinusoidal variation in reflection coefficient is observed with a maximum when the notch length is a quarter wavelength and minimum at half wavelength; this is due to the constructive and destructive interference of reverberations of the SH0 mode in the notch length (Demma et al., 2003). In the SH0 case at low frequency it is the only propagating mode so no mode conversion occurs; with the A1 mode at high frequency, extensive mode conversion can occur so there is no clear periodicity of reverberations.

Figure 5.7b illustrates the transmission coefficient of the A1 mode against the notch length for depths of 20% to 50%; here it is clear that the transmission coefficient reduces for longer notches. Through further investigation, it was found that when the incident A1 mode interacts with the step-down part of the notch, it partially mode converts to the Rayleigh mode which propagates along the base of the notch, so the transmitted A1 mode past the step-up part of the notch is formed by a combination of the remnant A1 mode and the mode conversion of the Rayleigh mode back to the A1 mode. As the notch becomes longer, the group velocity mismatch between the Rayleigh and A1 modes causes an interference effect which results in the reduction of the transmission coefficient recorded in this study.

Figure 5.8a shows the reflection coefficient of the S0, SH0 and SH1 modes against the notch length at a fixed 30% depth. Here it is clear that the reflection coefficient of these modes varies significantly with the notch length because of the interference effect created through reverberations in the notch (Demma et al., 2003); this can limit the detectability of the methods as the reflection coefficient is highly dependent on the lateral length of the notch meaning that at some lateral lengths, minimal reflection is obtained even from very deep defects. In this comparison, the reflection coefficient of the SH1 mode is generally larger than that of the other modes and comparable even at worst as this mode at 300 kHz in the 10 mm thick plate is highly dispersive and so is very sensitive to the thickness of the structure;

this higher thickness sensitivity however causes stronger interference effects resulting in larger variation of the reflection coefficient with notch length.

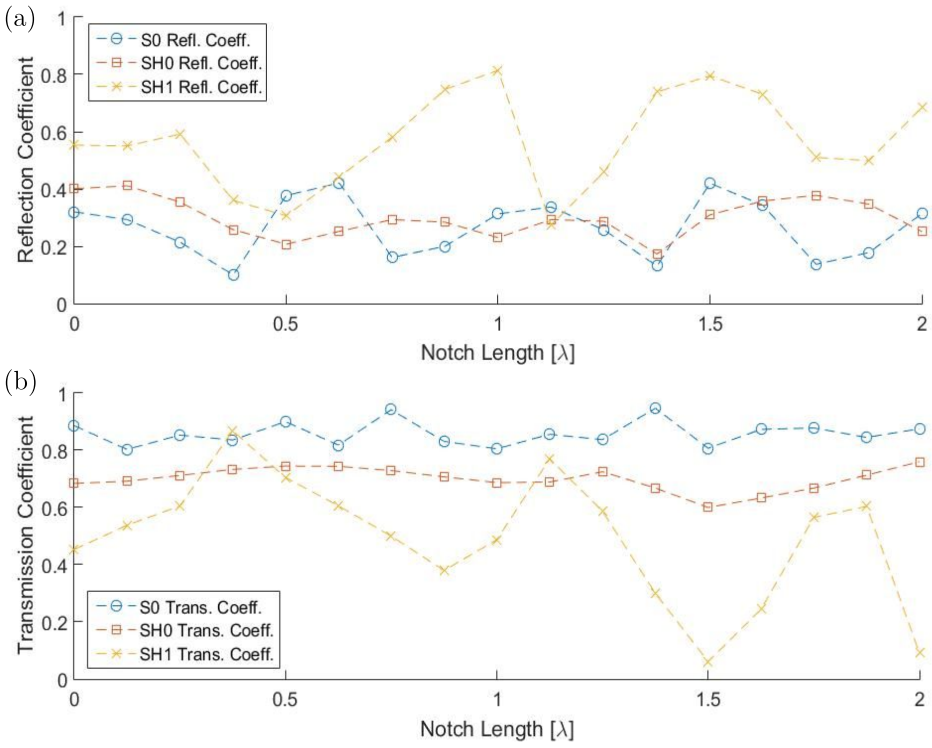

Figure 5.8: *2D FE predictions of reflection (a) and transmission (b) coefficients of the other guided wave methods at a fixed notch depth of 30% and lengths (0 to 2λ) of notches in 10mm thick plate. The results are for the following methods at their corresponding centre frequencies (fc): S0 at fc=150 kHz (Blue), SH0 at fc=250 kHz (Red), SH1 at fc=300 kHz (Yellow). (Points joined with straight lines to aid clarity)*

Figure 5.8b shows the corresponding transmission coefficients; here the S0 mode exhibits the highest transmission coefficient even compared with the SH0 mode since there is higher dissimilarity between the mode shapes of the S0 and A0 modes than there is between the SH0 and SH1 modes which results in lower mode conversion and therefore higher transmission coefficient.

5.4.6 Inspection of gradual thinning

As mentioned above, corrosion patches sometimes involve wide area, gradual thickness loss which can significantly affect the performance of an inspection technique (Carandente et al., 2010; Carandente and Cawley, 2012). In this section, the interaction of each method with a large gradual defect is considered.

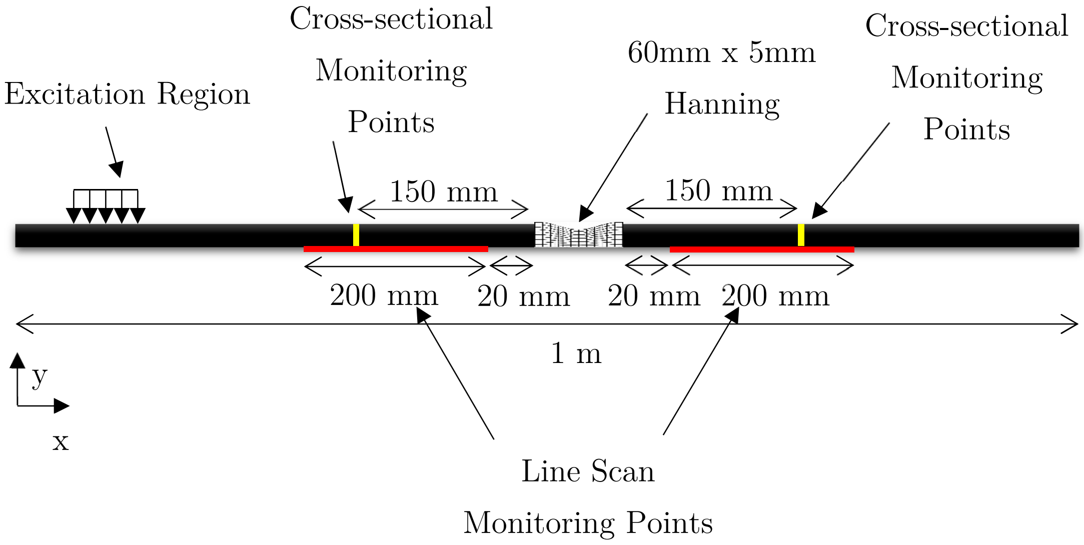

Figure 5.9: *Schematic of the 2D FE setup for gradual thickness loss.*

The defect was modelled as a 60 mm x 5 mm Hanning shaped notch in FE, shown in Figure 5.9, and to study its effect on each method, the reflected and transmitted time traces were obtained with a setup similar to the excitation setup of the corresponding method; for instance, in the case of the A1 mode the reception with a 1-inch transducer on a fluid coupled 60° PMMA wedge (as used for excitation) was simulated by phased addition of out-of-plane surface displacements. Mode shape excitation was used for the S0, SH0 and SH1 modes, reception being done by summing the displacements across the cross-section weighted according to the corresponding mode shape.

Table 5.6: *Reflection and transmission coefficients for each method through a 60mm x 5mm Hanning shaped notch.*

Wave	**Centre Frequency**	**Reflection Coefficient**	**Transmission Coefficient**
S0	150 kHz	0.04	0.99
SH0	250 kHz	0.01	0.98
SH1	300 kHz	0.94	0.14
A1	1.8 MHz	0	0.99
M-Skip	2.25 MHz	-	0.2

Table 5.6 shows the reflection and transmission coefficients for the S0, SH0, SH1, A1 and M-skip methods. Here it is clear that all the guided wave approaches, apart from the SH1 mode, experience minimal reflection from the large Hanning-shaped notch because the notch length (60 mm) is significantly larger than even the largest wavelength (32 mm for the S0 mode) (Carandente et al., 2010); this behaviour is due to the reflection coefficient being highly dependent on the wavelength of the propagating mode and in the case of the fundamental torsional mode T(0,1) in pipes or SH0 in plates, the reflection was predicted to be minimal for Hanning-shaped notches which are over 1.5λ long (Carandente et al., 2010). In transmission, due to the change in the remnant thickness of the structure, the guided wave methods all experienced mode conversion. The SH1 mode shows a significant reflection from the gradual defect as the remnant thickness is 50% at its lowest which is below the cut-off frequency-thickness product of this mode, resulting in the large reflection and reduced transmission recorded in this study. As explained before, the performance of the M-skip method is dependent on a number of factors; in this case, no reflection was recorded and the scattering of the

angled shear waves from the gradual notch contained various guided wave modes and surface waves, so a very complex signal was obtained in transmission.

5.5 Experimental Validation

In order to verify the FE predictions presented above, experimental measurements on a steel plate were carried out. For this section, the A1 and SH1 modes were chosen to establish their performance when testing for sharp notches at various depths as well as for wide-area gradual thinning by obtaining pulse-echo and pitch-catch time traces. The A1 mode was selected as it showed the best overall performance on the criteria above while its higher operating frequency improves the sensitivity to sharp, localised defects; in the case of the SH1 mode, it was considered to provide better detectability to shallower defects because of its dispersive nature while showing good performance on a number of criteria discussed above. It is noteworthy ,however, that in practice, it is difficult to excite a pure SH1 mode at 3 MHz-mm, hence the test signal consists of both SH0 and SH1 modes.

5.5.1 Experimental setup

Figure 5.10a illustrates the experimental setup for the SH modes when testing for 2-D 2 mm long sharp defects at depths of 10% to 50% of the plate thickness which were machined on a 10mm thick steel plate and Figure 5.10b shows the setup for the A1 mode used to test a 2-D 60 mm x 5 mm Hanning-shaped notch. Excitation for the A1 mode was performed at 1.8 MHz centre frequency with a 5-cycle Hanning-windowed toneburst via a 1-inch diameter 2.25 MHz centre frequency piezoelectric compression wave transducer (Panametrics A104S-RB) mounted on a gel coupled 60° PMMA wedge [c_L = 2710 m/s, and ρ = 1188 kg/m^3 (Khalili and

Cawley, 2016)]; the excitation for the SH modes was carried out at 300 kHz centre frequency with a 5-cycle Hanning-windowed toneburst via single-loop SH wave EMATs (Howard and Cegla, 2017) where the reflection was recorded via a separate EMAT placed around 250 mm after the excitation EMAT (as shown in Figure 5.10a).

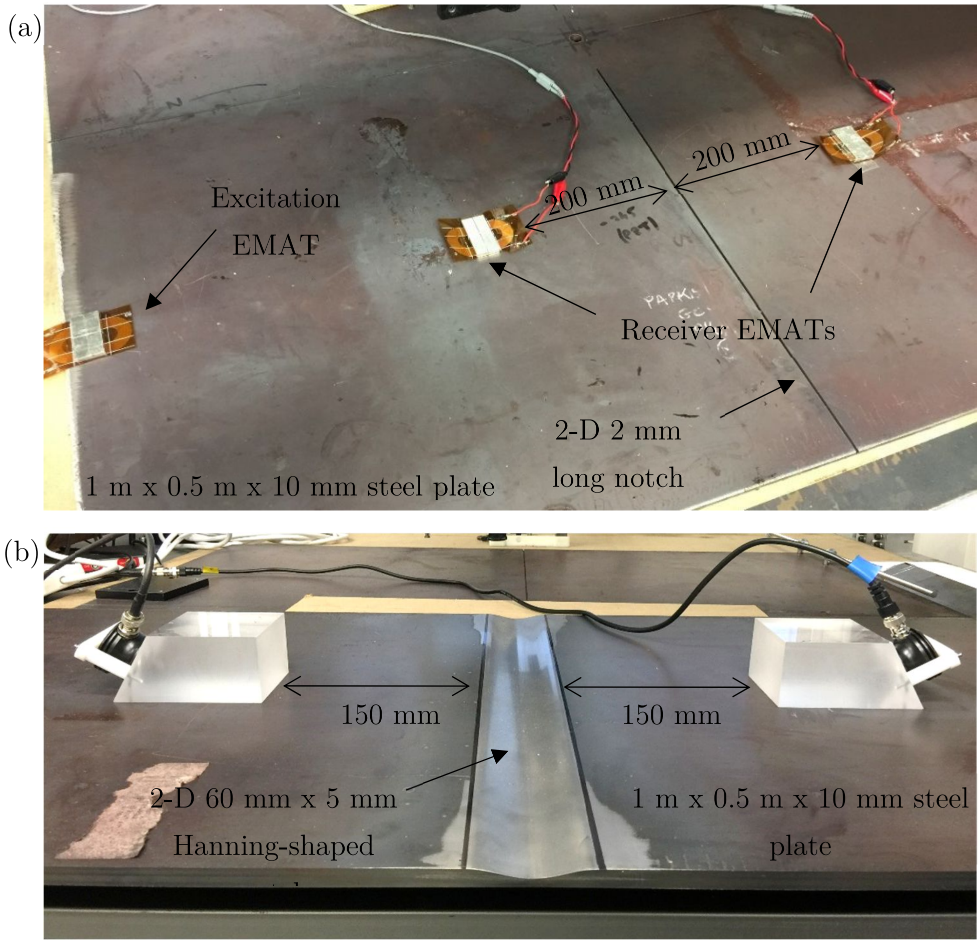

Figure 5.10: *Experimental setup on 1 m x 0.5 m x 10 mm steel plates consisting of (a) SH wave EMATs placed around 200 mm before and after the 2-D 2mm long rectangular notch defect with a separate excitation EMAT; (b) two sets of compression wave transducers mounted on a gel coupled 60° PMMA wedge, for A1 mode excitation, positioned around 150 mm before and after the 2-D 60 mm x 5 mm Hanning-shaped notch.*

The toneburst was generated and amplified via a custom-built amplifier which was then fed into the transducer. To record the reflections from the defect, in the case of the A1 mode, the excitation transducer was positioned before the defect and used as a receiver in a pulse-echo configuration, while for the SH modes, a separate EMAT was employed after the excitation EMAT to record the reflections. To obtain the transmitted signals a second transducer similar to that for the excitation was placed after the defect and employed in a pitch-catch configuration. The signals received for both methods were amplified and then captured on a digital oscilloscope. In order to improve the SNR, 1000 averages were used when testing with the SH modes due to the lower amplitudes generated by the EMATs, while 10 averages or fewer were required for the A1 mode.

5.5.2 Sharp notch results

The measured A1 mode reflection and transmission coefficients are shown alongside the FE predictions in Figure 5.7 and show good agreement. The amplitudes were normalised to the transmitted wave that was obtained in a separate test on an undamaged section of the plate. As expected the reflection amplitude is shown to increase while the transmission amplitude decreases as the notch becomes deeper. Also as predicted by the FE results, the notches with 20% or lower thickness loss are difficult to detect through reflection due to the low surface motion of the A1 mode at 18 MHz-mm.

Figure 5.11 illustrates the predicted (red) and experimental (black) reflection time traces for the SH modes when interacting with 2 mm long notches with depths of 10% (b), 20% (c), 30% (d), 40% (e) and 50% (f). It should be noted that the time traces were normalised to the incident wave (a) which was obtained separately on an undamaged section of the steel plate; the incident wave consists of both SH0 and SH1 modes since pure SH1 mode excitation is difficult to implement in practice in this frequency-thickness regime due to the proximity of the SH0 and SH1 modes at around 3 MHz-mm as shown in the dispersion curves of Figure 5.2b. Therefore, additional FE simulations have been carried out to validate the experiments directly; these are shown as red coloured time traces in Figure 11b and 11f for the shallowest (10%) and deepest (50%) notch cases respectively. The expected arrival time (at centre frequency) of each mode, generated through mode conversion of the incident modes, is indicated on Figure 5.11c (The SH0-SH1 and SH1-SH0 mode conversions do not appear at exactly the same time because the outward path from the transmitter to the defect is longer than that for the reflected wave from the defect to the receiver, as shown in Figure 5.10a). The main reason for using the SH1 mode is to enhance sensitivity to shallower defects. In the case of the 10% depth notch, it is evident from the predicted and experimental time traces that the reflection signal is only generated from the SH1 part of the incident wave while the SH0 mode is unaffected (this was also confirmed numerically through a separate simulation; for brevity, the results are not shown here). For deeper notches, the reflected signal is complex because of the interference effect as both the SH0 and SH1 modes experience mode conversion; this is evident in both the predicted and experimental time traces.

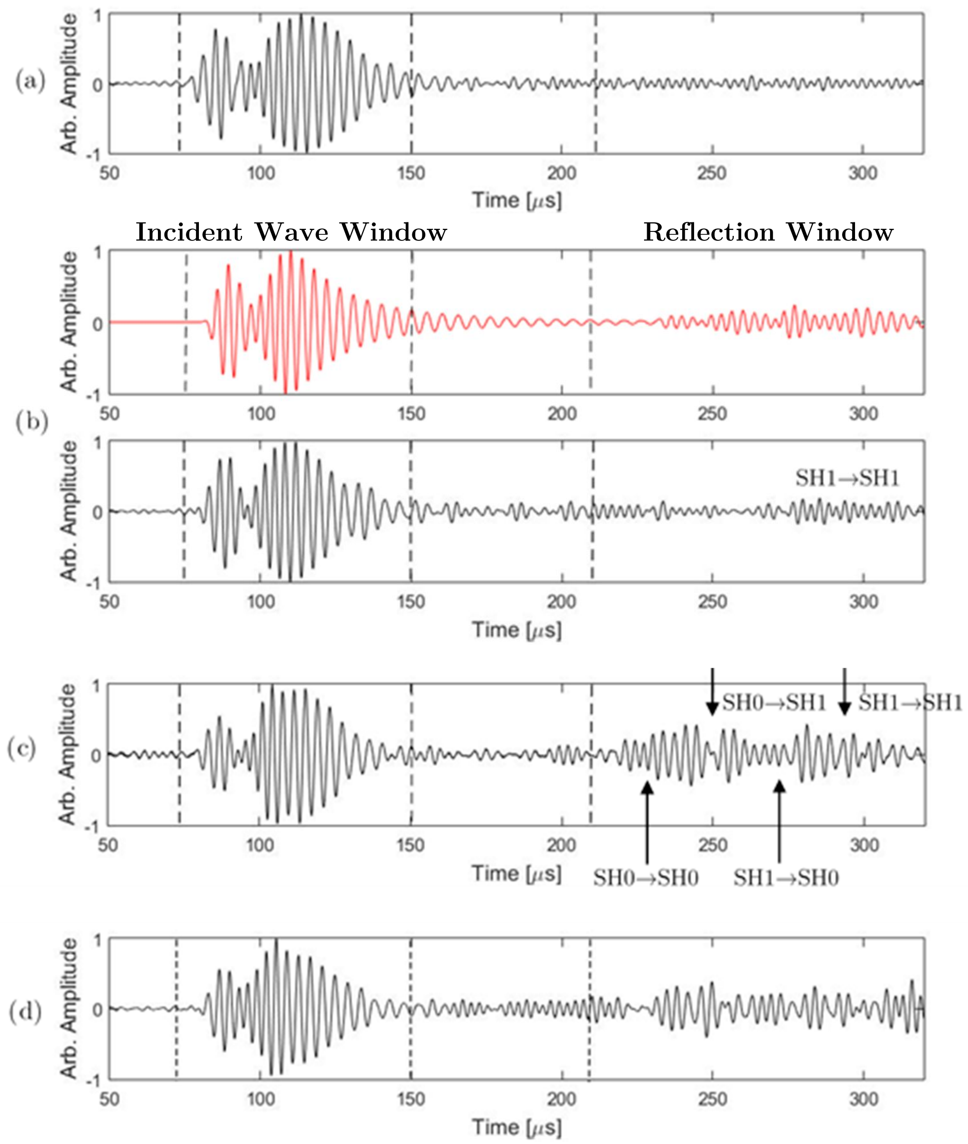
(a)
Arb. Amplitude
1
0
-1
50
100
150
200
250
300
Time [μs]
Incident Wave Window
Reflection Window
(b)
SH1→SH1
(c)
SH0→SH1
SH1→SH1
SH0→SH0
SH1→SH0
(d)

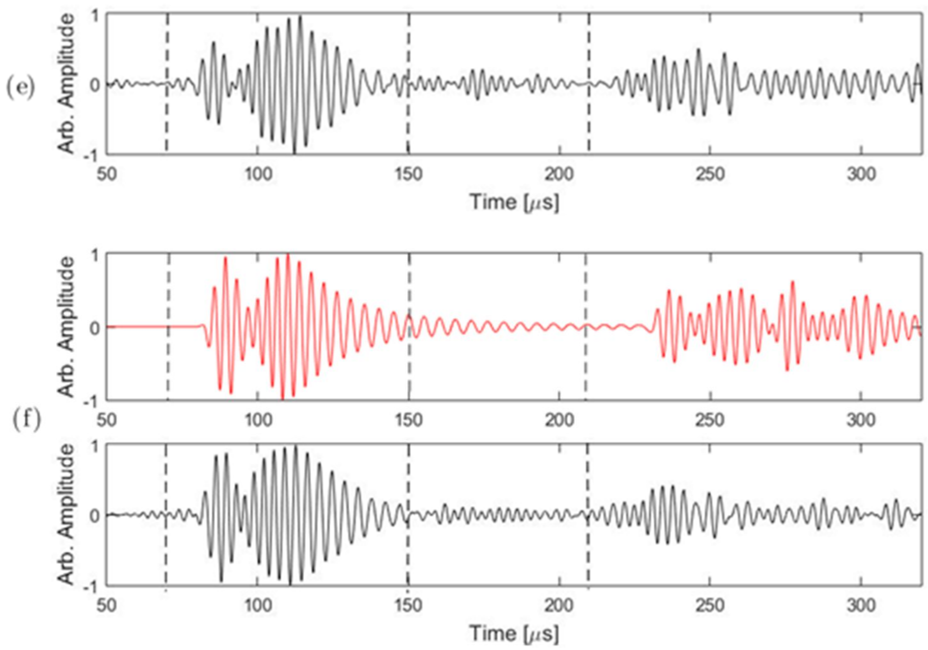

Figure 5.11: *(a) Experimental baseline SH signals at 3 MHz-mm on undamaged section of 10 mm thick steel plate; (b) predicted (red) and experimental (black) signals reflected from sharp notch 10% of plate thickness deep normalised to maximum amplitude in (a); (c) experimental signal as (b) for 20% deep notch; (d) as (c) for 30% deep notch; (e) as (c) for 40% deep notch; (f) as (b) for 50% deep notch.*

5.5.3 Gradual defect results

Figure 5.12a and 5.12b show the normalised reflection and transmission time traces for the A1 mode respectively when interacting with the large Hanning-shaped notch. As predicted by the FE results, this mode experiences minimal reflection from the defect as the length of the notch (60 mm) is significantly larger than the wavelength of the A1 mode (2 mm) at 18 MHz-mm. The transmitted signal of

Figure 5.12b is relatively complex due to mode conversion to the S1 and other modes; this was also predicted by FE analysis.

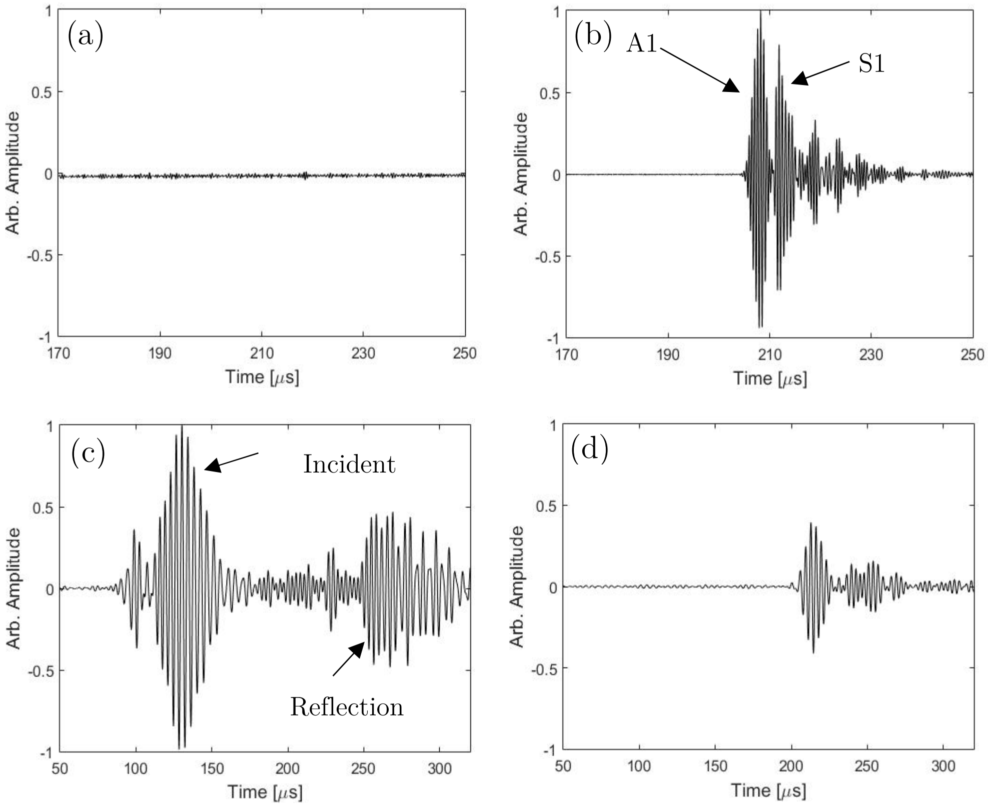

Figure 5.12: *(a) Normalised (to transmitted wave) time trace of the A1 mode (1.8 MHz centre frequency) in pulse-echo configuration around 150 mm behind the 60 mm x 5 mm Hanning-shaped notch in a 10 mm thick steel plate; (b) as (a) in pitch-catch configuration around 150 mm after the defect; (c) as (a) for the SH modes (300 kHz centre frequency); (d) as (b) for the SH modes.*

Figure 5.12c and 5.12d shows the normalised reflection and transmission time traces for the SH modes respectively when interacting with the large Hanning-shaped notch. As suggested previously by the FE results, the SH1 mode experiences a significant reflection from the defect as the minimum remnant thickness of the notch is below its cut-off frequency-thickness product; also due to this cut-off process, the transmitted signal predominantly consists of the SH0 mode.

5.6 Conclusions

The performance of the A1, S0, SH0, SH1, M-skip and CHIME inspection methods for detecting sharp and gradual defects was established via numerical predictions with selective experimental validation. The ability of the methods to cope with features such as liquid loading, surface coatings, rough surfaces and T-joints was also predicted via a mixture of analytical and numerical predictions. Table 5.7 summarizes the performance of the methods along with the long range guided wave method that was not covered in this chapter but has been extensively researched previously (Carandente and Cawley, 2012; Cawley et al., 2003; Demma et al., 2003; Lowe and Diligent, 2002; Mudge and Catton, 2008; Wilcox et al., 2002); desirable performance on each criterion is indicated with **bold text**.

When dealing with surface features such as liquid loading, coatings and welded T-joints, the A1 mode was very little affected due to its low surface motion at 18 MHz-mm and showed the best overall performance. The bulk wave methods (CHIME and M-skip) are predicted to perform poorly as they require multiple surface reflections to propagate so the presence of surface features has a significant effect.

With regards to the sharp defects, as suggested by Table 5.7, the A1 mode offers the best performance for inspecting severe (>30%) thickness loss as it exhibits high spatial resolution because of its raised operating frequency and also, as shown by Figure 5.7a, the detectability of the sharp notches is independent of their axial dimension which is in contrast to the other guided wave methods discussed in Table 5.7. When testing for sharp but shallow defects, the SH1 mode is found to be the most suitable method because of its dispersive nature at around 3 MHz-mm which provides enhanced sensitivity to small thickness changes.

When inspecting for wide-area gradual thinning, low frequency guided waves offer higher detectability in reflection because of their longer wavelengths; detection in reflection can also be achieved with the SH1 mode for the cases when the remnant thickness is near the cut-off frequency-thickness product of this mode as shown in Table 5.7. The SH1 mode was also found to be suitable for detecting wide-area gradual thinning in transmission and it may be possible to obtain remnant thickness profiles of structures along a line (Howard and Cegla, 2017), again because of the dispersive nature of this mode.

In addition to the performance, there are a number of limitations regarding the application of some of the methods which were not investigated in this chapter. The excitation of a pure SH1 mode is not easy due to the presence of the SH0 mode and its relatively large wavelength at 3 MHz-mm. In the case of M-skip, the performance was found to be highly dependent on the number of surface “skips”, hence in order to minimise the effect of surface features and increase the detectability of sharp defects, it was concluded to be more suited for inspecting thicker structures. Finally CHIME is often not practical for corrosion inspection at inaccessible locations as rough surfaces, welded patches and coatings are often present.

Table 5.7: *Performance of the each inspection methods along with the long range guided wave methods (not covered in this chapter) for the different areas investigated in this chapter.*

Inspection method	Long range S0/SH0	S0	SH0	SH1	A1	M-Skip	CHIME
Centre frequency x Nominal thickness (MHz-mm)	*< 0.5*	*1.5*	*2.5*	3	18	22.5	22.5
Effect of liquid loading	**Very low**	Average	**Very low**	**Very low**	**Low**	*Very high*	*Very high*
Effect of surface coatings	**Very low**	**Low**	*Very high*	*Very high*	**Very low**	*Very high*	*Very high*
Effect of rough surfaces	Average	**Low**	**Low**	Average	**Very low**	*Very high*	*Very high*
Effect of T-joint/welded patch	*Very high*	Average	**Low**	Average	**Very low**	Average	*Very high*
Sensitivity to sharp shallow defects	*Very poor*	Average	Average	**Good**	*Very poor*	Case dependent	-
Sensitivity to sharp severe defects	*Poor*	**Good**	**Good**	Average	**Very good**	Case dependent	-
Sensitivity to wide-area gradual thinning in reflection	**Good**	*Poor*	*Poor*	**Good***	*Poor*	*Very poor*	-
Sensitivity to wide-area gradual thinning in transmission	*Poor*	Average	*Poor*	**Very good**	**Good**	*Poor*	-

Bold text indicates desirable performance; *italic text* indicates poor performance.
*When mode cut-off is possible.
- Not investigated due to poor performance on other factors.

In conclusion, this chapter recommends a combination of two or more methods when inspecting for corrosion at inaccessible locations such pipe supports. The A1 mode at around 20 MHz-mm in reflection should be used for severe, sharp, pitting-type defects; its short wavelength (~2 mm in a 10 mm thick plate) means that it is the only method among those studied that will be capable of detecting localised pitting where the defect diameter might be in the order of the pipe thickness (Khalili and Cawley, 2016). Long range guided waves in reflection are most suitable for larger area thinning and the SH1 mode in transmission is particularly suitable for the detection of gradual, shallower defects, and can also be used in reflection over a range of defect morphologies.

Chapter 6

Sensitivity to 3-D Defects in the High Frequency-Thickness Regime

Following previous work carried out in 2-D, which suggested attractive properties of the A1 mode when testing for small, sharp defects in reflection, this chapter investigates the sensitivity of the A1 mode at 18 MHz-mm for square and circular 3-D holes which were considered to be extremes of no flat face normal to the beam and full face normal to it respectively; in practice a corrosion pit is likely to have a profile between these extremes. Finally, the chapter aims to offer a generalisation of the results for various combinations of defect size and plate thickness (t) values.

The chapter starts by outlining the potential issues when testing for localised, pitting-type corrosion defects. Next, the effect of different 3-D defect shapes, sizes and depths on the reflection characteristics of the A1 mode are investigated numerically. These predictions are then used to produce the reflection maps of the A1 mode for various defect sizes and depths which are verified experimentally. Finally the chapter goes on to demonstrate the advantages and disadvantages of implementing the A1 mode, at high frequency-thickness products, for the inspection of localised, sharp, pitting-type defects in a realistic test setup. This work is submitted to NDT&E Int. 2018 [P4] and the chapter follows the structure of the paper.

6.1 Introduction

Localised, pitting type defects such as those shown in Figure 6.1 are a concern, and are difficult to detect due to the low sensitivity of the generic guided wave methods, as discussed in Chapter 5; here it was also shown that raising the frequency content, in the case of the A1 mode, significantly improves the sensitivity to deep pits while the excited Lamb modes exhibit very low surface motion which reduces the sensitivity of the method to surface features such as pipe supports/T-joints (Balasubramaniam et al., 2012; Chandrasekaran et al., 2010; Jayaraman et al., 2009; Swaminathan et al., 2011). In Chapter 4, we have shown that with careful transduction, a wave packet dominated by the A1 mode can be reliably generated at high frequency-thickness products with both wedge coupled piezoelectric and EMAT probes.

Figure 6.1: *Photograph of deep, highly localised pits on the surface of a pipe located underneath a support (Burch, 2016).*

Figure 6.2a shows the Lamb wave dispersion curves for a steel plate where the excitation region of the A1 mode is indicated; Figure 6.2b illustrates the mode shape of the A1 mode at 18 MHz-mm (in a 10 mm thick steel plate). As previously discussed in Chapters 3, 4 and 5, a number of modes can potentially exist at the frequency-thickness regime of interest; since the sensitivity of a measurement is related to the signal to coherent noise ratio, where the coherent noise is generated by the excitation of undesired modes, Chapter 3 presents a great deal of work carried out to enable single mode transduction. As also discussed in Chapter 4, by understanding the effect of various excitation parameters on the frequency and wavenumber bandwidths of the excitation force, a wave packet dominated by the A1 mode can be generated at around 20 MHz-mm via both angled piezoelectric and EMAT probes. The performance of the A1 mode was then compared to other corrosion inspection techniques in Chapter 5, where it was concluded that the A1 mode was the least affected by surface features such as surface roughness, coatings, T-joints etc. because of its small surface motion as evident in Figure 6.2b; this method also offered the best sensitivity to small diameter, sharp, severe defects due to its raised frequency content. Additionally, it was demonstrated in Chapter 5 that, contrary to the low frequency guided waves (Demma et al., 2004; Lowe et al., 2002; Lowe and Diligent, 2002), the reflection coefficient of the A1 mode from a 2-D rectangular notch is almost independent of its axial extent. However, the predictions carried out in previous chapters have been on 2-D notches, though Balasubramaniam et al. have done experiments of HOMC on holes of various diameters (Ratnam et al., 2012; Satyarnarayan et al., 2008). It is meanwhile not clear how the outline shape of a 3-D defect influences the sensitivity of the method.

This chapter investigates the reflection of the A1 mode from 3-D square and circular holes of different diameter/size and depth using finite element analysis validated by experiments and aims to offer a generalisation of the results for various combinations of defect size and plate thickness values for a given frequency-thickness product.

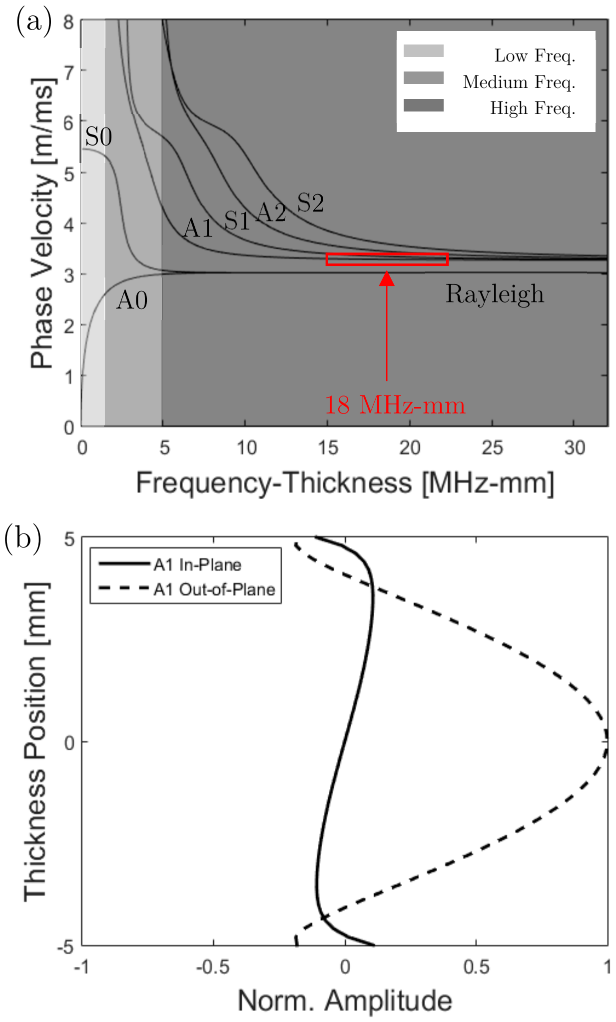

Figure 6.2: *(a) Lamb wave phase velocity dispersion curves in steel plate; (b) Normalised mode shape of the A1 mode at 18 MHz-mm; generated using DISPERSE (Pavlakovic et al., 1997) software.*

Section 6.2 gives an overview of different parameters used in this study along with a brief introduction of the setup used in the FE models. The effect of depth and width on the reflection ratio of the A1 mode for both square and circular holes is investigated and presented in Section 6.3. Then these predictions are verified experimentally in Section 6.4 and the findings are summarised in Section 6.5.

6.2 Finite Element Models

In order to assess the interaction of the A1 mode with 3-D defects of various depths and sizes, finite element (FE) analysis was employed. FE was deemed to be a useful tool as it allows the investigation of a large number of defect shapes/sizes which would be costly to examine experimentally. Since the wavelength of the A1 mode in the frequency range of interest is of the order of 1-2 mm and the defects of concern are typically of the order of the plate thickness in diameter, the defects extend over several wavelengths so the reflection obtained will be a strong function of the defect shape. In this chapter, two extremes are considered: a circular defect in which there is no planar surface normal to the incident wave, and a square defect oriented with one face normal to the beam.

Most of the predictions used a 10 mm thick plate but a few simulations with other thicknesses were also run (results not included in this chapter for brevity) in order to confirm that the reflection behaviour is controlled by the frequency-thickness product, the defect depth expressed as a fraction of the overall plate thickness and the defect lateral extent expressed as a multiple of the plate thickness.

The study of A1 mode reflection from defects was carried out at 18 MHz-mm, which in a 10 mm thick plate corresponds to a centre frequency of 1.8 MHz and a wavelength of around 2 mm; FE was carried out on ABAQUS CAE commercial package (Abaqus 6.14, 2014) and in order to ensure the stability and accuracy of the simulations, cubic elements (C3D8R) with side length of 0.1 mm were used (the defects were created by removing elements from the model). The original plan was to simulate a typical inspection in which a 2t diameter transducer (20 mm in a 10 mm thick plate) might be located ~100t (1 m in a 10 mm thick plate) from the defect; however, this proved to be impractical as the model would be too large.

In order to make the simulations practical, a short length of plate was modelled, taking advantage of the plane of symmetry through the defect, as shown in Figure 6.3. A typical model had around 100 million degrees of freedom and took 8 hours to run on a data cruncher with an 8-core Intel Xeon E5-2690 processor (Intel®, 2017) and 256GB of memory. The results were then extrapolated out to 100t range (1 m in a 10 mm thick plate) which proved to be satisfactory for small defects but led to problems with larger defects, as explained below.

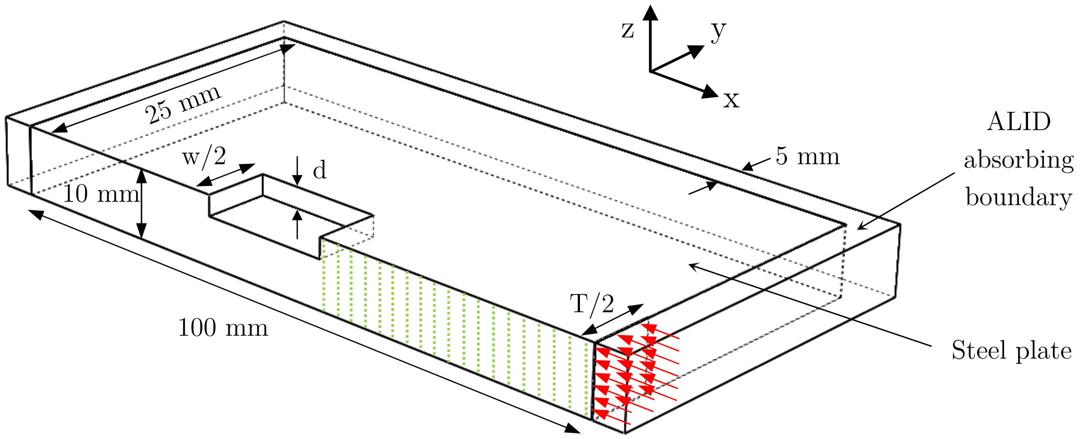

Figure 6.3: *Schematic of the FE setup with the plane of symmetry through the defect. The red arrows represent the mode-shape excitation along the equivalent width of the transducer; the green dotted lines show the mode-shape reception of the reflected wave.*

Figure 6.3 displays the general FE setup used in this study; here the mid-plane cross-section is shown for clarity. Due to the size limitation of the model, the generation of the A1 mode was done by exciting the mode-shape (shown in Figure 6.2b) through the thickness of the plate and repeated along the equivalent width of the transducer (T) (shown as red arrows in Figure 6.3); here the excitation signal in time was a 5-cycle Hanning windowed toneburst at 1.8 MHz centre frequency. Mode-shape excitation involves the application of force along the plate thickness weighted according to the desired mode-shape (at centre frequency, assuming minimal change across the frequency bandwidth) which allows pure mode transduction; additionally, a typical transducer size (T) of 2t (20 mm in a 10 mm thick plate) was used for the FE predictions as it has been shown in Chapters 3, 4 and 5, to allow practical excitation of a dominant A1 mode; it is important to note that the beam spread of the incident wave, over the propagation distances of interest, was assumed to be negligible due to the small wavelength of the A1 mode which results in the transducer being multiple wavelengths in size. However, this led to some issues with extrapolation as the defect was in the near field of the transducer (~ 50 mm). Some simulations were also run with a plane wave source and very similar results were obtained with the smaller defects.

The reflection was recorded via monitoring points located through the thickness (shown as green dotted lines in Figure 6.3) where mode-shape reception was carried out in order to obtain an accurate reflection amplitude of the A1 mode from the detect; this process involved summing the displacements over the cross-section weighted according to the corresponding mode-shape. The A1 mode reflection amplitudes were then plotted against their propagation distance and fitted with a power-law function which allowed extrapolation for longer distances. Lastly, the reflection ratio was calculated by comparing the predicted reflection amplitude for a given propagation distance and the incident wave amplitude of the A1 mode obtained on an undamaged plate model. This chapter aims to compute typical signals that would be obtained at about 100t stand-off (1 m in a 10 mm thick plate) as in a practical test. As also illustrated in Figure 6.3, a 5 mm wide Absorbing Layers using Increasing Damping (ALID) (Liu and Quek Jerry, 2003; Rajagopal et al., 2012) boundary was placed around the steel plate to eliminate edge reflections.

6.3 Results

In order to understand the behaviour of the A1 mode when interacting with square and circular holes, simulations were carried for various defect depths of 20% to 50% of the plate thickness (t) as well as for different normalised (to plate thickness) widths/diameters of 0.2t to 4t. As mentioned above, due to the small plate model, the reflection amplitude of the A1 mode was extrapolated for a 100t (1 m in 10 mm plate) propagation length in order to replicate a typical inspection setup. Figure 6.4 illustrates the A1 mode reflection amplitude against the propagation distance for square holes with widths of 0.5t, 1t, 3t and 4t at 50% depth, where superimposed are the power law functions used to extrapolate the results. The near field lengths of these defects are approximately 3 mm, 12.5 mm, 112.5 mm, and 200 mm respectively so the 0.5t and 1t defects are in the far field and this is confirmed by the power law decay functions being close to $x^{-0.5}$ as required in the far field. However, the larger defects are in the near field, as confirmed by the power law functions being far from $x^{-0.5}$. The extrapolation in these cases is therefore invalid; the results are presented for completeness but should be treated with caution.

Figure 6.5 illustrates the A1 mode reflection amplitude against the propagation distance for circular holes with widths of 1t, 2t, 3t and 4t at 50% depth, where superimposed are the power law functions used to extrapolate the results.

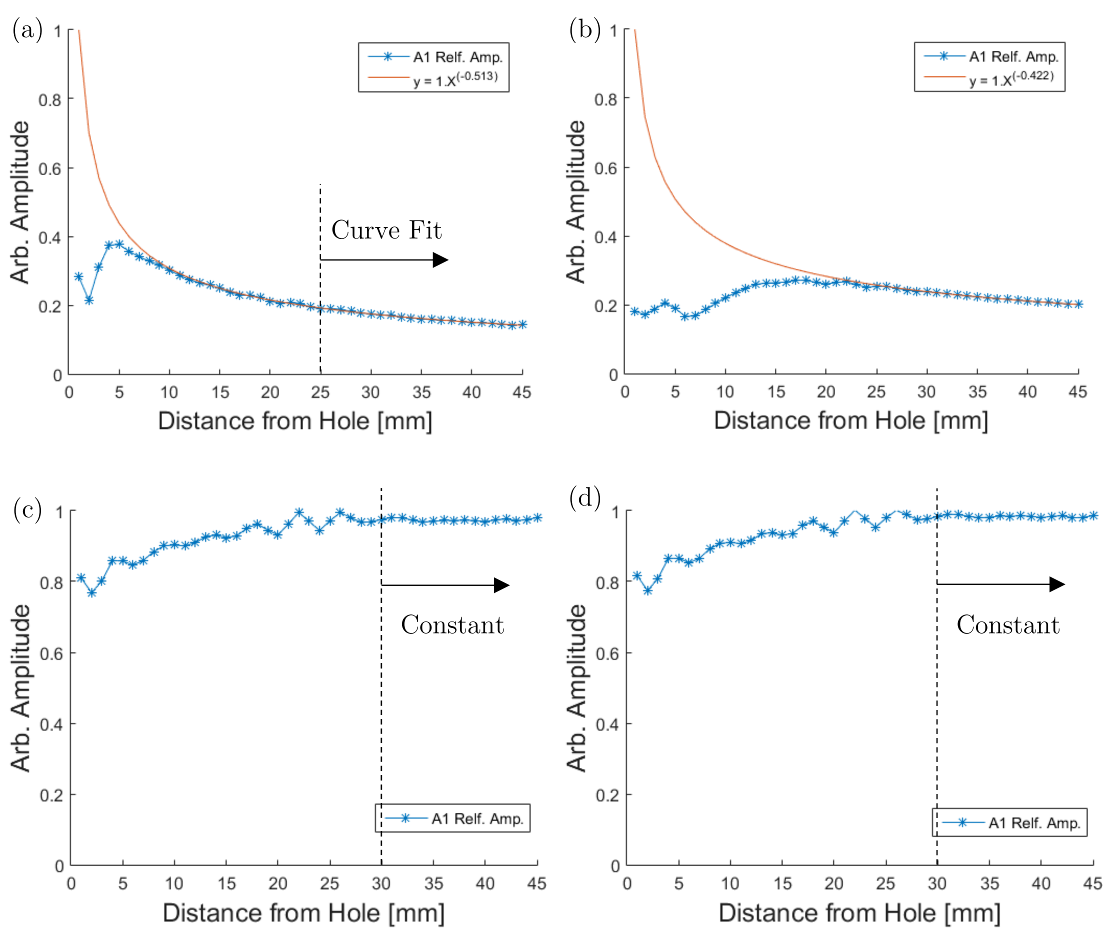

Figure 6.4: *Predicted reflection amplitude of the A1 mode (blue) from a 50% depth square hole as a function of the propagation distance for defect widths (a) 0.5t; (b) 1t; (c) 3t; (d) 4t. The red curve represent the power law function fitted to the A1 mode reflection amplitude.*

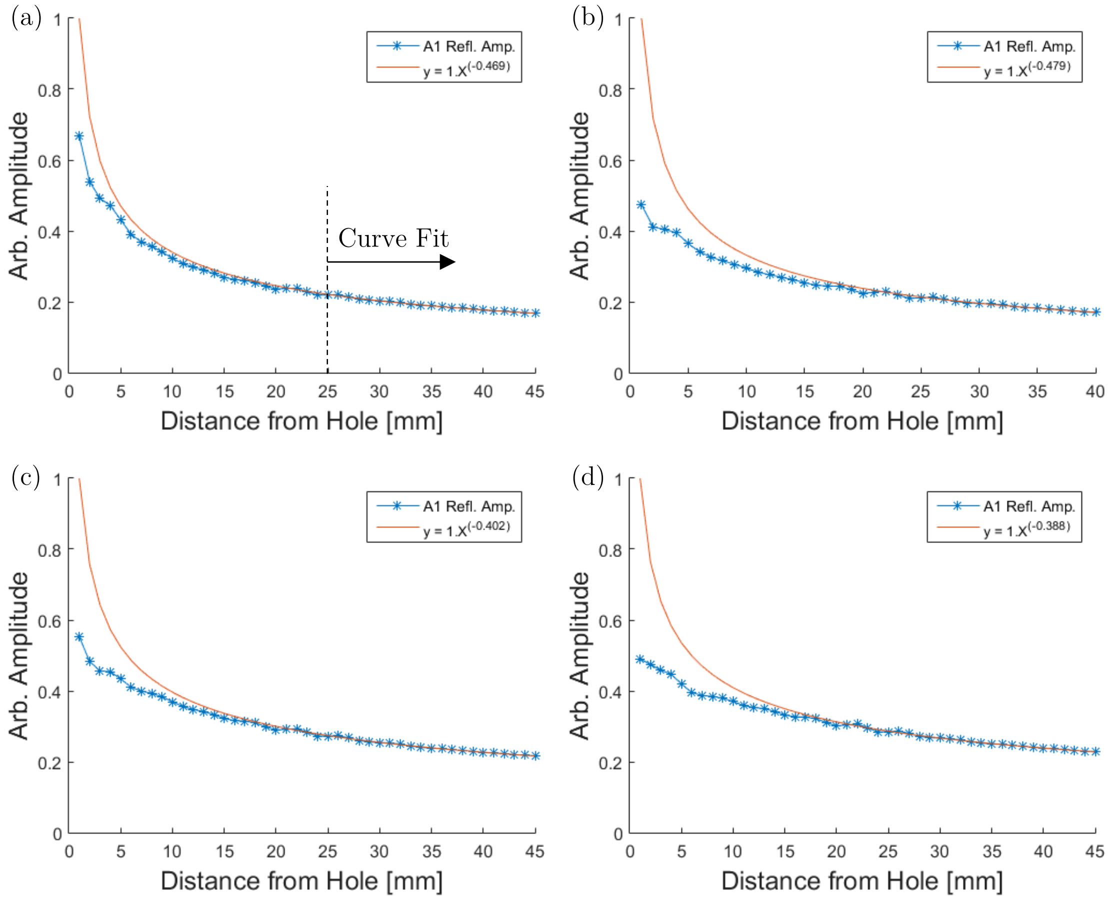

Figure 6.5: *Predicted reflection amplitude of the A1 mode (blue) from a 50% depth circular hole as a function of the propagation distance for defect widths of (a) 1t; (b) 2t; (c) 3t; (d) 4t. The red curve represent the power law function fitted to the A1 mode reflection amplitude.*

Here, as indicated by the reflection amplitude decay power functions, the near field effect is negligible for 1t and 2t defects as shown in Figures 6.5a and 6.5b respectively. As mentioned before, in the case of 3t and 4t defects, due to the near field issue, the results for such defect sizes should be treated with caution.

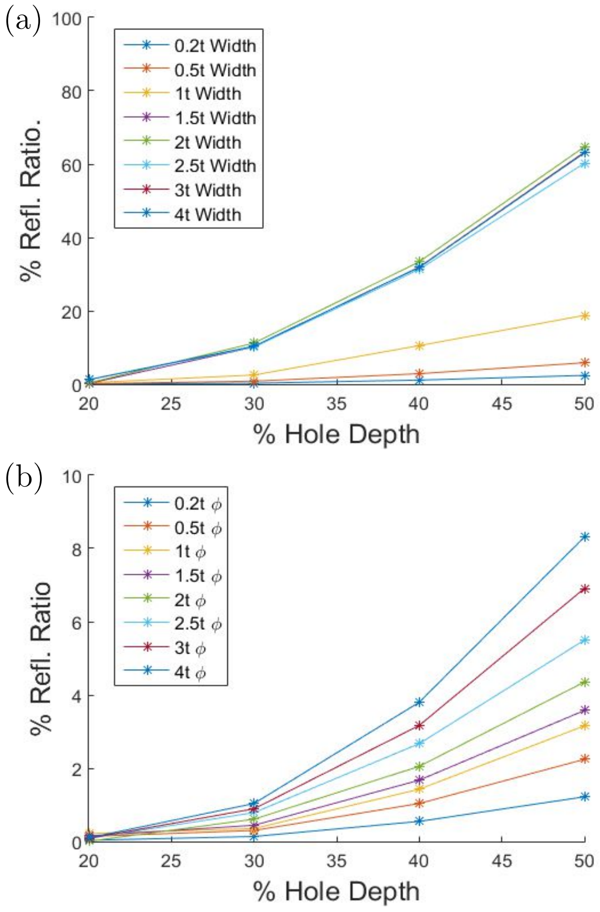

Figure 6.6: *Predicted reflection ratio of the A1 mode around 1 m from the defect as a function of the defect depth for (a) square hole; (b) circular hole. Note the difference in y-axis scale between the two cases; points joined by straight lines to improve clarity.*

Figure 6.6a shows the reflection ratio of the A1 mode from a square hole as a function of its depth. It is clear that defects with depths of 20% or lower are very difficult to detect through reflection due to the mode-shape of the A1 mode (Figure 6.2b) that exhibits low surface motion at 18 MHz-mm, while the method shows good sensitivity to deeper defects. It is also evident that square holes with widths of 1.5t or larger were predicted to have similar reflection characteristics. In such cases, the defect acts as a planar source (although the displacement pattern is not uniform across the face of the defect), meaning that, depending on the size of the defect, it exhibits a near field length, after which the reflection amplitude decays according to $x^{-0.5}$. Therefore, even though reflection ratios, over short propagation distances, were predicted to be constant for larger defects, it would be expected that due to the far field amplitude decay, the reflection ratios would in fact vary, hence the predicted results must be treated with caution. Figure 6.6b shows the corresponding result for circular holes; here the difference in the y-axis scale between Figures 6.6a and 6.6b should be noted. Contrary to the square hole case, the beam spread effect on the reflected signal is much more significant for circular holes, due to the absence of a planar surface normal to the incident wave, which explains the much smaller reflection ratio values.

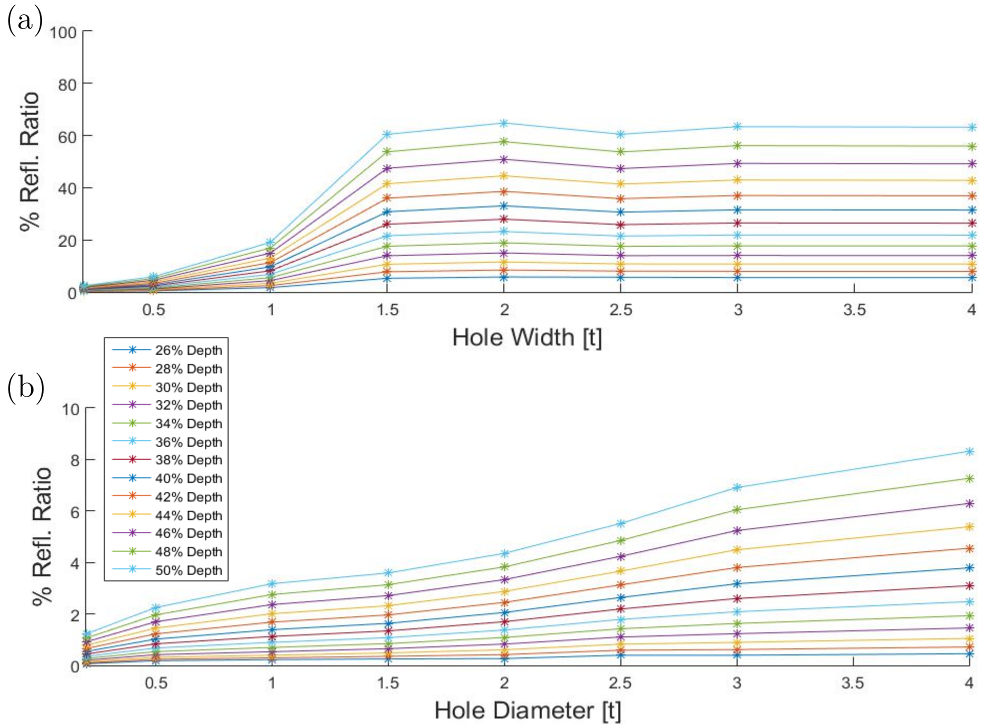

Figure 6.7: *Predicted reflection ratio of the A1 mode around 1 m from the defect as a function of the defect size for (a) square hole; (b) circular hole. The results were obtained for a 10 mm thick steel plate at a centre frequency of 1.8 MHz. Note the difference in y-axis scale between the two cases; points joined by straight lines to improve clarity.*

In order to obtain the reflection ratio values for different hole depths (shown in Figure 6.7), the results in Figure 6.6 were interpolated via polynomial curve fitting to each graph (not shown here). Figure 6.7a shows the reflection ratio of the A1 mode from a square hole as a function of its width; here for hole widths of 1.5t or larger; the predicted defect detectability is almost solely dependent on the hole depth, as beam spread becomes negligible. However, the extrapolation issues discussed above mean that the results must be treated with caution; even with a plane boundary, the reflection would reduce with distance in the far field of the transducer. It is also evident that because of the small wavelength (λ) of the A1 mode, this method is very sensitive to small defects (< 1t) where a width change of 0.2t is equivalent to the wavelength. Figure 6.7b shows the corresponding result for circular holes; the different y-axis scales between the figures should again be noted. Here the A1 mode generated higher reflection ratio values from larger diameter defects; this is because the larger reflection source, in this case a larger diameter hole, results in lower beam spread and hence a stronger reflection amplitude over a given propagation distance (note that in the far field, the reflection would reduce with distance, hence due the extrapolation issues for defects larger than 1t, the results must be treated with caution).

By cross-referencing the results from Figures 6.6 and 6.7, the reflection ratio map as a function of hole width/diameter and depth can be obtained. Figure 6.8 shows the reflection ratio map of the A1 mode around 100t from a square hole; here it is evident that this method shows good sensitivity to small, localised, severe defects e.g. square holes with 40% depth and as small as 0.5t. Figure 6.9 displays the reflection ratio map of the A1 mode for circular holes; here, the different contour scale to that of Figure 6.8 should be noted. As expected, the detectability is greatly reduced because of the significantly larger beam spread in the case of the circular hole but despite this, the A1 mode is predicted to have reasonable sensitivity from a 100t distance to small, severe circular holes e.g. holes with 50% depth and as small as 1t.

In both square and circular hole cases, it is shown that the reflection ratio obtained at a given width/diameter and depth is also obtained at smaller depth and larger hole width/diameter, hence suggesting that, for defect sizing purposes, it is important to know the hole width/diameter in order to interpret the reflection from a defect; this could be achieved by scanning across the defect and obtaining the width associated with the 6dB amplitude drop measured from the peak reflection reading. Otherwise, through the sole use of Figures 6.8 and 6.9, there is a risk of overestimating the severity of the defect (due to the extrapolation issues for defects larger than 1t, the results must be treated with caution).

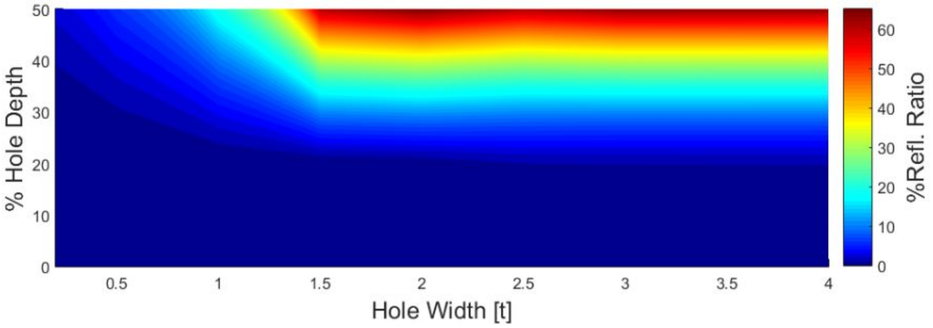

Figure 6.8: *Predicted reflection ratio map of the A1 mode around 1 m from a square hole for different widths and depths. The results were obtained for a 10 mm thick steel plate at a centre frequency of 1.8 MHz (due to the extrapolation issues for defects larger than 1t, the results must be treated with caution).*

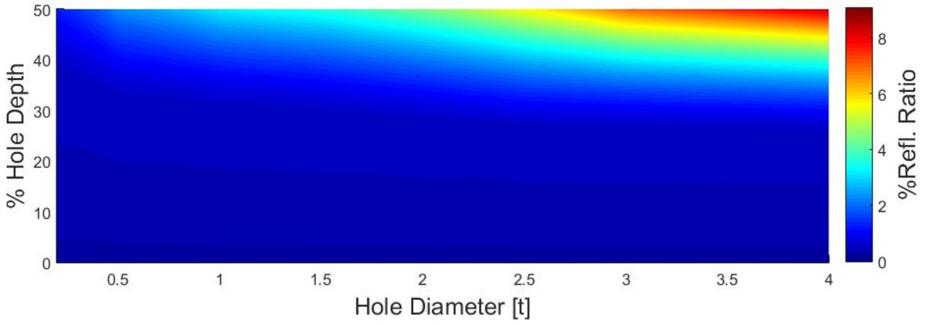

Figure 6.9: *Predicted reflection ratio map of the A1 mode around 1m from a circular hole for different diameters and depths. The results were obtained for a 10 mm thick steel plate at a centre frequency of 1.8 MHz (due to the extrapolation issues for defects larger than 1t, the results must be treated with caution).*

6.4 Experimental Validation

In order to establish the validity of the FE predictions on the reflection characteristics of the A1 mode from square and circular holes, experimental measurements on a steel plate were performed; defect widths/diameters of 1t, 2t and 3t, all at 50% depth were considered. As in the predictions, the reflection ratio was calculated by comparing the reflection amplitude and the transmitted amplitude of the A1 mode for the same propagation distance obtained on an undamaged section of the plate.

6.4.1 Experimental setup

Figure 6.10 illustrates the setup used to record the reflection time-traces from different sizes of defect on a 10 mm thick steel plate. The excitation toneburst was produced via a HandyScope HS3 connected to a computer, the signal being amplified using a RITEC RPR4000 gated amplifier (Ritec Inc. Warwick, RI) and fed into the transmitter. In order to generate a signal dominated by the A1 mode, as shown in previous chapters (Khalili and Cawley, 2016, 2018a, 2018b), the excitation was performed at 18 MHz-mm (1.8 MHz centre frequency) via a 5-cycle Hanning-windowed toneburst with a 1-inch diameter 2.25 MHz centre frequency piezoelectric compression wave transducer (Panametrics A104S-RB) on a gel coupled 60° PMMA wedge (c_{Lw}= 2710 m/s, ρ = 1180 kg/m^3). A similar probe was used for reception where the output signal was further amplified and recorded on a digital oscilloscope. In order to eliminate probe coupling issues which can result in inconsistent signal amplitude, each measurement was repeated 5 times; the standard deviation of all the recorded amplitudes was found to be <3% of the mean amplitude for both square and circular hole cases.

Due to the nature of the machining process, the square holes exhibited round corners with 1.5 mm radius (as indicated in Figure 6.10) and therefore to ensure accurate comparison, additional FE models were performed which incorporated rounded corners.

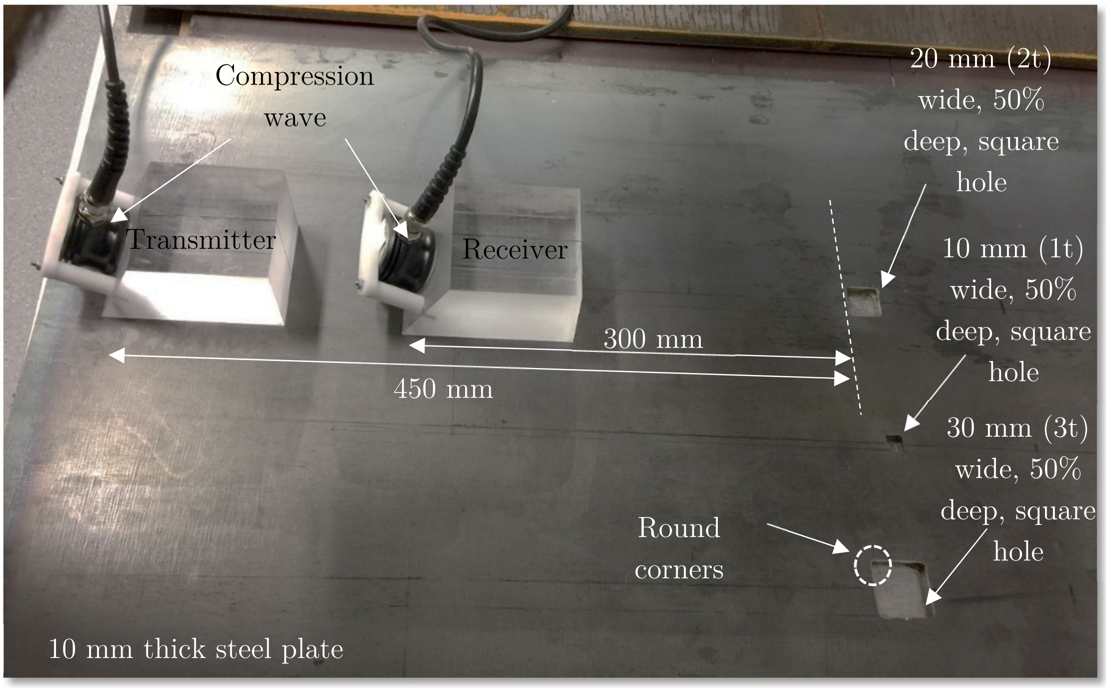

Figure 6.10: *Picture of the 1-inch diameter compression wave piezoelectric transducer on a 60° PMMA wedge probes, positioned to record the reflection time-trace from a square hole machined on a 10 mm steel plate.*

6.4.2 Results

Figure 6.11 illustrates the reflection time-traces of the Lamb modes when interacting with 50% deep, square holes with 1t (b), 2t (c) and 3t (d) widths. The time-traces were normalised to the transmitted Lamb wave signal (a) which was recorded separately on an undamaged section of the steel plate; time-of-flight calculations showed that the transmitted wave is dominated by the A1 mode. Table 6.1 displays the experimental (shown in Figure 6.11) and FE reflection ratios of the A1 mode for different square hole widths with a constant 50% depth (due to the FE extrapolation issues for defects larger than 1t, the results must be treated with caution); the FE results for square holes with sharp corners are also included for comparison purposes. The results show good agreement for the square holes with round corners; higher reflection ratios are predicted for the 2t ideal square hole case since the larger effective size gives lower beam spread of the reflected signal (note the FE extrapolation issues meaning the results must be treated with caution; even with a plane boundary, the reflection would reduce with distance in the far field of the transducer). The predictions for both the square and rounded corners and the experiments all show higher reflection ratio for the 2t width compared to the 3t case. The reasons for this are not clear and have not been pursued since a corrosion type defect with a substantial dimension normal to the beam is unusual and gives a large reflection at all sizes and so is easy to detect.

Figure 6.12 illustrates the reflection time-traces of the Lamb modes when interacting with 50% deep, circular holes with 1t (b), 2t (c) and 3t (d) diameters; the different y-axis scales between Figures 6.11 and 6.12 should be noted. Similar to Figure 6.11, the time-traces were normalised to the transmitted Lamb wave signal (a) which was recorded separately on an undamaged section of the steel plate; again, it is shown that the transmitted wave is dominated by the A1 mode. It is clear that the amplitude of the reflected signal increases for larger diameter defects because of the lower reflection beam spread for larger holes. Table 6.2 displays the experimental (shown in Figure 6.12) and FE reflection ratios of the A1 mode for different circular hole diameters; there is good agreement between the predicted and measured reflection ratios (due to the FE extrapolation issues for defects larger than 1t, the results must be treated with caution).

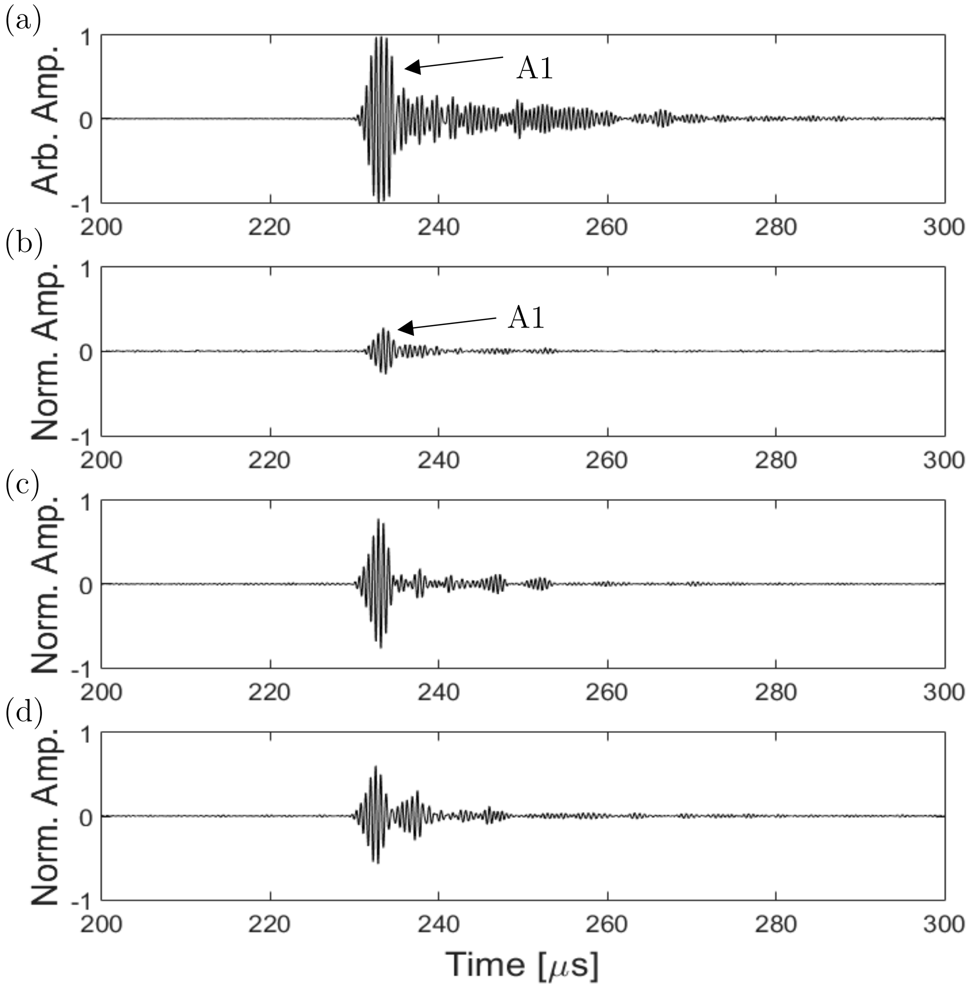

Figure 6.11: *(a) Transmitted Lamb wave signals at 18 MHz-mm on undamaged section of 10 mm thick steel plate obtained in pitch-catch configuration with around 750 mm probe separation; (b) reflection time-trace obtained in pitch-catch configuration at around 300 mm behind a 10 mm (1t) wide square hole at 50% depth; (c) as (b) for a 20 mm (2t) wide square hole at 50% depth; (d) as (b) for a 30 mm (3t) wide square hole at 50% depth. Time-traces obtained using two similar probes consisting of a 1 inch diameter compression wave piezoelectric transducer mounted on a gel coupled 60° PMMA wedge where the excitation was performed with a 5-cycle Hanning windowed toneburst at 1.8 MHz centre frequency.*

Table 6.1: *Reflection ratio % of the A1 mode around 300 mm from different sizes of square hole with round corners at a constant depth of 50% obtained experimentally shown alongside the FE predictions (note the extrapolation issues discussed above, for defects larger than 1t); the FE results for square hole with sharp corners are also displaced for comparison; all results have been obtained at 18 MHz-mm for a 10 mm steel plate.*

Square hole width (mm)	**Exp. A1 refl. ratio %**	**FE A1 refl. ratio %**	**FE A1 refl. ratio % (sq. corners)**
10 (1t)	25	20	31
20 (2t)	69	67	68
30 (3t)	57	57	58

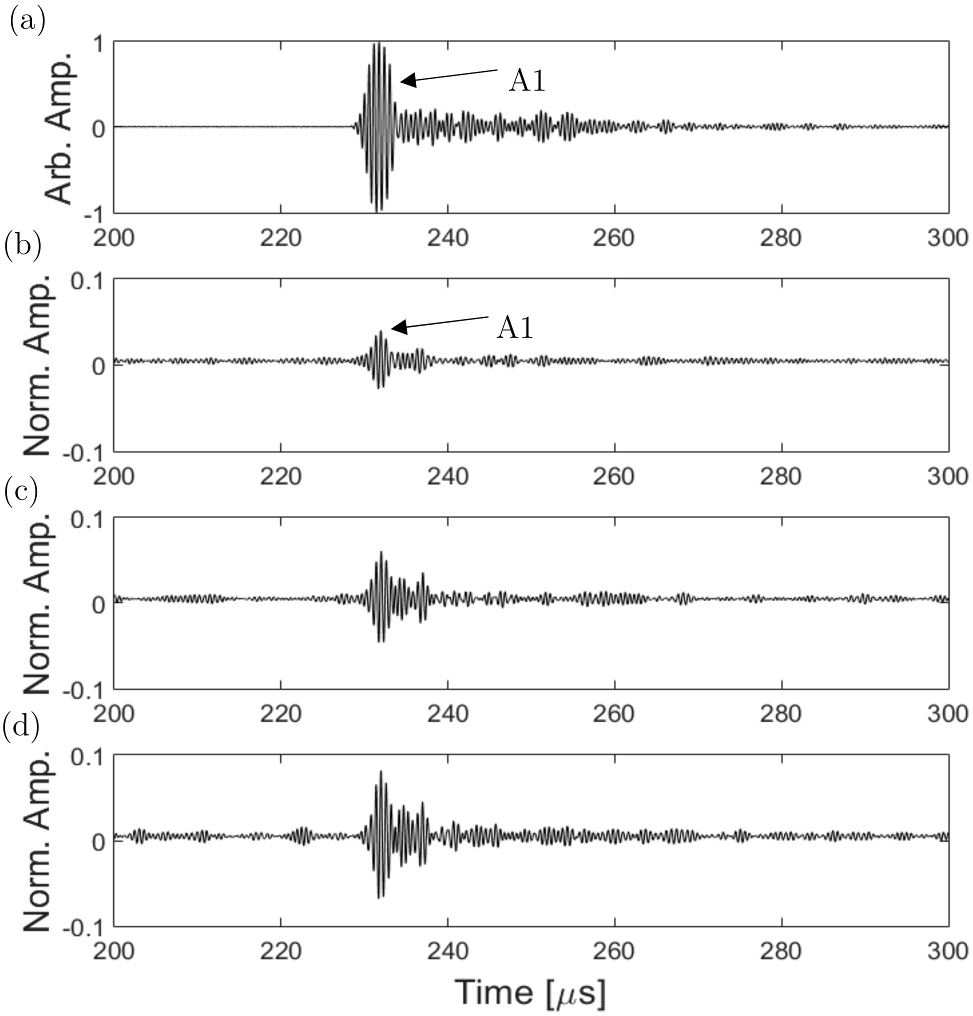

Figure 6.12: *(a) Transmitted Lamb wave signals at 18 MHz-mm on undamaged section of 10 mm thick steel plate obtained in pitch-catch configuration with around 750 mm probe separation; (b) reflection time-trace obtained in pitch-catch configuration at around 300 mm behind a 10 mm (1t) diameter circular hole at 50% depth; (c) as (b) for a 20 mm (2t) diameter circular hole at 50% depth; (d) as (b) for a 30 mm (3t) diameter circular hole at 50% depth. Time-traces obtained using two similar probes consisting of a 1 inch diameter compression wave piezoelectric transducer mounted on a gel coupled 60° PMMA wedge where the excitation was performed with a 5-cycle Hanning windowed toneburst at 1.8 MHz centre frequency.*

Table 6.2: *Reflection ratio % of the A1 mode around 300 mm from different sizes of circular hole at a constant depth of 50% obtained experimentally shown alongside the FE predictions (note the extrapolation issues discussed above, for defects larger than 1t); all results have been obtained at 18 MHz-mm for a 10 mm steel plate.*

Circular hole diameter (mm)	**Exp. A1 refl. ratio %**	**FE A1 refl. ratio %**
10 (1t)	4.0	4.2
20 (2t)	6.1	6.0
30 (3t)	7.9	8.2

6.5 Conclusions

The A1 mode at 18 MHz-mm was considered for this study since in previous work done in 2-D (Khalili and Cawley, 2016, 2018a, 2018b), this method has been shown to exhibit attractive properties when testing for small, sharp defects in reflection. In order to understand the practical detectability of the method, this chapter studied the reflection of the A1 mode from 3-D defects. Here, two extremes were considered: a circular defect in which there is no planar surface normal to the incident wave, and a square defect oriented with one face normal to the beam. Numerical (FE) predictions were employed for various defect depths from 20% to 50% of the plate thickness (t) as well as for different normalised (to plate thickness) widths/diameters of 0.2t to 4t. In order to represent a practical test setup, excitation with a 1 inch transducer at 100t range was considered. This proved to be satisfactory for small defects but led to problems with larger defects as the limited size of the FE model meant the A1 mode reflection was captured in the near field for such defects.

Firstly, the reflection ratio of the A1 mode from idealised square holes was investigated. Here it was found that due to the small wavelength of the A1 mode at 18 MHz-mm (λ~2 mm in a 10 mm thick plate), the method is very sensitive to small defects, so from a 100t distance, square holes with 40% depth and as small as 0.5t were predicted to give a 3% reflection ratio, and so are likely to be detectable. The reflection ratio value plateaued for square holes larger than 1.5t as the beam spread effect of the reflected signal becomes negligible at the high frequencies involved. The reflection ratio of the A1 mode from circular holes was then studied where it was found that the beam spread effect is more significant due to the defect shape, which resulted in much smaller reflection ratio values; despite this, A1 mode showed reasonable sensitivity from a 100t distance meaning circular holes with 50% depth and as small as 1t were predicted to give around 3% reflection ratio, and so are likely to be detectable. Finally, experimental measurements were carried out on a 10 mm thick steel plate to validate the numerical predictions and showed good agreement with the predicted results.

This chapter demonstrates that in the worst (circular) case scenario, a defect as small as 1t, which at 40% depth gives a 1.5% reflection ratio and at 50% depth gives around 3% reflection ratio, is detectable from a range of 100t (1 m in a 10 mm wall thickness) using the A1 mode. It should be noted that, as mentioned before, the FE extrapolation results are reliable for 1t or smaller defect sizes meaning the overall conclusion of this chapter regarding the sensitivity of the A1 mode is still accurate. Therefore this method is an attractive tool for detection of defects of type shown in Figure 6.1; it can be used in conjunction with lower frequency methods for the detection of gradual defects as also discussed in the previous chapter (Khalili and Cawley, 2018b).

Chapter 7

Conclusions

7.1 Review of Thesis

In Chapter 2, the fundamental wave motion theory concerning bulk wave and guided wave propagation in isotropic materials was presented. The key properties of guided waves, such as dispersion and mode shapes, were then discussed, followed by the introduction of different frequency regimes concerning different guided wave inspection techniques. Finally the chapter outlined the use of 2-D and 3-D FE models to study the propagation of ultrasonic waves within bounded structures.

Chapter 3 primarily investigated the formation of the Higher Order Mode Cluster (HOMC) developed by Balasubramaniam et al. (Indian Institute of Technology Madras) at high frequency-thickness products, where it was found that the properties of HOMC are similar to those of the A1 mode. Following this, the chapter went on to establish the possibility of single mode transduction at the high modal density region of the dispersion curves.

In Chapter 4, the relative ability of wedge-mounted piezoelectric and meander coil EMAT probes towards single mode transduction at medium and high frequency-thickness products was explored. Firstly, the basic physics behind each transducer type was presented; then through analytical means, the advantages and limitations of each probe were explored. These predictions were used to find the appropriate transducer setup best suited for single mode transduction which were verified experimentally.

Chapter 5 set out to systematically compare the performance of the commonly used corrosion inspection techniques with that of the A1 mode. The effect of surface features such as roughness, coatings and T-joints on the propagation of each method was investigated analytically and numerically. Finally, the sensitivity of each technique to sharp and gradual defects were established numerically, followed by experimental validations.

Due to the attractive properties of the A1 mode indicated by the 2-D analysis of previous chapters, Chapter 6 investigated the sensitivity of the A1 mode at around 18 MHz-mm for square and circular 3-D holes and offered a generalization of the results for various combinations of defect size and plate thickness (t) values. Numerical predictions, backed up by experiments, were employed to obtain the reflection ratio of the A1 mode from 3-D defects in a typical inspection setup.

7.2 Key Contributions

The multi-modal nature of guided waves fundamentally limits the sensitivity of such methods and ultimately restricts the achievable performance of the inspection. Therefore the possibility of single mode excitation through careful transduction is very appealing as it can significantly reduce the inspection complexity and allow improvements to NDE such as enhanced signal-to-noise (SNR) ratio.

Testing for corrosion in the petrochemical industry has always been a significant challenge which takes up a large portion of the operating expenditure. Whereas major advancements have been made for the detection of general corrosion, inspection at inaccessible locations, such as at pipe supports, remains a demanding prospect, hence signifying the need for an alternative technique, capable of dealing with various surface conditions encountered when testing at such locations including weld patches, T-joints, rough surfaces and coatings. The approach shown in Chapter 3 presents the ability of single A1 mode inspection within a high modal density region of the dispersion curves; it has been shown that the properties of the HOMC are fundamentally those of the A1 mode while this method has been put on a sound scientific footing.

Based on the findings demonstrated in Chapter 3, the possibility of single mode excitation at medium and high frequency-thickness regimes using both wedge mounted piezoelectric and meander coil EMAT probes was pursued in Chapter 4. Here, the results showed that signals dominated by the A0 mode at 1.5 MHz-mm and also the A1 mode at 18 MHz-mm can be generated with both angled piezoelectric and EMAT probes, therefore facilitating the use of these modes in practical applications.

Prior to the application prospects however, the question remained on the performance of the A1 mode, compared to the currently known techniques, when used for corrosion inspection at inaccessible locations. Therefore, as shown in Chapter 5, a systematic performance comparison between the A1 mode and various guided wave and bulk wave methods was carried out which looked at the effects of various surface features commonly encountered when testing at inaccessible locations, in addition to different types of corrosion damage including sharp and gradual thickness loss. Here, it was shown that the A1 mode provides the best overall performance when dealing with surface features because of its low surface motion. Additionally a combination of two or more methods was suggested for corrosion inspection at inaccessible locations: the A1 mode in reflection for severe, sharp, pitting type defects; long range guided waves in reflection for large-area thinning and the SH1 mode in transmission for shallow, gradual defects.

Having demonstrated the potential attractiveness of the A1 mode and the ability to excite it, it was beneficial to investigate the sensitivity of the A1 mode, in reflection, to more realistic 3-D part-depth holes. By studying various hole depths and sizes [all normalised to waveguide thickness (t)], it was found that circular holes presented the worst case and even with these, a hole 1t in diameter with 50% depth gives a reflection ratio of around 3% and so is likely to be detectable. Square holes with a side normal to the beam give a much larger reflection ratio (19% for 1t side length, 50% depth case) and therefore a facet normal to the beam in an irregular defect will enhance its detectability. Hence the method is an attractive tool for the detection of localized, sharp, severe defects that will be missed by standard, lower frequency guided wave testing.

7.3 Future Work

An obvious candidate for future consideration is the use of the analytical model discussed in Chapters 3 and 4, in order to develop more advanced techniques for single mode transduction at various frequency-thickness regimes. This can be particularly attractive in the case of SH guided wave techniques since, at higher frequency-thickness products, the existing methods generate multiple modes and rely mainly on modal cut-off of the higher order modes for defect characterisation.

Another potential for future work is to improve the practicality of the A1 mode technique which can prove to be a challenge due to the low surface motion of this mode. Although it was shown that signals dominated by the A1 mode can be generated using a relatively simple EMAT probe, ultimately finding an optimal transducer setup in order to further enhance the SNR value is an attractive prospect.

Finally, this research project showcases a solution to a major industrial problem, which further emphasizes the commercial prospects of the single A1 mode method for the industry, where, as recommended in Chapter 5, the implementation of a multi-method setup would be a comprehensive tool for corrosion inspection at inaccessible locations.

7.4 Thesis Publications

[P1] P. Khalili and P. Cawley, “Excitation of single-mode Lamb waves at high-frequency-thickness products,” *IEEE Trans. Ultrason. Ferroelectr. Freq. Control*, vol. 63, no. 2, pp. 303–312, 2016.

[P2] P. Khalili and P. Cawley, “The choice of ultrasonic method for the detection of corrosion at inaccessible locations,” *NDT&E Int.*, vol. 99, pp. 80–92, 2018.

[P3] P. Khalili and P. Cawley, “Relative ability of wedge coupled piezoelectric and meander coil EMAT probes to generate single mode Lamb waves,” *IEEE Trans. Ultrason. Ferroelectr. Freq. Control*, vol. 65, no. 4, pp. 648–656, 2018.

[P4] P. Khalili and P. Cawley, “The reflection of the A1 Lamb mode in the high frequency-thickness regime from 3-D part-depth holes,” *Submitted to NDT&E Int.*, 2018.

References

Abaqus 6.14 2014, , Dassault Systems, *www.3ds.com.*

Achenbach, J.D., 1973, *Wave Propagation in Elastic Solids*, North-Holland Publishing Company, Amsterdam.

Alers, G.A., 1994, Application of special wave modes to industrial inspection problems, *Proceedings of the ASME Symposium on Wave Propagation and Emerging Technologies*, Chicago, USA.

Alleyne, D.N., 1991, *The Nondestructive Testing of Plates Using Ultrasonic Lamb Waves*, PhD Thesis, Imperial College London.

Alleyne, D.N. and Cawley, P., 1991, A two-dimensional Fourier transform method for the measurement of propagating multimode signals, *The Journal of the Acoustical Society of America*, Vol. 89 No. 3, pp. 1159–1168.

Alleyne, D.N. and Cawley, P., 1992a, Optimization of lamb wave inspection techniques, *NDT & E International*, Vol. 25 No. 1, pp. 11–22.

Alleyne, D.N. and Cawley, P., 1992b, The interaction of Lamb waves with defects, *IEEE Transactions on Ultrasonics, Ferroelectrics and Frequency Control*, Vol. 39 No. 3, pp. 381–397.

Alleyne, D.N., Lowe, M.J.S. and Cawley, P., 1998, The reflection of guided waves from circumferential notches in pipes, *Journal of Applied Mechanics*, Vol. 65 No. 3, pp. 635–641.

Alleyne, D.N., Pavlakovic, B., Lowe, M.J.S. and Cawley, P., 2001, Rapid long-range inspection of chemical plant pipework using guided waves, *Insight: Non-Destructive Testing and Condition Monitoring*, Vol. 43 No. 2, pp. 93–96.

Attarian, V.A., Cegla, F.B. and Cawley, P., 2014, Long-term stability of guided wave structural health monitoring using distributed adhesively bonded piezoelectric transducers, *Structural Health Monitoring*, Vol. 13 No. 3, pp. 265–280.

Auld, B.A., 1991, *Acoustic Fields and Waves in Solids*, Krieger Publishing Company, Malabar, Florida.

Balasubramaniam, B.K., Swaminathan, A.A. and Venkataraman, K.S., 2012, Higher Order Modes Cluster (HOMC) guided waves technique for corrosion detection, *18th World Conference on Nondestructive Testing.*

Bass, F.G. and Fuks, I.M., 1979, *Wave Scattering from Statistically Rough Surfaces*, edited by Haar, D. ter;, 1st ed., Pergamon.

Belanger, P., 2014, High order shear horizontal modes for minimum remnant thickness, *Ultrasonics*, Elsevier B.V., Vol. 54 No. 4, pp. 1078–1087.

Belanger, P. and Cawley, P., 2009, Feasibility of low frequency straight-ray guided wave tomography, *NDT & E International*, Vol. 42 No. 2, pp. 113–119.

Belanger, P., Cawley, P. and Simonetti, F., 2010, Guided wave diffraction tomography within the born approximation, *IEEE Transactions on Ultrasonics, Ferroelectrics and Frequency Control*, Vol. 57 No. 6, pp. 1405–1418.

Birks, A.S., Green, R.E. and Mclntire, P., 1991, *Nondestructive Testing Handbook: Vol. 7*, 2nd ed., American Society of Nondestructive Testing, Columbus, OH.

Bloom, J.G.P., Heerens, G.-J. and Volker, A.W.F., 2009, Opportunities for permanent corrosion monitoring of pipelines using guided wave tomography, *Volume 5: High Pressure Technology; Nondestructive Evaluation Division; Student Paper Competition*, Vol. 5, ASME, pp. 225–230.

Brekhovskikh, L., 1976, *Waves in Layered Media*, 2nd ed., Academic Press, New York, USA.

Burch, S.F., 2016, Inspection of corrosion under pipe supports (CUPS) – industry perspective and inspection challenges, *Imperial College/HOIS Workshop on GW Tomography for CUPS Inspection.*

Burch, S.F., Collett, N.J., Terpstra, S. and Hoekstra, M. V., 2007, M-skip: a quantitative technique for the measurement of wall loss in inaccessible components, *Insight - Non-Destructive Testing and Condition Monitoring*, Vol. 49 No. 4, pp. 190–194.

Carandente, R. and Cawley, P., 2012, The effect of complex defect profiles on the reflection of the fundamental torsional mode in pipes, *NDT & E International*, Vol. 46 No. 1, pp. 41–47.

Carandente, R., Ma, J. and Cawley, P., 2010, The scattering of the fundamental torsional mode from axi-symmetric defects with varying depth profile in pipes, *The Journal of the Acoustical Society of America*, Vol. 127 No. 6, pp. 3440–3448.

Cawley, P., Lowe, M.J.S., Alleyne, D.N., Pavlakovic, B. and Wilcox, P.D., 2003, Practical long range guided wave testing: applications to pipes and rail, *Materials Evaluation*, Vol. 61 No. 1, pp. 66–74.

Chandrasekaran, J., Anto, I., Balasubramaniam, K. and Venkataraman, K.S., 2009, Higher order modes cluster (HOMC) guided waves for online defect detection in annular plate region of above-ground storage tanks, *Insight: Non-Destructive Testing and Condition Monitoring*, Vol. 51 No. 11, pp. 606–611.

Chandrasekaran, J., Krishnamurthy, C. V. and Balasubramaniam, K., 2010, Axial higher order modes cluster (A-HOMC) guided wave for pipe inspection, *AIP Conference Proceedings*, Vol. 1211 No. 1, pp. 161–168.

Chimenti, D.E. and Lobkis, O.I., 1997, Effect of rough surfaces on guided waves in plates, *Review of Progress in Quantitative Nondestructive Evaluation*, Springer US, Boston, MA, pp. 169–176.

Clarke, T., Simonetti, F., Rohklin, S. and Cawley, P., 2009, Development of a low-frequency high purity A0 mode transducer for SHM applications, *IEEE Transactions on Ultrasonics, Ferroelectrics and Frequency Control*, Vol. 56 No. 7, pp. 1457–1468.

Clarke, T., Simonetti, F., Rokhlin, S. and Cawley, P., 2008, Evaluation of the temperature stability of a low- frequency A0 mode transducer developed for SHM applications, *AIP Conference Proceedings*, Vol. 975, pp. 910–917.

Corrosion Inspection Technologies, 2016, Corrosion under pipe supports inspections, *www.cit-Corrosion-Group.com.*

Demma, A., Cawley, P., Lowe, M., Roosenbrand, A.G. and Pavlakovic, B., 2004, The reflection of guided waves from notches in pipes: A guide for interpreting corrosion measurements, *NDT and E International*, Vol. 37 No. 3, pp. 167–180.

Demma, a, Cawley, P. and Lowe, M., 2003, Scattering of the fundamental shear horizontal mode from steps and notches in plates, *The Journal of the*

Acoustical Society of America, Vol. 113 No. 4, pp. 1880–1891.

DISPERSE: User’s Manual, Version 2.0.20a, 2013, , Non-Destructive Testing Laboratory, Imperial College London, London.

Ditri, J.J., Rose, J.L. and Chen, G., 1992, Mode selection criteria for defect detection optimization using Lamb waves, *Review of Progress in Quantitative Nondestructive Evaluation*, Vol. 11B, pp. 2109–2115.

Ditri, J.J., Rose, J.L. and Pilarski, A., 1993, Generation of guided waves in hollow cylinders by wedge and comb type transducers, *Review of Progress in Quantitative Nondestructive Evaluation*, Vol. 12A, pp. 211–218.

Dixon, S. and Palmer, S.B., 2004, Wideband low frequency generation and detection of Lamb and Rayleigh waves using electromagnetic acoustic transducers (EMATs), *Ultrasonics*, Vol. 42 No. 10, pp. 1129–1136.

Dobson, J. and Cawley, P., 2017, The scattering of torsional guided waves from Gaussian rough surfaces in pipework, *The Journal of the Acoustical Society of America*, Vol. 141 No. 3, pp. 1852–1861.

Dransfeld, K. and Salzmann, E., 1970, Excitation, detection, and attenuation of high-frequency elastic surface waves, *Physical Acoustics*, vol. 7., New York, USA, pp. 219–272.

Drozdz, M.B., 2008, *Efficient Finite Element Modelling of Ultrasonic Waves in Elastic Media*, PhD Thesis, Imperial College London.

Duffill, C. and Silk, M.G., 2000, Ultrasonic Inspection, United States Patent, No. 6105431, USA.

Erhard, A. and Kröning, E., 1984, Propagation and utilization of ultrasonic creeping waves, *Materialprüfung*, Vol. 26, pp. 323–326.

Galvagni, A. and Cawley, P., 2011, The reflection of guided waves from simple supports in pipes, *The Journal of the Acoustical Society of America*, Vol. 129 No. 4, pp. 1869–1880.

Graff, K.F., 1975, *Wave Motion in Elastic Solids*, Clarendon Press, Oxford, U.K.

Guo, Z., Achenbach, J.D. and Krishnaswamy, S., 1997, EMAT generation and laser detection of single lamb wave modes, *Ultrasonics*, Vol. 35 No. 6, pp. 423–429.

Hay, T.R. and Rose, J.L., 2002, Flexible PVDF comb transducers for excitation of axisymmetric guided waves in pipe, *Sensors and Actuators A: Physical*, Vol. 100 No. 1, pp. 18–23.

Herdovics, B. and Cegla, F., 2016, Structural health monitoring using torsional guided wave electromagnetic acoustic transducers, *Structural Health Monitoring*, Vol. 17 No. 1, pp. 24–38.

Hirao, M., Fukuoka, H. and Miura, Y., 1982, Scattering of Rayleigh surface waves by edge cracks: Numerical simulation and experiment, *The Journal of the Acoustical Society of America*, Vol. 72 No. 2, pp. 602–606.

Hirao, M. and Ogi, H., 1999, An SH-wave EMAT technique for gas pipeline inspection, *NDT & E International*, Vol. 32 No. 3, pp. 127–132.

Howard, R. and Cegla, F., 2016, Monitoring thicknesses along a line using SH guided waves, *AIP Conference Proceedings*, Vol. 1706, p. 30014.

Howard, R. and Cegla, F., 2017, On the probability of detecting wall thinning defects with dispersive circumferential guided waves, *NDT & E International*, Elsevier, Vol. 86, pp. 73–82.

Huthwaite, P., 2014a, Evaluation of inversion approaches for guided wave thickness mapping, *Proceedings of the Royal Society A: Mathematical, Physical and Engineering Sciences*, Vol. 470 No. 2166, pp. 20140063–20140063.

Huthwaite, P., 2014b, Accelerated finite element elastodynamic simulations using the GPU, *Journal of Computational Physics*, Elsevier Inc., Vol. 257, pp. 687–707.

Huthwaite, P., Ribichini, R., Cawley, P. and Lowe, M., 2013, Mode selection for corrosion detection in pipes and vessels via guided wave tomography, *IEEE Transactions on Ultrasonics, Ferroelectrics, and Frequency Control*, Vol. 60 No. 6, pp. 1165–1177.

Huthwaite, P. and Simonetti, F., 2013, High-resolution guided wave tomography, *Wave Motion*, Elsevier B.V., Vol. 50 No. 5, pp. 979–993.

Innerspec, 2016, temate® MRUT (medium range UT), *www.innerspec.com.*

Intel®, 2017, Xeon Processor E5-2690, *ark.intel.com/products/64596/Intel-Xeon-Processor-E5-2690-20M-Cache-2_90-GHz-8_00-GTs-Intel-QPI.*

Jayaraman, C., Krishnamurthy, C. V. and Balasubramaniam, K., 2009, Higher order modes cluster (HOMC) guided waves - A new technique for ndt inspection, *AIP Conference Proceedings*, Vol. 1096 No. 1, pp. 121–128.

Kehlenbach, M., Kohler, B., Cao, X. and Hanselka, H., 2003, Numerical and experimental investigation of Lamb wave interaction with discontinuities, *Proceedings of the 4th International Workshop on Structural Health Monitorinhh*, Stanford, USA, pp. 421–428.

Khalili, P. and Cawley, P., 2016, Excitation of single-mode Lamb waves at high-frequency-thickness products, *IEEE Transactions on Ultrasonics,* *Ferroelectrics, and Frequency Control*, Vol. 63 No. 2, pp. 303–312.

Khalili, P. and Cawley, P., 2018a, The reflection of the A1 Lamb mode in the high frequency-thickness regime from 3-D part-depth holes, *Submitted to NDT & E International.*

Khalili, P. and Cawley, P., 2018b, Relative ability of wedge coupled piezoelectric and meander coil EMAT probes to generate single mode Lamb waves, *IEEE Transactions on Ultrasonics, Ferroelectrics, and Frequency Control*, Vol. 65 No. 4, pp. 648–656.

Khalili, P. and Cawley, P., 2018c, The choice of ultrasonic method for the detection of corrosion at inaccessible locations, *NDT & E International*, Vol. 99, pp. 80–92.

Kim, Y.Y., Park, C.I., Cho, S.H. and Han, S.W., 2005, Torsional wave experiments with a new magnetostrictive transducer configuration, *The Journal of the Acoustical Society of America*, Vol. 117 No. 6, pp. 3459–3468.

Kohler, B., Schubert, F. and Frankenstein, B., 2004, Numerical and experimental investigation of Lamb wave excitation, propagation, and detection for structural health monitoring, *Proceedings of the 2nd European Workshop on Structural Health Monitoring*, Munich, Germany, pp. 993–1000.

Krautkramer, H. and Krautkramer, J., 1990, *Ultrasonic Testing of Materials*, 4th ed., Springer-Verlag.

Li, J. and Rose, J.L., 2001, Excitation and propagation of non-axisymmetric guided waves in a hollow cylinder, *The Journal of the Acoustical Society of America*, Vol. 109 No. 2, pp. 457–464.

Liu, G.R. and Quek Jerry, S.S., 2003, A non-reflecting boundary for analyzing wave propagation using the finite element method, *Finite Elements in Analysis and Design*, Vol. 39 No. 5–6, pp. 403–417.

Lorenz, M. and Lewandowski, S., 2012, Ultrasonic multi-skip inspection at clamped saddle supports, *18th World Conference on NDT*, p. 206.

Lowe, M.J.S., Cawley, P., Kao, J.Y. and Diligent, O., 2002, The low frequency reflection characteristics of the fundamental antisymmetric Lamb wave a0 from a rectangular notch in a plate., *The Journal of the Acoustical Society of America*, Vol. 112 No. 6, pp. 2612–2622.

Lowe, M.J.S. and Diligent, O., 2002, Low-frequency reflection characteristics of the s0 lamb wave from a rectangular notch in a plate., *The Journal of the Acoustical Society of America*, Vol. 111 No. 1, pp. 64–74.

Ludwig, R. and Lord, W., 1988, A finite-element formulation for the study of ultrasonic NDT systems, *IEEE Transactions on Ultrasonics, Ferroelectrics and Frequency Control*, Vol. 35 No. 6, pp. 809–820.

Ma, J. and Cawley, P., 2010, Low-frequency pulse echo reflection of the fundamental shear horizontal mode from part-thickness elliptical defects in plates., *The Journal of the Acoustical Society of America*, Vol. 127 No. 6, pp. 3485–93.

Masserey, B. and Fromme, P., 2009, Surface defect detection in stiffened plate structures using Rayleigh-like waves, *NDT & E International*, Vol. 42 No. 6, pp. 564–572.

Masserey, B. and Fromme, P., 2013, Fatigue crack growth monitoring using high-frequency guided waves, *Structural Health Monitoring*, Vol. 12 No. 5–6, pp. 484–493.

Mirkhani, K., Chaggares, C., Masterson, C., Jastrzebski, M., Dusatko, T., Sinclair, A., Shapoorabadi, R.J., et al., 2004, Optimal design of EMAT transmitters, *NDT & E International*, Vol. 37 No. 3, pp. 181–193.

Mohr, W. and Holler, P., 1976, On inspection of thin-walled tubes for transverse and longitudinal flaws by guided ultrasonic waves, *IEEE Transactions on Sonics and Ultrasonics*, Vol. 23 No. 5, pp. 369–373.

Monkhouse, R.S.C., Wilcox, P.D. and Cawley, P., 1997, Flexible interdigital PVDF transducers for the generation of Lamb waves in structures, *Ultrasonics*, Vol. 35 No. 7, pp. 489–498.

Moser, F., Jacobs, L.J. and Qu, J., 1999, Modeling elastic wave propagation in waveguides with the finite element method, *NDT & E International*, Vol. 32 No. 4, pp. 225–234.

Mudge, P.J., 2001, Field application of Teletest long-range ultrasonic testing technique, *Insight*, Vol. 43, pp. 74–77.

Mudge, P.J. and Catton, P., 2008, Quantification of defect size from long range guided wave ultrasonic tests on pipes, *AIP Conference Proceedings*, Vol. 975 No. 1, pp. 147–154.

Ning Hu, Shimomukai, T., Fukunaga, H. and Zhongqing Su, 2008, Damage identification of metallic structures using A0 mode of Lamb waves, *Structural Health Monitoring: An International Journal*, Vol. 7 No. 3, pp. 271–285.

Nurmalia, Nakamura, N., Ogi, H. and Hirao, M., 2011, Detection of shear horizontal guided waves propagating in aluminum plate with thinning region, *Japanese Journal of Applied Physics*, Vol. 50 No. 7S.

Nurmalia, Nakamura, N., Ogi, H., Hirao, M. and Nakahata, K., 2012, Mode conversion behavior of SH guided wave in a tapered plate, *NDT and E International*, Elsevier, Vol. 45 No. 1, pp. 156–161.

Ogilvy, J.A., 1987, Wave scattering from rough surfaces, *Reports on Progress in Physics*, Vol. 50, pp. 1553–1608.

Ogilvy, J. a, 2000, Computer simulation of acoustic wave scattering from rough surfaces, *Journal of Physics D: Applied Physics*, Vol. 21 No. 2, pp. 260–277.

Pavlakovic, B., Lowe, M., Alleyne, D. and Cawley, P., 1997, Disperse: A general purpose program for creating dispersion curves, *Review of Progress in Quantitative Nondestructive Evaluation*, Vol. 16A, pp. 185–192.

Quarry, M.J. and Rose, J.L., 1999, Multimode guided wave inspection of piping using comb transducers, *Materials Evaluation*, Vol. 57 No. 10, pp. 1089–1090.

Rajagopal, P., Drozdz, M., Skelton, E.A., Lowe, M.J.S. and Craster, R. V., 2012, On the use of absorbing layers to simulate the propagation of elastic waves in unbounded isotropic media using commercially available Finite Element packages, *NDT & E International*, Elsevier, Vol. 51, pp. 30–40.

Ratnam, D., Balasubramaniam, K. and Maxfield, B.W., 2012, Generation and detection of higher-order mode clusters of guided waves (HOMC-GW) using meander-coil EMATs, *IEEE Transactions on Ultrasonics, Ferroelectrics, and Frequency Control*, Vol. 59 No. 4, pp. 727–737.

Ravenscroft, F., Hill, R., Duffill, C. and Buttle, D., 1998, CHIME- A new ultrasonic method for rapid screening of pipe, plate and inaccessible geometries, *7th European Conference on Non-Destructive Testing*, Vol. 3.

Ribichini, R., Cegla, F., Nagy, P. and Cawley, P., 2011, Study and comparison of different EMAT configurations for SH wave inspection, *IEEE Transactions* *on Ultrasonics, Ferroelectrics and Frequency Control*, Vol. 58 No. 12, pp. 2571–2581.

Rose, J.L., 2002, A baseline and vision of ultrasonic guided wave inspection potential, *Journal of Pressure Vessel Technology*, Vol. 124 No. 3, p. 273.

Rose, J.L., 2014, *Ultrasonic Guided Waves in Solid Media*, *Ultrasonic Guided Waves in Solid Media*, Cambridge University Press, New York.

Rose, J.L., Avioli, M.J., Mudge, P. and Sanderson, R., 2004, Guided wave inspection potential of defects in rail, *NDT & E International*, Vol. 37 No. 2, pp. 153–161.

Rose, J.L., Pelts, S.P. and Quarry, M.J., 1998, A comb transducer model for guided wave NDE, *Ultrasonics*, Vol. 36 No. 1–5, pp. 163–169.

ROSEN, 2016, IFSE service – External precision piping inspection, *www.rosen-Group.com.*

Roux, P., Roman, B. and Fink, M., 1997, Time-reversal in an ultrasonic waveguide, *Applied Physics Letters*, Vol. 70 No. 14, pp. 1811–1813.

Salzburger, H.-J., Niese, F. and Dobmann, G., 2012, EMAT pipe inspection with guided waves, *Welding in the World*, Vol. 56 No. 5–6, pp. 35–43.

Salzburger, H.J., 1995, Long range UT by structural ultrasonic waves and electromagnetic acoustic transducers (EMAT), *16th Major International UT Conference and Exhibition*, Edinburgh, U.K.

Salzburger, H.J., 2009, EMAT's and its potential for modern NDE-state of the art and latest applications-, *2009 IEEE International Ultrasonics Symposium*, IEEE, pp. 621–628.

Satyarnarayan, L., Chandrasekaran, J., Maxfield, B. and Balasubramaniam, K., 2008, Circumferential higher order guided wave modes for the detection and sizing of cracks and pinholes in pipe support regions, *NDT and E International*, Vol. 41 No. 1, pp. 32–43.

Schmerr, L.W., 1998, *Fundamentals of Ultrasonic Nondestructive Evaluation: A Modeling Approach*, Springer US.

Seher, M., Huthwaite, P., Lowe, M., Nagy, P. and Cawley, P., 2014, Numerical design optimization of an EMAT for A0 Lamb wave generation in steel plates, *AIP Conference Proceedings*, Vol. 1581 No. 1, pp. 340–347.

Seher, M., Huthwaite, P., Lowe, M.J.S. and Nagy, P.B., 2015, Model-based design of low frequency Lamb wave EMATs for mode selectivity, *Journal of Nondestructive Evaluation*, Springer US, Vol. 34 No. 3, p. 22.

Sheard, M. and McNulty, A., 2001, Field experience of using long-range ultrasonic testing, *Insight*, Vol. 43, pp. 79–83.

Simonetti, F., 2004a, *Sound Propagation in Lossless Waveguides Coated with Attenuative Materials*, PhD Thesis, Imperial College London.

Simonetti, F., 2004b, Lamb wave propagation in elastic plates coated with viscoelastic materials, *The Journal of the Acoustical Society of America*, Vol. 115 No. 5, p. 2041.

Sonomatic, 2016a, Topside SH-EMAT inspection, *www.sonomatic.com.*

Sonomatic, 2016b, CHIME® inspection, *www.sonomatic.com.*

Sonomatic, 2016c, Multiskip inspection, *www.sonomatic.com.*

Swaminathan, A.A., Balasubramaniam, B.K., Anto, C.I. and Venkataraman, K.S., 2011, Higher Order Mode Cluster (HOMC) guided wave testing of corrosion under pipe supports (CUPS), *Proceedings of the National Seminar & Exhibition on Non-Destructive Evaluation*, India, pp. 224–227.

Tems, R. and Al Zahrani, A.M., 2006, Cost of corrosion in oil production and refining, *Saudi Aramco Journal of Technology*, pp. 2–14.

Thompson, R.B., 1990, Physical principles of measurements with EMAT transducers, *Physical Acoustics*, Academic Press, New York, pp. 157–200.

Thompson, R.B., Alers, G. a. and Tennison, M. a., 1972, Application of direct electromagnetic Lamb wave generation to gas pipeline inspection, *1972 Ultrasonics Symposium*, IEEE, pp. 91–94.

Thompson, R.B., Alers, G. a. and Tennison, M. a., 1974, Method for ultrasonic inspection, United States Patent, United States of America.

Vasile, C.F., 1978, Electromagnetic Transducer, United States Patent, No. 4127035, USA.

Vasile, C.F., Thompson, R.B. and Fortunko, C.M., 1981, Method and Apparatus for Efficiently Generating Elastic Waves with a Transducer, United States Patent, No. 4248092, USA.

Vinogradov, S.A., 2009, Magnetostrictive transducer for torsional guided waves in pipes and plates, *Materials Evaluation*, Vol. 67 No. 3, pp. 333–341.

Wilcox, P., 2004, Modeling the excitation of Lamb and SH waves by point and line sources, *AIP Conference Proceedings*, Vol. 700, AIP, pp. 206–213.

Wilcox, P., Castaings, M., Monkhouse, R., Cawley, P. and Lowe, M., 1997, An example of the use of interdigital PVDF transducers to generate and receive a high order Lamb wave mode in a pipe, *Review of Progress in Quantitative Nondestructive Evaluation*, Springer US, Boston, MA, pp. 919–926.

Wilcox, P., Lowe, M. and Cawley, P., 2001a, The effect of dispersion on long-range inspection using ultrasonic guided waves, *NDT & E International*, Vol. 34 No. 1, pp. 1–9.

Wilcox, P.D., Lowe, M.J.S. and Cawley, P., 2001b, A signal processing technique to remove the effect of dispersion from guided wave signals, *27th Annual Review of Progress in Quantitative Nondestructive Evaluation (AIP Conf. Proc. 557)*, Vol. 20 No. 1, pp. 555–562.

Wilcox, P.D., Lowe, M.J.S. and Cawley, P., 2002, Mode and transducer selection for long range Lamb wave inspection, *Journal of Intelligent Material Systems and Structures*, Vol. 12, pp. 553–565.

Xu, B. and Giurgiutiu, V., 2007, Single mode tuning effects on Lamb wave time reversal with piezoelectric wafer active sensors for structural health monitoring, *Journal of Nondestructive Evaluation*, Vol. 26 No. 2–4, pp. 123–134.

Zemanek, J., 1972, An experimental and theoretical investigation of elastic wave propagation in a cylinder, *The Journal of the Acoustical Society of America*, Vol. 51 No. 1B, pp. 265–283.